

RÉPUBLIQUE ALGÉRIENNE DÉMOCRATIQUE ET POPULAIRE
MINISTÈRE DE L'ENSEIGNEMENT SUPÉRIEUR ET DE LA RECHERCHE SCIENTIFIQUE

Université des Sciences et de la Technologie d'Oran Mohammed Boudiaf

USTO-MB

FACULTÉ DE GÉNIE MÉCANIQUE

DÉPARTEMENT DE GÉNIE MÉCANIQUE

THÈSE

En vue de l'obtention du diplôme de doctorat en sciences en génie mécanique

SPÉCIALITÉ: GÉNIE MÉCANIQUE

OPTION: GÉNIE MÉCANIQUE

Présentée par:

Mr. Lakhdar AIDAOU

INTITULÉE

MODÉLISATION DE LA POLLUTION PHOTOCHIMIQUE DE L'AIR À L'ÉCHELLE LOCALE ET MÉSO

Soutenu publiquement le: 24.06.2015 devant le jury composé de:

Mme. Amina SABEUR	Pr	USTO-MB Oran	Présidente
Mr. Abbès AZZI	Pr	USTO-MB Oran	Rapporteur
Mr. Alberto MAURIZI	Dr	ISAC-CNR Bologne (Italie)	Co-Rapporteur
Mr. Nouredine SAD CHEMLOUL	Pr	UIK Tiaret	Examineur
Mr. Ahmed Zineddine DELLIL	Pr	U Oran	Examineur
Mme. Fadela NEMDILI	Dr	USTO-MB Oran	Examinatrice

ANNEE 2015

Abstract

Evaluation of the spatial and temporal distribution of nitrogen dioxide (NO₂) and Ozone (O₃) concentration at local-scale and meso-scale has attracted much interest from the scientific community, from both monitoring and modelling points of view. Photochemical air pollution modelling and simulation in different atmospheric scales was performed during this study.

In the first part of this work, the photochemical smog formation over a heavily industrialized area with complex terrain was investigated. A prognostic meteorological and air pollution model was used in combination with data, which were collected by in situ and remote monitoring stations. The results showed a considerable skill of the model in predicting the major local scale features affecting the pollutants' dispersion and concentrations in the area of interest. Numerical simulation data of photochemical pollutants were significantly correlated with meteorology during the simulation period. The correlation reveals the most important factors of ozone production, such as solar radiation, temperature, wind speed and topography.

In the second part of the study, NO₂ tropospheric vertical column density (VCD) was simulated at different resolutions using the online-coupled BOLCHEM model, with focus to high-polluted regions. High and low-resolution model output are compared to ozone monitoring instrument (OMI) data from the Tropospheric Emission Monitoring Internet Service (TEMIS) over selected areas for the year 2007. For this purpose, satellite data were averaged and regridded on daily basis, onto a common analysis grid with the same model resolutions. Moreover, model simulation results were processed using the averaging kernel (AK) information. The same criteria used to select satellite data, were used as a mask that is applied to model results to make the satellite and model datasets fully consistent. Standard statistical analysis reveals good model performances, even in highly polluted regions, with spatial correlation that ranges from 0.74 to 0.91, depending on the region and model resolution considered. Seasonal analysis shows some dependency on time, with lowest scores in winter, when the satellite product also suffers weaker statistical significance due to the presence of clouds. The increase in resolution is found to affect the spatial correlation of the two high-polluted regions differently, 5% and 23%. This difference is likely to depend on the very different meteorology of the two hot-spots.

Keywords: Photochemical simulation, Tropospheric NO₂ column, Model resolution effect, Ozone, Meteorology effect.

ملخص

يحوز تقييم التوزع الموضعي و الزمني لانتشار تراكيز ثنائي أكسيد النيتروجين NO₂ وكذا الأوزون O₃ على المستويين المحلي و المتوسط, على اهتمام لجان البحث العلمية سواء من ناحية المراقبة أو النمذجة. خلال هذه الدراسة تم التطرق إلى نمذجة و محاكاة التلوث الفوتوكيميائي للهواء على عدة مستويات في الغلاف الجوي.

في الجزء الأول من هذا المشروع, تم دراسة تشكل الغيوم الفوتوكيميائية على مستوى منطقة صناعية ذات تضاريس معقدة. حيث تم استخدام نموذج خاص بتلوث الهواء و الأرصاد الجوية, الى جانب بيانات القياس المأخوذة من المحطات المتوفرة على مستوى نفس المنطقة. أظهرت النتائج المتحصل عليها من طرف النموذج المستعمل دقة عالية للبرنامج في التنبؤ بأهم العوامل المؤثرة في توزع الملوثات و تراكيزها على مستوى المنطقة ذات الإهتمام. و المحاكاة الرقمية المنجزة وضحت العلاقة بين التلوث الفوتوكيميائي و عناصر الأرصاد الجوية خلال فترة المحاكاة, حيث أظهرت هذه العلاقة أهم العوامل المؤثرة في تكون الأوزون O₃, مثل الإشعاع الشمسي, درجة الحرارة, سرعة الرياح بالإضافة إلى التضاريس الصعبة للمنطقة.

خلال الجزء الثاني من هذه الدراسة, تمت محاكاة الكثافة العمودية لثاني أكسيد النيتروجين باستعمال عدة مقاييس مكانية للدقة و ذلك باستخدام البرنامج BOLCHEM, مع التركيز على المناطق الأكثر تلوثا. نتأج كل من الدقة العالية و العادية للبرنامج تم مقارنتها إلى بيانات القمر الصناعي OMI المأخوذة من مركز TEMIS و ذلك على مستوى المناطق المختارة لسنة 2007. لأجل تحقيق الهدف المشار إليه تمت معالجة بيانات القمر الصناعي على أساس يومي, و ذلك طبقا لنفس الخصائص المستعملة في برنامج المحاكاة. إضافة إلى ذلك تمت معالجة المحاكاة الرقمية للنموذج باستعمال معلومة Averaging kernel (AK), حيث خلال المعالجة, تم أخذ نفس المعايير التي استعملت في تصفية بيانات القمر الصناعي ثم استعمالها كقناع لحساب نتأج النمذجة, و ذلك لجعل بيانات كل من المحاكاة الرقمية و القمر الصناعي أكثر ملائمة. أظهرت التحاليل الإحصائية للنتأج المتحصل عليها بالمحاكاة دقة عالية للنموذج المستعمل, حتى على مستوى المناطق الأكثر تلوثا, مع ارتباط مكاني spatial correlation يتراوح بين 0.74 و 0.91 و ذلك تبعا للمنطقة المختارة و كذا دقة البرنامج. التحليل الفصلي للنتأج أظهر بعض الفروق, مع نتأج منخفضة في الشتاء حيث بيانات الأقمار الصناعية تكون متأثرة بوجود الغيوم. الزيادة في دقة البرنامج أثرت على الإرتباط المكاني في المنطقتين ذات التلوث العالي بشكل مختلف 5% و 23% هذا الفرق يرجع على الأرجح إلى الإختلاف في شروط الأحوال الجوية لكل من المنطقتين المعنيتين.

Résumé

L'évaluation de la distribution spatiale et temporelle de concentration du dioxyde d'azote (NO₂) et l'ozone (O₃) à l'échelle locale et méso, a suscité beaucoup d'intérêt de la communauté scientifique, des points de vue: contrôle et modélisation. La modélisation et la simulation de la pollution photochimique de l'air dans différentes échelles atmosphériques ont été effectuées au cours de cette étude.

Dans cette étude, la première partie a fait l'objet d'étude de formation de brouillard photochimique sur une zone fortement industrialisée avec un terrain complexe. Il s'agit d'un modèle de pollution de l'air et de météorologie qui a été utilisé en combinaison avec les données des stations de surveillance à distance. Les premiers résultats ont montrés une grande habileté du modèle, il peut prédire les principaux éléments qui affectent la dispersion et la concentration des polluants à l'échelle locale au niveau de la région sélectionnée. Les données de la simulation numérique des polluants photochimiques étaient significativement corrélées avec la météorologie au cours de la période de simulation. Cette corrélation a révélé les facteurs les plus importants de la production d'ozone, tels que le rayonnement solaire, la température, la vitesse du vent et la topographie.

La seconde partie de l'étude consiste en la simulation de la densité verticale du NO₂ troposphérique à des résolutions différentes et par l'utilisation du modèle couplé en ligne BOLCHEM, ainsi que par la prise en considération des régions très polluées. Les résultats des différentes résolutions du modèle ont été comparés aux données satellitaires d'OMI (Ozone Monitoring Instrument) de TEMIS (Tropospheric Emission Monitoring Internet Service) sur les régions sélectionnées durant l'année 2007. A cet effet, les données satellitaires ont été moyennées et re-maillées quotidiennement sur des grilles d'analyse communs avec les mêmes résolutions du modèle. De plus, les résultats de simulation numérique ont été traités en utilisant les informations du averaging kernel (AK). Les mêmes critères utilisés pour sélectionner les données satellite, ont été utilisés comme un masque qui est appliqué aux résultats du modèle, pour en faire à la fois les données satellitaires et du modèle pleinement compatible. L'analyse statistique révèle de bonne performance du modèle, même dans les régions les plus polluées, avec un coefficient de corrélation spatiale allant de 0.74 à 0.91, selon la région et la résolution du modèle considéré. L'analyse saisonnière montre une certaine dépendance dans le temps avec des scores plus faibles en hiver, lorsque le produit du satellite subit une grande incertitude due à la couverture nuageuse. L'augmentation de la résolution se trouve à affecter la corrélation spatiale des deux régions très polluées, différemment, 5% et 23%. Cette différence est probablement due à la différence de la météorologie qui affecte les deux régions.

Mots-Clefs: Simulation de la pollution photochimique, Colonne de NO₂ troposphérique, Ozone, Effet de la résolution, Effet de la météorologie.

ACKNOWLEDGEMENTS

First and foremost, praises and thanks to ALLAH almighty who has been giving me everything to accomplish this study.

There is not enough space, here, to mention all the people who have helped me, with scientific discussions, or with their friendship and encouragement, during this thesis work. I would like to thank all of them.

Nevertheless, I will mention some of the people who have played a major role. I would like to express my sincere acknowledge to my advisors Pr. Abbes Azzi and Dr. Alberto Maurizi, for their guidance and knowledge, their support and confidence for the development of this thesis.

I would like to thank my colleagues in the laboratory of development in mechanics and materials LDMM, University of Djelfa and at the University of sciences and technology of Oran (USTO-MB) for their help.

Besides, my thanks goes to the Atmospheric Dynamics and Turbulence Modelling Group team, at ISAC-CNR Bologna, Italy and the LAPEP laboratory team, Kozani Greece, for their collaboration and scientific support.

I thank in advance all members of the jury for taking the time to read this work and for their comments.

I am grateful to all my friends in Algeria and abroad for their great company and support.

Last but not least, I would like to thank my parents, my big and small families, for always being supportive, also for their comprehension, patience and prayers.

Dedicate to

My dear parents

My big and small families

and all who knows me.

...To my daughter Yasmine

TABLE OF CONTENTS

Abstract	i
ملخص	ii
Résumé	iii
Acknowledgements	iv
Table of contents	vi
Nomenclature.....	ix
List of figures	xi
List of tables	xiii

Chapter One.

INTRODUCTION.....	14
-------------------	----

Chapter Two.

PHOTOCHEMICAL AIR POLLUTION

2.1 Structure and chemical composition of the atmosphere.....	20
2.2 Air pollution definitions	21
2.2.1 Pollutants types.....	23
2.2.1.1 Primary Pollutants.....	23
2.2.1.2 Secondary Pollutants.....	24
2.2.2 Sources of pollutants.....	24
2.2.2.1 Mobility.....	24
2.2.2.2 Origin.....	25
2.2.3 Pollutant measures.....	26
2.2.3.1 Concentration.....	26
2.2.3.2 Mixing ratio.....	26
2.2.3.3 Residence time.....	26
2.3 Effects on pollutants dispersion.....	27
2.3.1 Effects of wind speed and direction.....	27
2.3.2 Effects of atmospheric turbulence.....	28
2.3.3 Effects of atmospheric stability.....	28
2.3.4 Effects of topography on air motion and pollution.....	29
2.4 Photochemical pollution formation.....	29
2.4.1 Diurnal and seasonal variation of photochemical smog.....	30
2.4.1.1 Diurnal variation of ozone.....	30
2.4.1.2 Seasonal variation of ozone.....	31
2.5 Photochemical air quality modelling.....	32

2.5.1	Introduction.....	32
2.5.2	Air Quality Models.....	32
2.5.3	Air quality models uncertainties.....	33
2.5.4	Air Quality management.....	34
2.5.5	3D Photochemical models requirements.....	36
2.5.6	Model formulation steps.....	37
2.6	Consequences of photochemical pollution.....	38
2.6.1	Damage on human health.....	38
2.6.2	Damage on the environment and ecosystems.....	41

Chapter Three.

DYNAMICS IN THE ATMOSPHERIC

BOUNDARY LAYER

3.1	Introduction.....	42
3.2	Time and space scales.....	42
3.3	Basic Equations of Atmospheric Fluid Mechanics.....	44
3.3.1	Equations for the Mean Quantities.....	46
3.3.2	Mixing-Length Models for Turbulent Transport.....	47
3.3.3	Variation of wind with height in the atmosphere.....	48
3.3.3.1	Mean Velocity in the Adiabatic Surface Layer over a Smooth Surface.....	49
3.3.3.2	Mean Velocity in the Adiabatic Surface Layer over a Rough Surface.....	50
3.3.3.3	Mean Velocity Profiles in the Nonadiabatic Surface Layer.....	50
3.4	Atmospheric stability.....	53
3.5	Air pollution modelling	54
3.6	3D atmospheric chemical transport models.....	55
3.6.1	Coordinate System-Uneven Terrain.....	56
3.6.2	Initial conditions.....	58
3.6.3	Boundary conditions.....	59

Chapter Four.

MODELLING METHODOLOGY

4.1	Introduction	61
4.2	Local-scale simulation.....	61
4.2.1	Study area and dataset description.....	62
4.2.2	Air pollution model.....	64
4.2.2.1	Model description.....	64
4.2.2.2	Model configuration.....	65
4.2.3	Data analysis.....	65
4.3	Meso-scale simulation.....	67
4.3.1	Model description.....	68
4.3.2	Experimental set-up.....	69

4.3.3	Satellite data (OMI sensor).....	70
4.3.4	Satellite tropospheric NO ₂ VCD level-3 production.....	71
4.3.5	Computation of tropospheric NO ₂ VCD.....	72
4.3.6	Statistical metrics.....	73
4.3.7	Data processing.....	74

Chapter Five.

RESULTS AND ANALYSES

5.1	Introduction	75
5.2	Photochemical air pollution modelling in local-scale.....	75
5.2.1	Meteorology.....	75
5.2.2	Model's results and validation of chemistry.....	78
5.2.3	Effect of meteorology on O ₃ , NO ₂ formation.....	81
5.3	Tropospheric NO ₂ vertical column densities simulation.....	84
5.3.1	Low-resolution results.....	84
5.3.2	High-resolution results.....	91
	CONCLUSIONS	95
	References	98

NOMENCLATURE

Acronyms & Latin symbols

AK	Averaging kernel	
Alt	Altitude	[°]
C	Concentration of a pollutant	[$\mu\text{g}\cdot\text{m}^{-3}$]
CDO	Climate Data Operators	
CO	Carbon monoxide	
c_p	Specific heat at constant pressure	[$\text{J}\cdot\text{kg}^{-1}\cdot\text{K}^{-1}$]
c_v	Specific heat at constant volume	
E	Turbulence kinetic energy	[$\text{J}\cdot\text{kg}^{-1}$]
E_i	Emission fluxes	$\text{g}/\text{m}^2\cdot\text{s}$
EGM	Eulerian Grid Module	
g	Gravitational constant	[$\text{m}\cdot\text{s}^{-2}$]
HDF	Hierarchical Data Format	
h_r	Reference height	m
h_v	Photosynthetically active radiation.	
IOA	Index of Agreement	
K	Diffusion coefficient	
k	Von karman constant (0.41)	
Lat	Latitude	[°]
L	The Monin-Obukhov length	m
Lon	Longitude	[°]
M	The molecular weight of the substance	[$\mu\text{g}\cdot\text{mol}^{-1}$]
AMF	The air mass factor	
MB	Mean bias	
MS	Monitoring Station	
netCDF	Network Common Data Form	
NO ₂	Nitrogen dioxide	
NO	Nitric oxide	
O ₃	Ozone	
P	The Pressure	[hPa]
PM	Particulate Matter	
ppb	Part per billion	
ppm	Part per million	
ppmm	Part per million mass	
ppmv	Part per million volume	
PS	Power station	
Q	Heat flux	W/m^2
q_z	The sensible heat flux	W/m^2
r	Correlation coefficient	
R	Gas constant	[$\text{J}/\text{mole}\cdot\text{K}$]
R_f	The flux Richardson number	
RMSE	Root-Mean-Square-Error	

Nomenclature

S_i	Removal fluxes	$g/ m^2. s$
Sigma	Sigma coordinate system	
SO_2	Sulphur dioxide	
TAPM	The air pollution model	
T	Temperature	[K]
t	The time	[s]
TM4	The chemistry transport model	
u_1	Horizontal velocity (x)	$[m.s^{-1}]$
u_2	Horizontal velocity (y)	$[m.s^{-1}]$
u_3	Vertical velocity (z)	$[m.s^{-1}]$
UV	Ultraviolet	
v_d	The deposition velocity	$[m.s^{-1}]$
VDC	Vertical Column Density	$Molcs/cm^2$
VOC	Volatile Organic Compounds	

Greek symbols

θ	Potential temperature	[K]
ν	The kinematic viscosity	m^2 /s
ϕ	Stability universal function	
λ	Thermal conductivity	$[W/m. K]$
μ	The dynamic viscosity	$kg/(m.s)$
ρ	The density of the fluid	Kg/m^3
ϵ	The height of the roughness element	m
ζ	The terrain-following coordinate	
β	Represent the ratio (z/L)	
τ	The shear stress	Pa
ω	Vertical wind speed for the terrain following system	$[m.s^{-1}]$
∇	Nabla operator	
Δz	The vertical grid spacing	[m]
Φ	A scalar	
δ_{ij}	Symbol of Kronecker (=1 if $i=j$, =0 otherwise)	

LIST OF FIGURES

2-1	Vertical temperature distribution in the atmosphere (Roulet 2004)	21
2-2	Evolution of world's population, vehicle fleet, fossil fuel consumption and GNP from 1950 to 1990.(J.Kubler 2001).....	23
2-3	Simplified schematic representation of the photochemical smog formation.....	30
2-4	Diurnal cycle of O ₃ and its precursors.....	31
2-5	Schematic representation of the seasonal variation of ozone and a primary pollutant (CO).....	32
2-6	Eulerian three-dimensional photochemical model.(From. J.Kubler 2001).....	33
2.7	Diagram of the basic concepts on the role of air quality modelling.....	35
2.8	Schematic diagram of the general structure of a photochemical model.....	37
3.1	Daily evolution of the atmospheric boundary layer (Stull, 1988).....	43
3.2	Eddy transfer in a turbulent shear flow.....	47
3.3	Wind profile modification due to stability (Thom, 1975).....	53
3.4	Scheme of processes described in a chemistry transport model (Sportisse, 2007).....	55
3.5	Coordinate transformation for uneven terrain.....	57
4.1	Topography of the area covered by the inner grid with the Power Stations (PS) Triantafyllou et al, 2013).....	63
4.2	Street canyon covered by DOAS light path, and the measurement station location.....	64
4.3	Selected regions for analysis: Europe (yellow), Po Valley (red), BeNeLux (blue) and Gibraltar (green), overlapped to average NO ₂ emission rates sample (unit: mol /m ² /h).....	67
4.4	BOLCHEM flow chart (http://bolchem.isac.cnr.it/projects/bolchem.do).....	69
4.5	Difference between satellite grid and fixed regular grid.....	71
5.1	Meteorological monitoring station MS compared to TAPM results for: a) Wind direction, b) Temperature, c) Wind speed and d) Solar radiation (SR).....	78
5.2	Observed and predicted mean hourly Ozone concentrations (ppb), obtained by TAPM, Measurement station and DOAS, during the simulated period; 23-29 June 2006.....	79
5.3	Comparison between measured and simulated Ozone, where r is the correlation coefficient and S is the slope.....	80
5.4	Concentrations of NO ₂ , obtained by TAPM, Measurement station and DOAS, during the simulated period between 23 and 29 June 2006.....	81
5.5	The variation of Ozone, NO ₂ concentrations with solar radiation (a), temperature (b) and wind speed (c), during the simulated period.....	83
5.6	Annual average of NO ₂ VCD (Unit: ×10 ¹³ molecules cm ⁻²) over Europe: left (model), centre (difference: model-satellite) and right (satellite).....	85
5.7	Area-averaged over Europe (see Figure 4.3) of the monthly mean tropospheric columns for 2007.....	86
5.8	Seasonal average of NO ₂ VCD (Unit: ×10 ¹³ molecules cm ⁻²) over Europe: left (model), centre (difference: model-satellite) and right (satellite). Seasons are: winter, springer, summer and autumn from top to bottom, respectively.....	87

5.9	Annual average of NO ₂ VCD (Unit: $\times 10^{13}$ molecules cm ⁻²) over Po Valley: left (model), centre (difference: model-satellite) and right (satellite), for low-resolution (top) and high-resolution (bottom).....	91
5.10	Annual average of NO ₂ VCD (Unit: $\times 10^{13}$ molecules cm ⁻²) over BeNeLux: left (model), centre (difference: model-satellite) and right (satellite), for low-resolution (top) and high-resolution (bottom).....	93
5.11	Annual average of NO ₂ VCD (Unit: $\times 10^{13}$ molecules cm ⁻²) over Gibraltar: left (model), centre (difference: model-satellite) and right (satellite).....	89
5.12	Area-averaged over Gibraltar (see Figure 4.3) of the monthly mean tropospheric columns for 2007 (left panel). In the right panel, relative differences are shown.....	90
5.13	Scatter plots between BOLCHEM and OMI NO ₂ columns: a) Europe, b) Gibraltar at low-resolution, c) Po Valley and d) BeNeLux at high-resolution. r is the correlation coefficient and S is the slope.....	90
5.14	Area-averaged over Po Valley (see Figure 4.3) of the monthly mean tropospheric columns for 2007 with different model resolutions (left panel). In the right panel, relative differences are shown.....	92
5.15	Area-averaged over BeNeLux (see Figure 4.3) of the monthly mean tropospheric columns for year 2007 with different model resolutions (left panel). In the right panel, relative differences are shown.....	94

LIST OF TABLES

2.1	Examples of sources of primary pollutants.....	25
2.2	<i>Orders of magnitude of the atmospheric pollutants' concentrations and their typical time of stay in the atmosphere.(Atmosphère météorologique et air humide J-F Sini, 2005)</i>	27
2.3	Scale definitions and different processes with characteristic time and horizontal scales. (After Atkinson, 1981).....	36
2.4	Sources, health and welfare effects for selected Pollutants (Ref: US EPA website).....	40
3.1	Time and distance magnitude scales for atmospheric layers (adapted from San-tamouris and Dascalaki, 2003).....	43
3.2	Monin-Obukhov Length L with Respect to Atmospheric Stability.....	52
3.3	Coordinate Systems for Solution of the Atmospheric Diffusion Equation.....	58
5.1	Model performance statistics for meteorology.....	76
5.2	Model performance statistics of mean hourly Ozone concentrations during the considered period.....	79
5.3	Model performance statistics of ozone's daily variation computed from the hourly averages values of the whole period.....	80
5.4	The correlation coefficient r of chemical and meteorological TAPM results.....	82
5.5	Annual and seasonal statistical indices computed over Europe and selected regions. Units for RMSE and MB is $\times 10^{13}$ molecules cm^{-2}	86

CHAPTER 1

INTRODUCTION

Evaluation of the spatial and temporal distribution of nitrogen dioxide (NO₂) and Ozone (O₃) concentration in local and meso scales has attracted much interest from the scientific community, from both monitoring and modelling points of view. Pollutants directly emitted from sources (primary pollutants) include NO_x (NO + NO₂), SO₂, volatile organic compounds (VOCs), or formed in the atmosphere as the result of chemical transformation (secondary pollutants) e.g. ozone (O₃), are harmful to human health (Latzka et al., 2009; Vlachokostas et al. 2010a). The combination of chemical substances and specific meteorological parameters are the cause for the formation of the ground-level ozone layer. The formation and accumulation of ozone at the ground level is dangerous for people with respiratory disorders (Bernard et al. 2001). Moreover, crop damages from photochemical air pollution constitute one of the most serious problems in the agricultural sector at the present time (Vlachokostas et al. 2010b). Ozone has also a negative impact on forests, materials and ecosystems (Wang et al. 2005; Linkov et al. 2009). High temperature, sunlight and increased surface pressure have been proved to cause ozone formation (Chen et al. 2003). In addition, local circulations e.g. sea breeze (Moussiopoulos et al. 2006) may assist in ozone formation by creating adequate dilution conditions that accelerate photochemical reactions. Wind speed and direction have also been considered as important factors in the formation of ozone (Brulfert et al. 2005).

Besides, NO₂ is one of the most important atmospheric pollutants, due to its effect on human health (see, e.g., Latzka et al, 2009), and, specifically, its influence on mortality (see, e.g., Chen et al, 2012). Furthermore, it plays a basic role in the formation of ground ozone which is known to be harmful, not only for human, but also for ecological health (Ashmore, 2005). As a

consequence, it is one of the few pollutants that are regulated by the environmental policy and, accordingly, it is considered to be one of the main indexes of local pollution (Richter et al, 2005; Monks et al, 2009).

It also affects the climate by increasing the levels of greenhouse gases (Solomon et al, 1999). A small fraction of NO₂ is directly emitted while the largest part is a secondary product and derives basically from emitted NO. NO + NO₂ constitutes the NO_x family. NO_x originates from different sources (combustion of fossil fuel, biomass burning, microbiological processes in soil, lightning, wildfires ...) but it is mainly of anthropogenic origin, being the result of high temperature combustion processes.

As a consequence, the quantification of both: NO₂ and O₃ atmospheric levels are important for understanding tropospheric pollution and provide information for air pollution monitoring, modelling and management. Different classes of tools are available for this purpose. Ground-level measurement networks furnish detailed information on local surface concentration, while satellite instruments gives information at a large scale with global coverage (low earth orbit satellites - LEO), although limited to vertically integrated properties and also typically limited to one measurement per day (for LEO). Coupled models of atmospheric dynamics and chemistry are used in combination with measurements to obtain further information concerning the spatial and temporal distribution of pollutants (Yen-Ping Peng et al. 2011; Lalitaporn et al., 2013), forecast pollutant concentrations (see, e.g., Dias de Freitas et al. 2005; Kukkonen et al., 2012, for a recent review), and perform scenario studies (see, e.g., Colette et al., 2012). Photochemical air quality models take data on meteorology and emissions, couple the data with descriptions of the physical and chemical processes that occur in the atmosphere, and numerically process the information to yield predictions of air pollutant concentrations as a function of time and location.

In the last decade, an increasing number of studies have used both model simulations and observations (satellite retrieved data and surface monitoring stations) for different purposes. In some cases, the two types of information are used in combination to give a more comprehensive picture and study specific features, as in Im et al. (2014) where the major pollutant levels are simulated over Europe for the year 2008, the model simulations are compared with surface observations stations, ozone (O₃) soundings, ship-borne O₃ and nitrogen dioxide (NO₂) observations in the western Mediterranean, NO₂ vertical column densities from the SCIAMACHY instrument, and aerosol optical depths (AOD) from AERONET. The obtained

results reveal differences in the model performance between the different simulated regions, suggesting significant differences in the representation of anthropogenic and natural emissions in these regions.

Also in Curier et al. (2014), the tropospheric NO₂ concentration trends during 2005-2010 over Europe were derived from the Ozone Monitoring Instrument (OMI) and LOTOS-EUROS models and compared to reported NO_x emissions, or Wang and Chen (2013), where a combination of model results and satellite data were used to derive surface concentrations of NO₂. However, a large part of the literature deals with model verification using satellite data as a reference, with the assessment of different simulation parameters on the model results. Huijnen et al. (2010) compared the ensemble median of the Regional Air Quality (RAQ) models in the Global and regional Earth-system (Atmosphere) Monitoring using Satellite and in-situ data (GEMS) Project with the tropospheric NO₂ vertical column density (VCD) from Dutch OMI NO₂ (DOMINO) 1.0.2, for the period July 2008–June 2009, over Europe. The spatial distribution was found to agree well with OMI observations, displaying a correlation of 0.8. A comparative study between OMI observations and CMAQ model simulations of tropospheric NO₂ VCD in East Asia (Han et al., 2011), was carried out over seasonal episodes in 2006, to evaluate the accuracy of the NO_x emissions over the Korean peninsula, with correlation that ranges from 0.52 to 0.85, depending on the region and season considered. In Zyrichidou et al. (2013), the CAMx model is used to simulate NO₂ tropospheric VCD at high-resolution, which were evaluated and compared against both a previous study and OMI measurements over South-eastern Europe. The annual spatial correlation between OMI and the high resolution model turned out to be 0.6, somewhat improved compared to a previous study (Zyrichidou et al., 2009). When using satellite data for model evaluation, it must be borne in mind that the satellite product itself is the result of an inversion process which, in turn, relies on model results. In fact, tropospheric vertical column density VCD is the result of direct observation of the bulk radiative effect of the observed quantity at given wavelengths, combined with a retrieval algorithm involving the use of a priori profiles derived from model results (Richter and Burrows, 2002; Boersma et al., 2007). This is largely discussed when satellite products are compared (see, e.g., Zyrichidou et al., 2013) and taken into account when model performances are verified against satellite data (Zyrichidou et al., 2009; Yamaji et al., 2014). However, satellite products have become more reliable also as a consequence of the improvements in the inversion procedure.

Since the mid-nineties, satellite remote sensing has been used to derive tropospheric NO₂ concentrations on different atmospheric scales (Schaub et al., 2007; Hilboll et al., 2013), starting with GOME-1, then SCIAMACHY, OMI and GOME-2. Among these satellite instruments, OMI has a better spatial resolution ($13 \times 24 \text{ km}^2$ at nadir) than GOME ($320 \times 40 \text{ km}^2$) and SCIAMACHY ($60 \times 30 \text{ km}^2$), which makes it suitable for use in modelling studies where resolution can be relatively high.

Two research studies were conducted during the present thesis. Within the first part, the photochemical smog formation over a heavily industrialized area with complex terrain was investigated. Pollutants' concentrations and meteorological parameters reveal the most important factors of ozone production were discussed. A coupled local-scale prognostic meteorological and air pollution model is used, in combination with data, which were collected by a conventional ground monitoring station (MS) and a differential optical absorption spectroscopy (DOAS) system. A seven-day period in the summer of 2006 was selected for simulation and, in particular, the 23–29 of June 2006. This period of the year was recorded as a period with high temperatures and elevated air pollutant concentrations in the region of interest. For the same period, experimental data from the MS and DOAS system have also been collected. The analysis of pollutants' concentrations and meteorological parameters reveals the most important factors of ozone production, such as solar radiation, temperature, wind speed and topography. The methodological advance in the first work is the combined use of in situ and remote sensing measurements and the outputs of the local-scale simulations with the air pollution model TAPM.

The second part of the current doctorate research activity deals with the simulation of NO₂ tropospheric vertical column density (VCD), at different resolutions versus OMI satellite data. Satellite data were regridded on daily basis, onto a common analysis grid with the same model resolutions. In the regridding procedure, data with cloud cover larger than 0.2, surface albedo larger than 0.3 and solar zenith angle larger than 85° are discarded. This filter produces a mask of valid measurements that is applied also to model results to make the satellite and model datasets fully consistent. The model output was sampled at the same satellite overpass time over Europe (13:30 UTC). The modelled VCD was computed using the averaging kernel (AK) corrected by the ratio between the total and the tropospheric AMF (Eskes and Boersma 2003). Because model simulation reach a height of about 500 hPa, the upper NO₂ content was extrapolated linearly from the upper model value to zero at the tropopause (where O₃ exceeds

150 ppb which, above Europe, corresponds to about 200 hPa) (Huijnen et al. 2010). The linear extrapolation to zero is well-supported by the climatological fields used in CITYZEN (Colette et al. 2011) and the analysis about the application of the AK found in Huijnen et al. (2010).

Additionally, in this part, the BOLCHEM model (Mircea et al., 2008; Maurizi et al., 2010) is employed to simulate NO₂ VCD with the aim of verifying the model's performances in highly polluted areas affected by different meteorological conditions, using different model resolutions. The OMI DOMINO product v2.0 (Boersma et al., 2007) will be used for comparison. BOLCHEM started as an online coupled meteorology and composition model (Baklanov et al., 2014) in 2003 (Butenschoen et al., 2003), when this approach was relatively new. It was successfully used in the GEMS Project for operational forecasts of gas phase pollutants as a member of the GEMS-RAQ ensemble, for over 1.5 years. In the same framework, it was compared indirectly, as part of the GEMS-RAQ ensemble, to satellite-retrieved NO₂ VCD (Huijnen et al., 2010) and, directly, with IASI tropospheric O₃ columns (Zyryanov et al., 2012). Moreover, an upgraded version (2.0) was also verified in a 10-year experiment against surface data measurements as part of "megaCITY - Zoom for the Environment" (CITYZEN) project (Colette et al, 2011), showing good skills particularly for NO₂ surface concentration.

This partial work focuses on two main aspects: beside the analysis of the general behaviour over Europe, one of the main interests is on the ability of the model to capture the NO₂ content in the two most polluted European areas (PoValley and BeNeLux). In those highly populated regions, emissions of NO_x change rapidly over very fine spatial scale (size of roads). This fact combined with the non-linear nature of NO₂, makes the model resolution an important parameter. The evaluation of the effects of resolution change is the second objective of the present work.

Model simulations were performed throughout 2007 (the last year of the 10-year CITYZEN experiment) over Europe and the two main hot-spots therein: the Po Valley and the BeNeLux area. In addition, the area of Gibraltar is also considered since, in the absence of other important pollutant sources, shipping emissions have a major role. Analyses will be discussed on annual and seasonal bases and the effect of resolution will be also addressed.

The thesis is organized as follow: Chapter 2 describes the structure and chemical composition of the atmosphere and the important issues in the development of photochemical pollution in the Tropospheric level. A large part of the chapter deals with general aspects such as

the composition and sources of photochemical pollution, in addition to the different parameters affecting the pollutants dispersion in the atmospheric boundary layer. The effects of photochemical pollution on human health and ecosystem are discussed. The second part of this chapter deals with the numerical modelling of photochemical pollution. The structure of photochemical models is presented in general.

Chapter 3 presents the fundamental equations of fluid mechanics governing the atmosphere dynamics, mainly in the atmospheric boundary layer. Meteorology conditions affecting the atmospheric stability are also discussed in the second part of the current chapter. Additionally, fundamentals of the air pollution modelling in the atmospheric boundary layer are presented. In chapter 4, the modelling methodology for both: local scale modelling and meso-scale modelling were described. Concerned the local scale modelling, a general illustration of the study area and the emission sources existing in the selected region was mentioned. The model description and configuration over the region of interest is also presented, in addition to some information about the measurement tools used in this part: monitoring station (MS) and DOAS system. At the end of this phase, the data analysis method used for the comparison and combination between simulation and measurements was described.

The second part of chapter 4 was devoted to the meso-scale modelling of NO₂ tropospheric vertical column densities (VCDs) with BOLCHEM model and retrieved data from OMI satellite, including the model description and experimental set-up, satellite retrieval algorithm, tropospheric NO₂ VCD characteristics and selected regions and the NO₂ VCD computation procedures.

In the last chapter (results and analyses), obtained results for photochemical air pollution modelling and simulations in local and meso scales are presented. The simulations results are evaluated with measurements from monitoring station and DOAS system for the first part and against satellite databases for the second one. Appropriate statistical performance measures (IOA, RMSE, MB and Pearson's correlation coefficient r) are used in the comparison and analyses. Finally some conclusions and perspectives for future studies are drawn.

CHAPTER 2

PHOTOCHEMICAL AIR POLLUTION

2.1. Structure and chemical composition of the atmosphere

The atmosphere can be viewed as a very thin layer in comparison to the volume of the Earth, which protecting the Earth and our life. Nearby 75% of the lower 7-16 km of the atmosphere's mass consists of the four chemical species: nitrogen (N_2 , 78 %), oxygen (O_2 , 21 %), argon (Ar, 0.93 %), and carbon dioxide (CO_2 , 0.03 %), which maintain these constant proportions up to about 80 km above the Earth's surface. The last few hundredths of a percent consist of trace elements, which can have concentrations that are constant in time, as for instance methane (CH_4), carbon monoxide (CO), and hydrogen (H_2), or variable, as ozone (O_3), sulphur dioxide (SO_2), and the nitrogen oxides ($NO_x = NO + NO_2$). In addition, water (H_2O) is present in highly variable proportions and totalling about 1 % of the atmosphere's volume, either as a gas or condensed as clouds (Roulet 2004).

The atmosphere decomposed in the vertical direction into four separate layers of different thicknesses, which related with a specific vertical temperature profile and chemical composition of its species (Figure 2.1). The thermosphere is the upper layer in the atmosphere, which is far from the Earth's surface by about 500-600 km, in this layer it exists the very high temperature of the atmosphere, which varied from 1000 to 2000 k according to the solar activity. After the thermosphere layer, the temperature of the air decreases very much where it gets the lowest value in the total atmosphere (193 K) in the mesopause layer, the mesopause is situated about 80 km above the Earth's surface. The next atmospheric layer is the mesosphere, it is located in between the two layers: mesopause and the stratopause layer, which about 50 km above the Earth's surface. In the mesosphere we find a high temperature increase from 193 K at the mesopause to about 273 K at the stratopause. The absorption of UV rays in addition to

the ozone formation in the stratosphere are the main reasons of the highest temperature at this level. The highest boundary of the stratosphere is defined as: stratopause. In addition to that the stratospheric layer is very dry, and the temperature in the top half of this layer decreases remarkably down to about 20 km far from the Earth's surface. Then in the lower boundary part of the stratosphere or the ozone layer and the tropopause. A very strong winds characterised the the tropopause region. The troposphere is the lowest layer in the atmosphere, its height latitudes vary from 8 km to 18 above the Equator. Also this layer is characterised by a high gradient of temperature toward the surface of the Earth, 6 k per km. In addition to high concentrations of water vapour and condensed water (Roulet 2004).

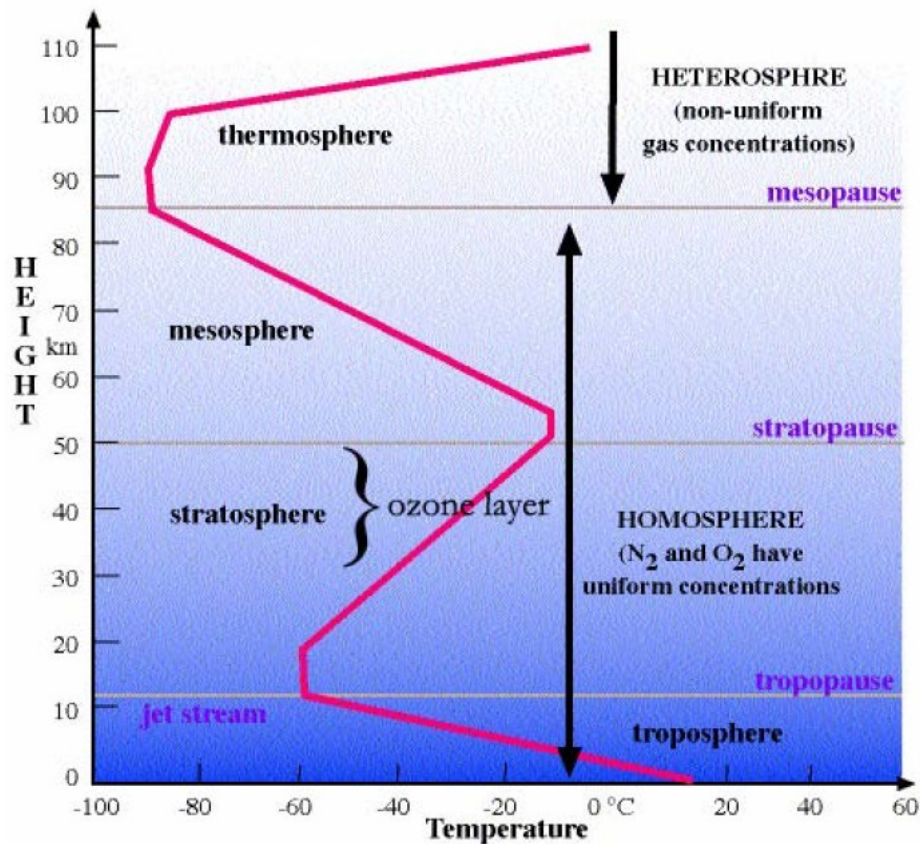


Figure 2.1 Vertical temperature distribution in the atmosphere (Roulet 2004).

2.2. Air pollution definition

Air pollution can be defined by the contamination of the atmosphere by different types of wastes (solid, liquid and gaseous). Those outputs are harmful to human life, animals and vegetation and also materials and structures, they also cause the visibility reduction. There are

many types of air pollutants in the atmosphere: solid, liquid or gaseous. Origins of pollutants can come from human sources for example: urban heating, transportation, industrial emissions ...) or natural sources like: fire forestry, emissions from volcanoes, particle matters and dust ...etc).

The atmosphere of the Earth comprises a lot of types of air pollutants. The effects of a substance depend on three factors [J.Kubler, 2001]:

Concentration: The pollutant is a component existing in many location with high concentration. A substance may not be a pollutant at a normal concentration, but if a substance presents with high concentration, it can causes and adverse effect: For example, the CO₂ (carbon dioxide) is necessary for our life, but it is considered as as pollutant if exist with high quantity.

Location: A pollutant present is maybe good in a location and considered as pollutant in an other place. for example, the ozone O₃ is one of the main pollutant causing photochemical pollution in low level, in the same time it protect us from UV radiation.

Time: The period of change of a substance is essential factor. When the increase of a pollutant is not fast, its effect can not be harmful to ecosystems, for example the formation of the oxygen in the atmosphere since the previous e time. Nevertheless, with the industrial growth with high rates the ecosystems can not resist to this changes, which menace the life equilibrium in the planet. During the past time the human-mad activities were not important against the natural-mad, but since the increase of industry in the last few decades, the pollutants emissions increased. As an example: the energy transformations caused by the human activity is approximately 40% from the those of the ecosystem.

In order to better understand the variation and the relationship between the economic and demographic variation in our world, figure 2.2 give us a quick opinion about their changes and magnitudes during the last 50 years. While the population multiplied by two, the GNP (Gross National Product) which is the Indicator of economic development was multiplied by six, in the same time the consumption of the fossil fuel quadrupled [J.Kubler, 2001].

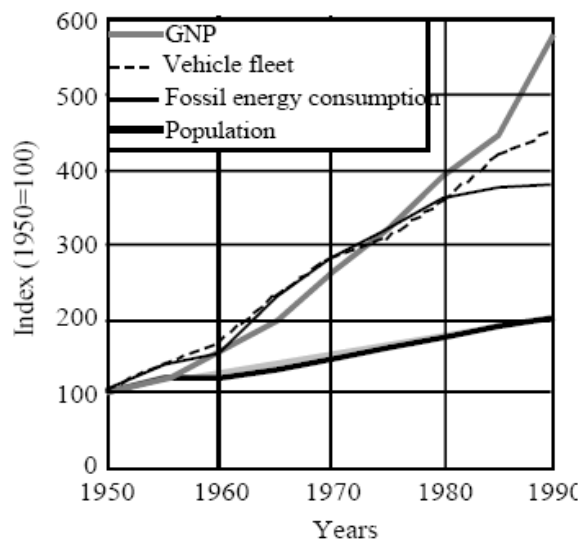


Figure 2.2 Evolution of world's population, vehicle fleet, fossil fuel consumption and GNP from 1950 to 1990. (J.Kubler 2001)

2.2.1.Types of pollutants

Generally, two types of air pollutants have been known in the atmosphere, the primary pollutants and the secondary pollutants.

2.2.1.1.Primary Pollutants

Primary pollutant continues in the first chemical form as it is emitted to the atmosphere from the source. The primary pollutants involve materials (solids, gases and liquids), they come in the atmosphere because of human activities and nature-made. The most important primary pollutants affecting the atmosphere are:

CO (Carbon monoxide). It is an odorless, colorless, poisonous gas. Also is resulted from the incomplete combustion in the vehicles and the organic matter decomposition. It affects oxygen-carrying capacity of blood and generates headaches and fatigue.

NO (Nitric oxide). This pollutant comes from transportation and industry, it is also created from secondary reactions like the formation of ozone.

SO₂ (Sulphur dioxide). It is mainly formed from the combustion of the full in immobile sources. It affect the respiration mainly.

VOCs (Volatile Organic Compounds). The VOC is an organic molecule formed of carbon and hydrogen atoms. It is produced during the incomplete combustion and industrial emissions.

PM (Particulate Matter). The particle matter released mostly from solid emissions by industry. It causes mainly the reduction of visibility.

NH₃ (Ammonia). It is usually related with the formation of aerosol.

2.2.1.2.Secondary Pollutants

When the primary pollutants react with each other and with the atmospheric substances, this reactions form new toxic chemical species, named secondary pollutants. In urban areas, the combination between emissions from transport and industry from one side and the sun light in the other side produce the photochemical smog. Photochemical pollution is very toxic to planet life (animal and human life, materials).

Nitrogen dioxide, NO₂, forms a brownish color in the atmosphere and is also the reason of lung damage.

Ozone, O₃, is the main chemical substance forms the photochemical smog, it is a colorless gas causing lung damage, eye irritation and damage to vegetation.

Sulphuric acid, H₂SO₄, it is related with the formation of aerosol in addition to respiratory problems acid rain and the reduction of visibility.

2.2.2.Sources of pollutants

The air pollution sources can be divided in many types (David H.F Liu, 2000), depending on their:

2.2.2.1.Mobility

- *Stationary*. Can be an area or point sources. *Area sources* include vehicular traffic in an area in addition to fugitive dust emissions from open air stock piles of resource materials at industrial plants. *Point sources* describe pollutant emissions from stacks (industrial and fuel combustion). Table 2.1 shows examples of sources of air pollution. Included in these categories are transportation sources, fuel combustion in stationary sources, industrial process losses, solid waste disposal, and miscellaneous items. This organization of source categories is basic to the development of emission inventories (David H.F Liu, 2000).
- *Mobile* (e.g. line sources) involve heavily transport highway facilities and the boundaries of forest fires.

2.2.2.2.Origin

- *Natural*. Which means the activities happened without the humans intervention. Including: Volcano emissions are natural sources. Biogenic processes, involving those that related to a living makes.
- *Anthropogenic*. Or man-made sources, which is caused by the human activities . These are mostly related to the burning of multiple types of fuel. As example, the humans activities increase the dust in the ground and thus the wind will raise dust from the ground into the air.

	Sources.	Pollutants.
Natural.	Volcanic eruptions Forest fires Dust storm Ocean waves Vegetation Hot springs	Particle(dust,ash),gases(SO ₂ CO ₂) Smoke, unburned hydrocarbons (CO ₂ ,NO _x , ash) Suspended particulate matter Salt particles Hydrocarbons (VOCs), pollen Sulfurous gases
Human caused Industrial. Personal.	Paper mills Power Plants-coal Oil Refineries Manufacturing-H ₂ SO ₄ PO ₄ fertilizer Iron and street mills Automobiles, fireplaces, home Furnaces,	Particulate matter, sulfur oxides Ash sulfur oxides, nitrogen oxides Sulfur oxides, nitrogen oxides, CO Hydrocarbons sulfur oxides CO SO ₂ , SO ₃ and H ₂ SO ₄ Particulate, matter gaseous fluoride Gaseous resin CO NO _x VOCs particulate matter

Table 2.1 Examples of sources of primary pollutants.

2.2.3. Pollutant measures

2.2.3.1. Concentration

It relates on the number of molecules of the particular gas or the mass of the gas molecules are in the sample volume of gas, and the total volume of the sample:

Concentration = Amount of substance / Volume occupied by the substance.

2.2.3.2. Mixing ratio

It gives the ratio of a particular substance to the sum of all of the other substances (e.g., "1 part in 10 parts", where there is, say, 10 grams of "A" and 100 grams of everything else):

Mixing ratio = Amount of a substance in a mixture / Amount of all substances in the Mixture

Typical mixing ratios for pollutants result in extremely small fractions. For this reason, fractions such as parts per million (ppm) or parts per billion (ppb) are often used. Specifications of whether we are referring to mass (ppmm) or volume (ppmv) mixing ratios are also determined:

$$\text{ppmv} = \frac{N(\text{cm}^3)}{10^6(\text{cm}^3)} \quad (2.1) \quad ; \quad \text{ppmm} = \frac{N(\text{kg})}{10^6(\text{kg})} \quad (2.2)$$

The transition from concentration unit $\mu\text{g}/\text{m}^3$ to mixing ratio unit ppb is performed through:

$$C[\mu\text{g} \cdot \text{m}^{-3}] = C[\text{ppb}] \frac{RT}{PM} \quad (2.3)$$

Where:

$R = 0.08314 \text{ hPa} \cdot \text{m}^3 \cdot \text{K}^{-1} \cdot \text{mol}^{-1}$

T is the temperature [K]

P is the pressure in [hPa]

M is the molecular weight of the substance. [$\mu\text{g} \cdot \text{mol}^{-1}$]

2.2.3.3. Residence time

It is the average time where a molecule or aerosol stay in the atmosphere after its emission from the source. For substances with well defined emission and sources rates, this is estimated by the ratio of the average global concentration of a substance to its production rate on a global scale. It is a function of not only the emission rates but the loss rates by chemical and physical removal processes. The residence time gives an indication of the accumulation of pollutants. (Table 2.2).

Species.	Concentration [ppm]	Residence time in the atmosphere
CO ₂	355	15 years
CH ₄	1.7	7 years
NO ₂	0.3	10 years
CO	0.05-0.2	65 days
SO ₂	10 ⁻⁵ -10 ⁻⁴	40 days
NH ₃	10 ⁻⁴ -10 ⁻²	20 days
O ₃	10 ⁻² -10 ⁻¹	Few days
NO _x	10 ⁻⁶ -10 ⁻²	1 day
HNO ₃	10 ⁻⁵ -10 ⁻³	1 day

Table 2.2 Orders of magnitude of the atmospheric pollutants' concentrations and their typical time of stay in the atmosphere. (Atmosphère météorologique et air humide J-F Sini, 2005)

2.3. Effects on pollutants dispersion

several parameters can affect the pollutants dispersion in the atmospheric from point or area sources, including atmospheric turbulence and stability, wind speed and direction, topography, atmospheric turbulence and atmospheric stability (David H.F. Lin, 2000).

2.3.1. Effects of wind speed and direction

Horizontal wind speed and direction play an important role in the dispersion and transformation of pollutants. When the wind speed increases, the air volume moving by a source during a given time also increases. If we have a constant emission rate, the double of wind speed value, halve the pollutant concentration, as the concentration is an inverse function of the wind speed. If we have a wind speed relatively constant, a similar area can be affected by high pollutant concentration. If we have a shifting wind direction, the pollutants propagated a long a big area, and as results the concentrations over large area are lower. Big changes of the wind direction can happen during short periods of time.

2.3.2.Effects of atmospheric turbulence

Near the surface of the Earth, air does not flow smoothly, it follows patterns of three-dimensional movement or the turbulence regime. Turbulence eddies are formed by two specific processes: the first one, thermal turbulence, resulting from atmospheric heating, and the second one: mechanical turbulence caused by the movement of air past an obstruction in a wind stream. Ordinarily the two types of turbulence happened in any atmospheric state. In a clear and sunny days with low wind speed, the thermal turbulence is dominant. While the mechanical turbulence appears with several atmospheric conditions, for example in windy nights and neutral atmospheric stability the mechanical turbulent dominant. Turbulence increase the dispersion operation although in mechanical turbulence, downwash from the pollution source can result in high pollution levels immediately downstream (David H.F. Lin, 2000).

2.3.3.Effects of atmospheric stability

In the troposphere, the vertical profile of temperature decreases with height to a level of about 10 km. this decrease is because of the reduced heating processes with vertical levels and radiative cooling of air and gets its maximum in the tropospheric higher levels. Temperature decrease with vertical level is described by the lapse rate. Temperature decreases by an average of $-0.65^{\circ}\text{C}/100\text{ m}$. which is the normal lapse rate. If warm dry air is lifted in a dry environment, it undergoes adiabatic expansion and cooling. These adiabatic cooling outcomes in a lapse rate of $-1^{\circ}\text{C}/100\text{ m}$, the dry adiabatic lapse rate.

Measured individual vertical temperature change from the dry or normal adiabatic lapse rate. This variation of measured temperature with height is the environmental lapse rate. The stability of the atmosphere is characterized by the values for the environmental lapse rates, which profoundly affect vertical air motion and the pollutants dispersion.

The characteristics of dispersion are good to excellent if the environmental lapse rate is greater than the dry adiabatic lapse rate. From the other side the atmosphere becomes stable, and the dispersion becomes more limited, if the environmental lapse rate is less than the dry adiabatic lapse rate. (David H.F. Lin, 2000).

2.3.4. Effects of topography on air motion and pollution

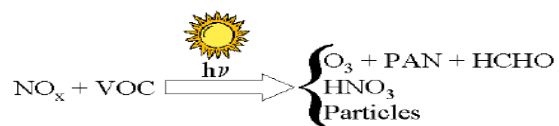
Micro and mesoscale air motion can be affected by topography near point and area sources. Circulations produced due to the complex topography in a region are very dependent with trapping of photochemical air pollution. The temporal and spatial variation of pollutant dispersion and concentration are very affected by the complex airflow configuration in a valley in the valley and also the surrounding mountains. In regions where the topography may limit or stop surface winds under anticyclonic conditions, the movement of pollutants can be trapped within confined or semi-confined air-sheds, which develop a serious pollution episodes. Because of previous conditions, a serious aspect relative to atmospheric chemistry is that air-mass aging can go on for days in the valleys, under oscillatory movements of limited amplitude, when new emissions are stay being added to the air-mass. These locally driven thermal circulations will be weaker in the winter time.

Urban areas located in valleys are, therefore, more affected by photochemical smog. Mountains and hills surrounding them reduce the air motion, permitting the concentration of pollutant to increase. Because strong temperature inversions can repeatedly develop in valleys, Valleys are sensitive to photochemical smog. During the day the air close to the ground is heated and as it warms it rises, taking the pollutants with it to higher levels. Temperature inversions can continue from a few days to many weeks. However, if a temperature inversion develops pollutants can be trapped near the ground. The reduction of atmospheric mixing is caused by the temperature inversions and therefore reduce the vertical dispersion of pollutants. (David H.F. Lin, 2000).

2.4. Photochemical pollution formation

Photochemical pollution is the air pollution which arises from the interaction of sunlight with various constituents of the atmosphere. The coupling of big human activities producing large amount of pollutants in the atmosphere with meteorology conditions as temperature, high solar radiation and weak wind, allow several chemical reactions in the lower atmosphere and producing large quantities of hazardous substances for health and environment [J.Kubler, 2001]. In the presence of nitrogen oxides NO_x ($\text{NO} + \text{NO}_2$) and hydrocarbons. The complex chemistry including the Volatile Organic Components and NO_x results the formation of ozone, in addition to a variety of other oxidizing species, the “*photochemical oxidants*”. The

photochemical smog also consists of organic nitrates, oxidized hydrocarbons, photochemical aerosols, SO_2 and CO . Most of present species in a smog phenomena are gases, in addition to some others, such as aldehydes, which present as small droplets. The following figure summarise the complex reaction chain:



Photochemical smog (figure 2.3) is one of the most dangerous effects of pollution in the atmosphere. It usually often arise over cities and urban areas as a gases chemical mixture that products a brownish-yellow haze. In very urbanised areas, with clear weather and trapping smog, serious air quality problems will appear. Photochemical smog is common in regions with high complex topography such as mountains that block air movement and meteorology conditions like temperature inversions in the troposphere contribute the air pollutants trapping.

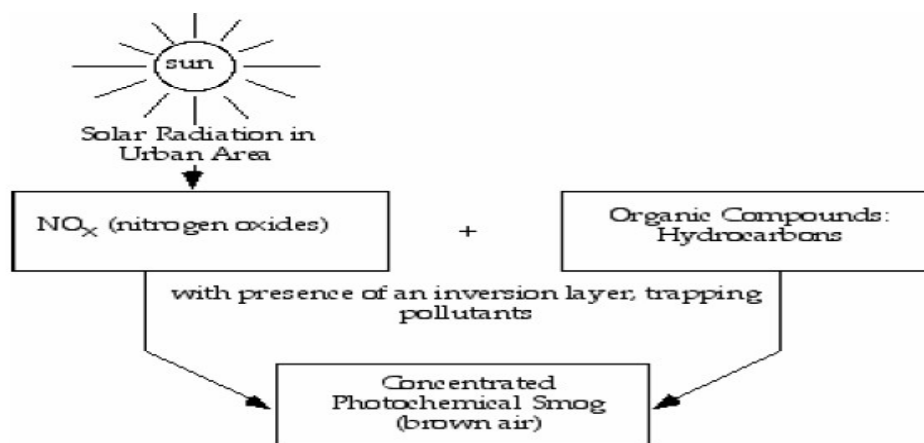


Figure 2.3 Simplified schematic representation of the photochemical smog formation.

2.4.1. Diurnal and seasonal variation of photochemical smog

2.4.1.1. Diurnal variation of ozone

A very important factor is the time of day which affect the amount of photochemical smog present (Figure 2.4).

- Early morning traffic increases the emissions of VOCs and NO_x when the people drive to go to work. An oxidation of NO to form NO₂.
- After that in the morning, traffic dies down and the VOCs and NO_x start to react forming NO₂, and increasing its concentration.
- When the sunlight becomes more intense later in the day, NO₂ amount is broken down and its by-products form increasing concentrations of O₃.
- At the same time, few amount of NO₂ react with the VOCs and produce toxic components such as PAN (peroxyacetyl nitrate).
- As the sun goes down, there is no production of O₃. The O₃ that remains in the atmosphere is then consumed by several different reactions.

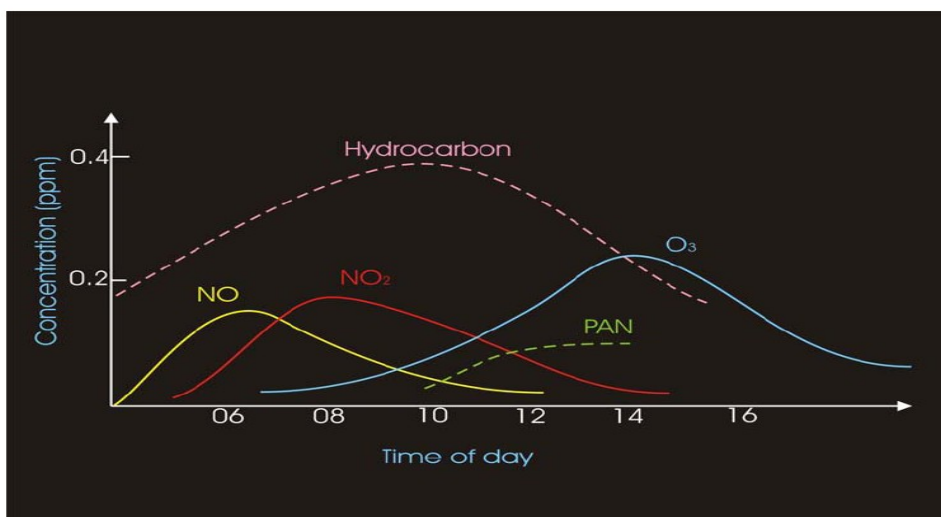


Figure 2.4 Diurnal cycle of O₃ and its precursors.

2.4.1.2. Seasonal variation of ozone

The ozone O₃ production rate during a seasonal cycle directly relates on the variations in sunlight intensity. Ozone O₃ obtains highest levels, and primary pollutants reach low

concentrations when the sun is most intense (i.e., in the summer), On the other hand, there is reduced of O_3 production in the winter, when the sun intensity is weak.

Primary pollutants, such as CO, obtain seasonal maxima during the winter. That is because the lower mixing heights during this season in addition to the reduced sunlight intensity. The low mixing heights effect is to reduce the volume of dispersion in which pollutants can mix, which increases the concentration if the source rate is the same.

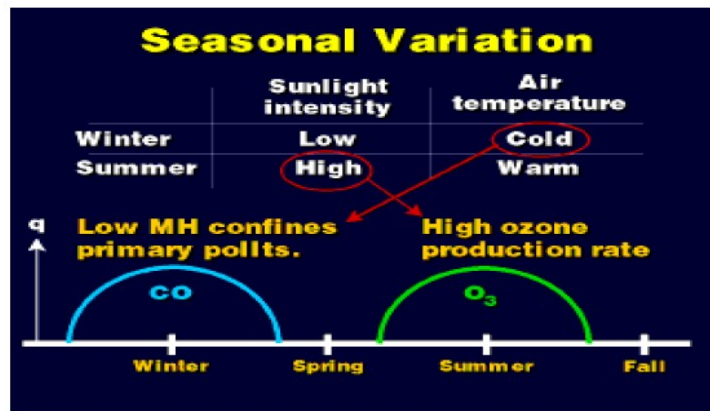


Figure 2.5 Schematic representation of the seasonal variation of ozone and a primary pollutant (CO).

2.5. Photochemical air quality modelling

2.5.1. Introduction

The large spectrum of atmospheric phenomena describing pollutants dispersion and concentration variate in time from seconds to years and in space scales from meters to thousand kilometers. It is very known to divide the atmospheric phenomena to micro, local, meso and global scale phenomena [J. Fenger, 1999].

Because of the numerous physical and chemical processes happen in the same time, the atmosphere is a very complex system. Measurements of atmospheric and chemical parameters lead to a momentarily view of the atmospheric conditions at a specific time and location. The numerical models allow the study of the atmospheric phenomena and chemical conditions and processes in a full integrated way. Through the spatial and temporal solution of equations describing the combination of all processes inside a model, we can understand each individual process in addition to the interactions between different processes. The best way to understand

and study the atmosphere, is the combined use of state-of-the-art models and state-of-the-art measurements.

2.5.2. Air Quality Models

Air quality models represent the good theoretical approach available currently in order to understand the atmosphere variation, and mainly the ozone levels to different air pollution control measures. These models include most of the physico-chemical processes governing formation, transport and fate of photochemical pollutants and allow reproducing and understanding multi-day air pollution episodes [J.Kubler, 2001] (Figure 2.6).

The air quality models inputs can be summarised in different groups based on: meteorology, emissions, topography, atmospheric concentrations and grid structure. Using those inputs an air quality model computes the spatial and temporal evolution of air pollutant concentrations, considering the main parameters affecting the pollutants dynamics, such as: diffusion, transport, the chemical and photochemical transformations and dry deposition.

The photochemical air quality model outputs are the resolved air pollution fields in time and space, describing the area response to an emission level. In order to evaluate the model ability to describe well the air pollution dynamics in a selected area, the model results are compared to a good documented historical episode. When the model assessment is finished it can be used to determine the airshed response to different emission control strategies.

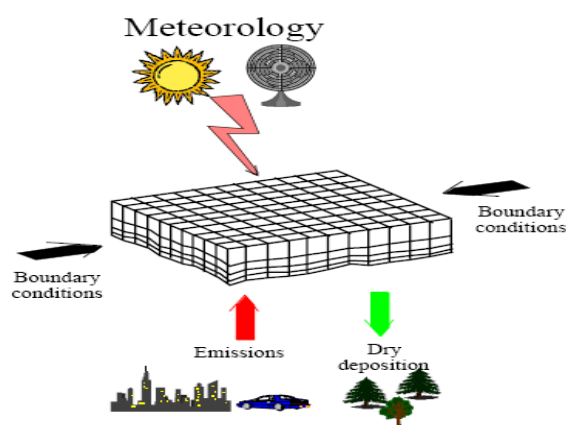


Figure 2.6 Eulerian three-dimensional photochemical model. (From. J.Kubler 2001)

2.5.3. Air quality models uncertainties

Even the huge number of developments in numerical field, modelling and simulations of air quality still suffer from many uncertainties due to the large range of scale and the complexity of physico-chemical phenomenon to be considered:

- Problem of uncertainties due to initial conditions, a lot of input data are not enough known like: ozone, VOC and Nox emissions, biogenic emissions, rainfall amount, cloud liquid water content. In addition to meteorological fields, which computed with numerical models that may be uncertain.
- Physico-chemical parametrizations produce a high sensitivity to the processing way and to the parameter values used to represent sub-grid processes.
- The numerical algorithms and the discretization can provoke uncertainties, mainly for low resolution because of the computational charge, especially for aerosols.

Even for a validated models, we must keep in mind that the amount of degrees of freedom is large mainly in parameterizations, and it is possible to measure only a small number of model outputs. For instance, most of the used chemical transport models have been extensively tuned to meet acceptable model-to-data error statistics for ozone peaks at ground. It does not ensure that the model outputs are satisfactory for 3D fields and other trace substances. There is therefore a problem of applying “overtuned” models, mainly for impact studies or long-term scenario studies (Sportisse, 2007).

2.5.4. Air Quality management

The physico-chemical processes side is not enough to develop an emission control strategy in order to decrease photochemical pollutants ambient concentrations, but also from the technological, social and economical point of view. The air quality management is a complex subject involving diverse topics [J.Kubler, 2001]. A collaboration must be done between the specialists of all topics in order to choose the most acceptable control strategy from a techno-economic and a social point of view. This process shown as a feedback loop in Figure 2.7, first the estimation of temporal and spatial of emission inventory distribution is required in the considered region. The air quality model is then applied to transform the emissions distribution into a pollutant dispersion through numerical simulation of the chemical transformation and physical transport of substances leans on meteorological description of

selected previous episodes. Then the pollutant distribution resulted is evaluated, and if the planned objective is not met, the developed control strategy is modified taking into account techno-economical feasibility and the political affects, next the new developed emission inventory is tested with the air quality model. This process will repeated until air quality aims are satisfied; regulations are after that considered to meet the emission goal in the control strategy analysis.

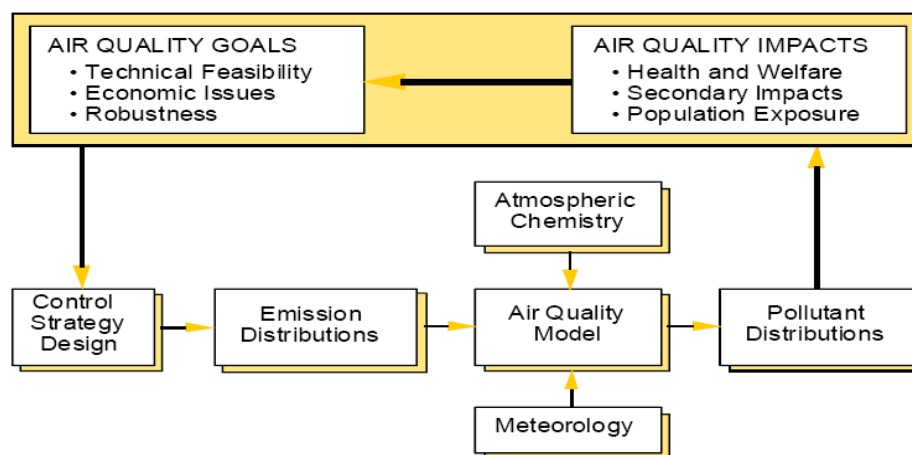


Figure 2.7 Diagram of the basic concepts on the role of air quality modelling.

Photochemical models are used in Eulerian, Lagrangian or Hybrid, Eulerian and Lagrangian mode. Lagrangian models describe the motion of an air parcel in the atmosphere and the chemical transformation that happened during the advection. In a Lagrangian model there is no mass exchange between the parcel and its surroundings, except for the emissions that can enter the substance. A Lagrangian model simulates concentrations at various regions and times.

Eulerian models describe the concentration of substance in an array of fixed computational cells. The concentration in an Eulerian model simulated at all locations in function of time. In general Eulerian models are examined that it is technically better and permit comprehensive, explicit processing of physical and chemical treatment. In addition in an Eulerian framework, the interactions of different sources are permitted. These models need good solution methods, using discrete time steps and operator splitting, they use a computational grid which is very cost to apply for a long time. Subgrid resolution can be a limitation because when the size of the grid and the time step areas grid size and time step are

reduced precision increases, in the same time the computation time is increases. Advanced grid models use variable grid spacing or nesting which ameliorates the precision in critical regions and permits the application of cost effective on the atmospheric scales from urban to regional. In a Hybrid model characteristics of Lagrangian types are mixed into an Eulerian framework. These models overcome many of the sub-grid model limitations and many of the prior practical advantages of Lagrangian models, by the development of nested grid resolution and techniques of source apportionment.

Models can also be distinguished according to the computational domain, the model use and duration. Table 2.3 presents different types of models based on the domain size and time scale. The domain of computational consists of cells with specific sizes. The cells size, is the volume in which the components concentration is averaged, determines the spatial resolution of the model. Concerning the resolution in space, with the use of a photochemical model different scales of phenomena can be analyzed.

TEMPORAL SCALE \ SPATIAL SCALE	1 MONTH	1 DAY	1 HOUR	1 MINUTE	1 SECOND	
10000 Km	STANDING WAVES	ROSSBY WAVES				Macro- α
2000 Km		BAROCLINIC WAVES				Macro- β
200 Km		FRONTS	HURRICANES			Meso- α
20 Km			CLOUD CLUSTERS			Meso- β
2 Km				THUNDER STORMS		Meso- γ
200 Metres				HEAT ISLAND EFFECTS		Micro- α
20 Metres				TORNADOES		Micro- α
				DEEP CONVECTIVE SYSTEMS		Micro- α
				DUST DEVILS		Micro- β
				THERMALS		Micro- β
					PLUMES	Micro- γ
					TURBULENCE	Micro- γ
					ROUGHNESS	Micro- γ
	CLIMATOLOGICAL SCALE	SYNOPTIC PLANETARY SCALE	MESO SCALE	MICRO-SCALE		SCALE DEFINITION

Table 2.3 Scale definitions and different processes with characteristic time and horizontal scales. (After Atkinson, 1981).

2.5.5. 3D Photochemical models requirements

several input parameters are required during the use of a photochemical air quality model, such as meteorological fields parameters: wind speed and direction, humidity, temperature, pressure, stability, substances emissions, in addition to initial and boundary concentration for each components.

Modules used in photochemical model are:

1. Emissions modelling system to create emissions fields for every substances.
2. Meteorological Modelling system to produce meteorological fields.
3. Preprocessors for other initial conditions to the photochemical model.
4. The Air Quality Model.
5. Post-Processors and Visualization.

Figure 2-18 shows a diagram describing the general structure of a photochemical model. The quality of the photochemical model results depend to the initial parameters, the inputs parameters are:

Meteorology: 3-D temperature, winds, humidity, turbulence.

Emissions: Temporally and spatially defined.

Topography: Landuse, surface roughness, altitude.

Initial and Boundary Conditions: Gridded array of species concentration for the 1st hour of the simulation, array of substances concentration for each hour of the simulation at the the domain boundaries.

Photolysis rates file: Photolysis rates for the photochemical reactions in the model.

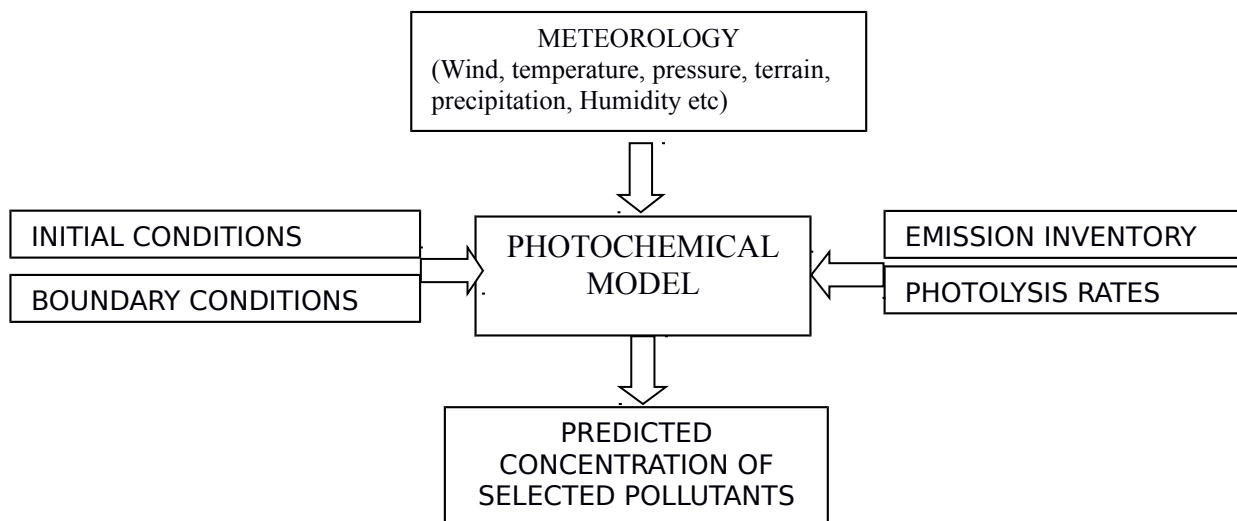


Figure 2.8 Schematic diagram of the general structure of a photochemical model.

2.5.6. Model formulation steps

Many steps are required in a model simulation design, application and testing. Below we present an example of the steps can followed:

- Definition and comprehension of the problem of interest.
- Determination of the problem scale in time and space.
- Determination of the dimension of the model.
- Selection of the processes to simulate: physical, chemical and dynamical.
- Variables Selection.
- Selection of time steps and intervals.
- Setting of initial conditions.
- Setting of boundary conditions.
- Obtainment of initial data.
- Obtainment of ambient data for comparison.
- Interpolation of input data and model predictions.
- Development of statistical and graphical techniques.
- Comparison of simulated results against experimental data.
- Sensitivity tests and data.
- Improvement of algorithms.

2.6. Consequences of photochemical pollution

Photochemical air pollution reduces visibility, has harmful effects on human health, damages plants, and degrades various materials. Ozone easily reacts with organic materials accelerating the deterioration of rubber, fibres, plastics, paints, and dyes.

2.6.1. Damage on human health

Photochemical smog is characterised by high concentration of ozone O_3 in atmosphere. The formation of photochemical smog's effects differ naturally depending to many conditions such as the concentration of contaminants, exposure time and human factors such as the condition of health, gender, age. In addition the eyes, nose and throat can irritated with the low

concentrations of ground-level ozone. When the photochemical smog increases, it can causes many serious problems for health involving:

- Bronchitis, Asthma,, Coughing, and chest pain, in addition to other chronic conditions;
- Increased susceptibility to respiratory infections;
- Reduce physical performance and lung function.

Prolonged exposure can eventually damage lung tissue, cause premature aging of the lungs, and contribute to chronic lung disease, in the same time it is possible to increase susceptibility to cardio-respiratory diseases. Children, the elderly, and people with impaired lung function are are the more affected by air pollution risk. In the USA, 14 million adults with asthma (6.9 %), 6.3 million (8.7 %) children with asthma have been reported in 2001. In the same year 4,269 deaths resulted by air pollution were estimated. Table 2.4 summarizes the sources, health and welfare effects for selected pollutants (US EPA website) .

Pollutant	Description	Sources	Health Effects	Welfare Effects
CO	Colorless, odorless gas	Motor vehicle exhaust, indoor sources include kerosene or wood burning stoves.	Headaches, reduced mental alertness, heart attack, cardiovascular diseases, impaired fetal development, death.	Contribute to the formation of smog.
SO2	Colorless gas that dissolves in water vapor to form acid, and interact with other gases and particles in the air.	Coal-fired power plants, petroleum refineries, manufacture of sulfuric acid and smelting of ores containing sulfur.	Eye irritation, wheezing, chest tightness, shortness of breath, lung damage.	Contribute to the formation of acid rain, visibility impairment, plant and water damage, aesthetic damage.
NO2	Reddish brown, highly reactive gas.	Motor vehicles, electric utilities, and other industrial,	Susceptibility to respiratory infections, irritation of the lung and	Contribute to the formation of smog, acid rain, water quality

		commercial, and residential sources that burn fuels.	respiratory symptoms (e.g., cough, chest pain, difficulty breathing).	deterioration, global warming, and visibility impairment.
O₃	Gaseous pollutant when it is formed in the troposphere.	Vehicle exhaust and certain other fumes. Formed from other air pollutants in the presence of sunlight.	Eye and throat irritation, coughing, respiratory tract problems, asthma, lung damage.	Plant and ecosystem damage, climate change.
VOC	Gaseous pollutants	Vehicle exhaust, home products, industrial plants, vegetations.	Eye irritation (e.g., acrolein), cancer (e.g., benzene, formaldehyde)	
PM	Very small particles of soot, dust, or other matter, including tiny droplets of liquids.	Diesel engines, power plants, industries, windblown dust, wood stoves.	Eye irritation, asthma, bronchitis, lung damage, cancer, heavy metal poisoning, cardiovascular effects.	Visibility impairment, atmospheric deposition, aesthetic damage.
Pb	Metallic element	Metal refineries, lead smelters, battery manufacturers, iron and steel producers.	Anemia, high blood pressure, brain and kidney damage, neurological disorders, cancer, lowered IQ.	Affects animals and plants, affects aquatic ecosystems, climate change.

Table 2.4 Sources, health and welfare effects for selected Pollutants (Ref: US EPA website).

2.6.2. Damage on the environment and ecosystems

According to literature, ozone is the pollutant having the strongest adverse action on vegetation. It lowers the Plant ability to produce and store the energy needed for their development and weaken their resistance to diseases and hard climatic conditions [J.Kubler, 2001].

At lower ozone concentrations some products like sensitive crops, trees, and other vegetation are harmed more than human health. In addition other plants are also sensitive to ozone such as tobacco, spinach, tomato, and pinto beans. Harmed leaves develop necrotic patterns – brown specks that turn yellow – on the upper surface of their leaves. Te ozone at the lower level reduce growth, productivity, and reproduction, damage leaves. It can cause vulnerability to insects, disease, and even death.

The most evident effect of photochemical smog is the reduce of visibility. It is due to the absorption and diffusion of light by gases and particles. Diffusion by PM10 causes 50 to 95% of the total extinction due to air pollution, particles smaller than 1 μ m contributing more strongly to light diffusion. In some regions in the United States air pollution reduces the visibility form 150 km to around 70 km [J.Kubler, 2001].

Besides, Nitrogen oxide engage to the creation of acid rain, allow the accumulation of nitrates in the ground and in water, can cause alterations of the environmental ecological equilibriums.

CHAPTER 3

DYNAMICS IN THE ATMOSPHERIC BOUNDARY LAYER

3.1.Introduction

The lowest layer of the atmosphere is called the troposphere. The troposphere can be divided into two parts: the atmospheric boundary layer (ABL), also known as the planetary boundary layer (PBL), extending upward from the surface to a height that ranges anywhere from 100 to 3000 m, and above it, the free atmosphere. The atmospheric boundary layer (ABL), as defined by Stull (1988), “is the part of the troposphere that is directly influenced by the presence of the Earth's surface, and responds to surface forcing with a time scale of about one hour or less”. Each of these forcings (as frictional drag, solar heating, and evapotranspiration) generates turbulence of various-sized eddies, which can be as deep as the boundary layer itself, lying on top of each other.

3.2.Time and space scales

The vertical structure of the atmosphere is characterised by many layers, with different time, vertical distance and horizontal distance scales (table 3.1). The effect of Earth surface roughness is limited to the troposphere level (the first 10 km above the ground of the atmosphere). According to table 1, on the time scale of one day, this influence is limited to a smaller zone, the atmospheric boundary layer, which is characterised by total mixing due to frictional drag. The planetary boundary layer gets most of its heat and all of its water through the turbulent processes. The height of the boundary layer is not constant and it depends on turbulence.

Layer	Time	Horizontal distance	Vertical distance
Troposphere	<i>Days</i>	<i>~ 500 km</i>	<i>~ 10 km</i>
Atm. Boundary Layer	<i>~ 1 hour</i>	<i>~ 50 km</i>	<i>~ 1km</i>
Surface layer	<i>~ 10 minutes</i>	<i>~ 1 km</i>	<i>10-100 m</i>
Roughness layer	<i>Seconds</i>	<i>1-5 elem. height</i>	<i>1-5 elem. height</i>

Table 3.1 Time and distance magnitude scales for atmospheric layers (Antonacci G 2005).

In a one day period, when the sun heats the ground, the upward transfer of heat into the cooler atmosphere improve the convection and the boundary layer depth is extended by $1 \div 2$ km. In the night time the ground is cooler than the atmosphere; therefore, the downward heat transfer suppresses mixing and the boundary layer may shrink to less than 100 m. The daily cycle can troubled by large scale weather events not depends to the configuration of the local surface or heating cycle. The higher horizontal scale limit of atmospheric boundary layer is 50 km, while the vertical scale limit is around 1 km. The turbulent surface layer is characterized by heavy small-scale turbulence produced by the surface roughness in addition to convection, which shows strong fluctuations during a limited periods of time (seconds). At the day time its maximum is about 50 m while during night-time becomes few meters. The depth of the atmospheric boundary layer may vary in space due to the characteristics of the orography. Moreover, the structure of the layer changes during the day. According to Stull (1988) three main patterns can be distinguished (figure 3.1): the mixed layer, the residual layer and the stable boundary layer .

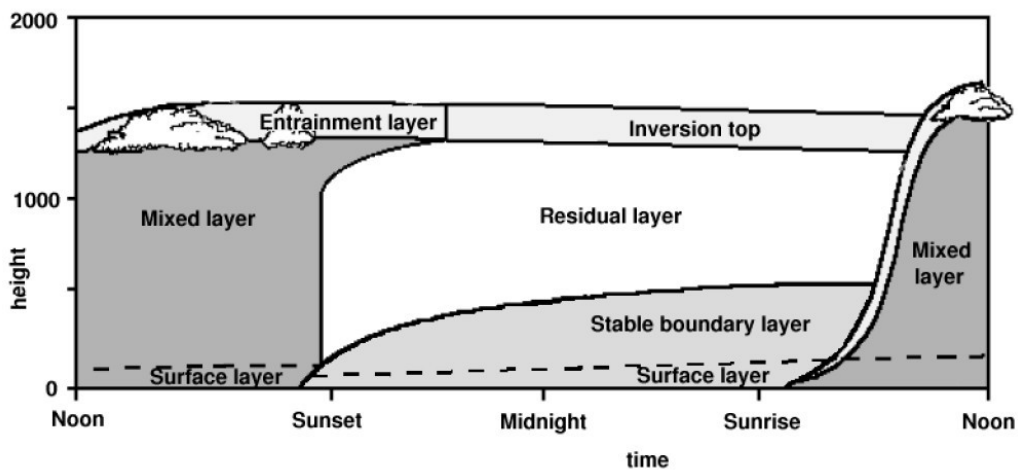


Figure 3.1 Daily evolution of the atmospheric boundary layer (Stull, 1988).

3.3. Basic Equations of Atmospheric Fluid Mechanics

In this section we present the equations of: continuity, motion, and energy that govern the fluid density, temperature, and velocities in the lowest part of the atmosphere. Subsequently these equations will form the basis from which the processes that influence the atmospheric turbulence can explore.

First, the equation of continuity for a compressible fluid:

$$\frac{\partial \rho}{\partial t} + \frac{\partial}{\partial x_1}(\rho u_1) + \frac{\partial}{\partial x_2}(\rho u_2) + \frac{\partial}{\partial x_3}(\rho u_3) = \frac{\partial \rho}{\partial t} + \frac{\partial}{\partial x_i}(\rho u_i) = 0 \quad (3.1)$$

where ρ is the fluid density and u_1, u_2, u_3 are the fluid velocity components in the directions $x, y,$ and $z,$ respectively.

The second equation is the equation of motion of a compressible, Newtonian fluid in a gravitational field, in this equation the Coriolis acceleration is neglected because we are interested only in processes taking place on limited spatial and temporal scales over which the air motion is not influenced by the rotation of the Earth.

$$\rho \left(\frac{\partial u_i}{\partial t} + u_j \frac{\partial u_i}{\partial x_j} \right) = \frac{\partial}{\partial x_k} \left[\mu \left(\frac{\partial u_i}{\partial x_k} + \frac{\partial u_k}{\partial x_i} \right) \right] - \left(P + \frac{2}{3} \mu \frac{\partial u_j}{\partial x_j} \right) \delta_{ik} - \rho g \delta_{3i} \quad (3.2)$$

where μ is the fluid viscosity and δ_{ij} is the Kronecker delta, defined by $\delta_{ij} = 1$ if $i = j$, and $\delta_{ij} = 0$ if $i \neq j$.

Finally the equation of energy, supposing that the contribution of viscous dissipation to the energy balance of the atmosphere is negligible, is:

$$\rho c_v \left(\frac{\partial T}{\partial t} + u_j \frac{\partial T}{\partial x_j} \right) = \lambda \frac{\partial^2 T}{\partial x_j \partial x_j} - P \frac{\partial u_j}{\partial x_j} + Q \quad (3.3)$$

where c_v is the heat capacity of air at constant volume per unit mass, λ is the thermal conductivity (constant) and Q represents the heat generated by any sources in the fluid.

Equations (3.1), (3.2), and (3.3) represent five equations for the six unknowns $u_1, u_2, u_3, p, \rho,$ and $T.$ The sixth equation necessary for closure is the ideal-gas law:

$$P = \frac{\rho R T}{M_{air}} \quad (3.4)$$

These six previous equations can be solved, in principle, subject to appropriate initial and boundary conditions to give pressure, velocity, density and temperature distribution in the atmosphere. Equations (3.1), (3.2), and (3.3) can be simplified for a superficial atmospheric layer near to the ground using the Boussinesq approximations. The fundamental opinion of these approximations is to first define the equilibrium profiles of temperature, pressure, and density as functions of the vertical coordinate x_3 as follows:

$$\begin{aligned} P_e &= P_0 + P_m(x_3) \\ \rho_e &= \rho_0 + \rho_m(x_3) \\ T_e &= T_0 + T_m(x_3) \end{aligned} \quad (3.5)$$

We consider only a superficial layer, so the ratios p_m/p_0 , ρ_m/ρ_0 , and T_m/T_0 are all smaller than unity. While a movement, we can define the actual density, pressure and temperature as the sum of the values in equilibrium and a small correction due to the motion. Thus we write:

$$\begin{aligned} P(x_1, x_2, x_3, t) &= P_0 + P_m(x_3) + \tilde{P}(x_1, x_2, x_3, t) \\ \rho(x_1, x_2, x_3, t) &= \rho_0 + \rho_m(x_3) + \tilde{\rho}(x_1, x_2, x_3, t) \\ T(x_1, x_2, x_3, t) &= T_0 + T_m(x_3) + \tilde{T}(x_1, x_2, x_3, t) \end{aligned} \quad (3.6)$$

where we suppose that the deviations induced by the movement are sufficiently small that the quantities \tilde{P}/P_0 , $\tilde{\rho}/\rho_0$, and \tilde{T}/T_0 are also small than the unity. Substituting (3.6) into (3.1), (3.2), and (3.3) and simplifying using the assumptions presented previously, the fundamental equations of atmospheric fluid mechanics that are applicable for a superficial atmospheric layer:

$$\frac{\partial u_i}{\partial x_i} = 0$$

$$\frac{\partial u_j}{\partial t} + u_j \frac{\partial u_i}{\partial x_j} = -\frac{1}{\rho_0} \frac{\partial \tilde{P}}{\partial x_i} + \frac{\mu}{\rho_0} \frac{\partial^2 u_i}{\partial x_j \partial x_j} + \frac{g \tilde{T}}{T_0} \delta_{i3} \quad (3.7)$$

$$\rho_0 c_p \left(\frac{\partial \theta}{\partial t} + u_j \frac{\partial \theta}{\partial x_j} \right) = \lambda \left(\frac{\partial^2 \theta}{\partial x_j \partial x_j} \right) + Q$$

where θ is the potential temperature, with $\theta = T(P_0/P)^{R/(c_p M_{air})} = T(P_0/P)^{0.286}$. An important simplification of the original equations are done because of the Boussinesq approximations. The first is the continuity equation for an incompressible fluid. The equation of motion is the same as the incompressible form of the equation except the last term, which accounts for the acceleration because of forces of buoyancy. Finally, the energy equation is the known heat conduction equation replacing T by θ . The complete set of equations composed from the five equations in (3.7) for the five unknowns, u_1 , u_2 , u_3 , ρ , and θ . The ideal-gas equation of state is no needed now, as it has been incorporated into the equations. With ρ_0 and T_0 in (3.7) describe the constant surface values, equations of precisely the same form can be derived in which ρ_0 and T_0 are replaced by ρ_e and T_e , the reference profiles.

3.3.1. Equations for the Mean Quantities

Since the atmospheric flow is turbulent (not laminar), the dependent variables u_i , p and θ to the equations of motion and energy (3.7) are random variables, and therefore the equations are impossible to solve virtually. Which implies to modify trying to compute the variables to trying to estimate their mean values. Fluid characteristics are decomposed into a mean value and fluctuatin:

$$u_i = \bar{u}_i + u'_i$$

$$\theta = \bar{\theta} + \theta'$$

$$p = \bar{p} + p'$$
(3.8)

Where the mean of the fluctuation is equal to zero: $\bar{u}'_i = \bar{\theta}' = \bar{p}' = 0$ in order to obtain the equations for $\bar{u}_i, \bar{\theta}, \bar{p}$ we substitute (3.8) into (3.7), the resulting equations are:

$$\frac{\partial \bar{u}_i}{\partial x_i} = 0$$

$$\frac{\partial}{\partial t}(\rho_0 \bar{u}_i) + \frac{\partial}{\partial x_j}(\rho_0 \bar{u}_i \bar{u}_j) = \frac{-\partial \bar{p}}{\partial x_i} + \frac{\partial}{\partial x_j} \left(\mu \frac{\partial \bar{u}_i}{\partial x_j} - \rho_0 \overline{\dot{u}_i \dot{u}_j} \right) + g \frac{\bar{\theta}}{T_0} \delta_{i3} \quad (3.9)$$

$$\rho_0 c_p \left(\frac{\partial \bar{\theta}}{\partial t} + \bar{u}_j \frac{\partial \bar{\theta}}{\partial x_j} \right) = \frac{\partial}{\partial x_j} \left(k \frac{\partial \bar{\theta}}{\partial x_j} - \rho_0 c_p \overline{\dot{u}_j \dot{\theta}} \right)$$

We note a new dependent variables $\overline{\dot{u}_i \dot{u}_j}, \overline{\dot{u}_j \dot{\theta}}$ for $i, j = 1, 2, 3$ when the equations written in the form (3.9). $\rho_0 \overline{\dot{u}_i \dot{u}_j}$ represent a new contribution to the total stress tensor and that $\rho_0 c_p \overline{\dot{u}_j \dot{\theta}}$ is a new contribution to the heat flux vector.

3.3.2. Mixing-Length Models for Turbulent Transport

If we assume a steady turbulent shear flow in which $\bar{u}_1 = \bar{u}_1(x_2) \wedge \bar{u}_2 = \bar{u}_3 = 0$. We suppose first turbulent momentum transport, that is, the Reynolds stresses. The mean flux of x_1 momentum in the x_2 direction due to turbulence is $\rho_0 \overline{\dot{u}_1 \dot{u}_2}$. As a prediction for this flux. The mixing length Le is a measure of the maximum distance in the fluid over which the velocity fluctuations are correlated, or in some sense, of the eddy size. The experimental computation of Le includes the measurement of the velocities at two separated points by big distance until the correlation between them is zero.

$$\overline{\dot{u}_1 \dot{u}_2} = \overline{\dot{u}_2} l \frac{\partial \bar{u}_1}{\partial x_2} \quad (3.10)$$

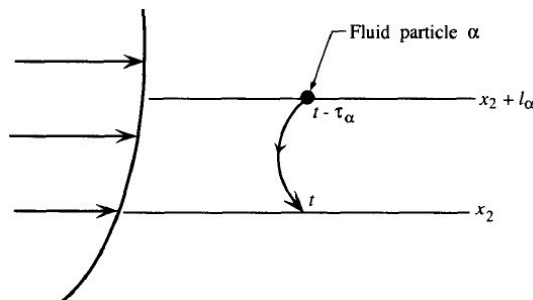


Figure 3.2 Eddy transfer in a turbulent shear flow

The term $\overline{u_2 l}$ indicates the correlation between the fluctuating x_2 velocity at x_2 and the distance of travel of the eddy. To predict the order of the term $\overline{u_2 l}$. First note that if

$\frac{\partial \bar{u}_1}{\partial x_2} > 0$, then from (3.10) $\overline{u_2 l}$ will have the same sign as $\overline{u_1 u_2}$, that is, it will be negative. If Le is the maximum distance over which an eddy keeps its integrity and \hat{u}_2 is the turbulent intensity $(\overline{u_2^2})^{1/2}$, then the term $\overline{u_2 l}$ will be proportional to $Le \hat{u}_2$ or if c is a positive constant of proportionality, then:

$$\overline{u_1 u_2} = -c L_e \hat{u}_2 \frac{\partial \bar{u}_1}{\partial x_2} \quad (3.11)$$

From (3.11), we determine the eddy viscosity or turbulent momentum diffusivity K_M as $K_M = c L_e \hat{u}$, so the equation (3.11) becomes:

$$\overline{u_1 u_2} = -K_M \frac{\partial \bar{u}_1}{\partial x_2} \quad (3.12)$$

We can extend the mixing-length concept to the turbulent heat flux. By analogy to the definition of the eddy viscosity, we can define an eddy viscosity for heat transfer by:

$$\overline{u_1 u_2} = -K_T \frac{\partial \bar{u}_1}{\partial x_2} \quad (3.13)$$

Equations (3.12) and (3.13) give a solution to the closure problem inasmuch as the turbulent fluxes have been related directly to the mean velocity and potential temperature. Substitution of these relations into (3.9) allows to closed equations for the mean quantities (Seinfeld and Pandis 2006).

3.3.3. Variation of wind with height in the atmosphere

According to literature (e.g. Seinfeld and Pandis 2006), the atmosphere near the surface of the Earth can be discomposed into four layers: the free atmosphere, the Ekman layer, the surface layer and the laminar sub-layer. The laminar sub-layer thickness is less than a centimetre, and this layer can be neglected in the present discussion. Practically the surface layer variates from the ground to a height of 30-50 m. along this layer, the vertical turbulent fluxes of momentum and heat are considered constant with height, and they also define the range of this region. The Ekman layer goes to a height of 300-500 m depending on the type of terrain, with the biggest thickness at the more uneven terrain. The wind direction in this

layer is affected by the rotation of the Earth. In the Ekman layer the wind speed is generally increases quickly with height; however, the rate lessens near the free atmosphere.

If we take in account the variation of wind with height in the surface and Ekman layers, which constitute the atmospheric boundary layer. Our interest goes mostly to the surface layer, which is the region where the pollutants are first released usually.

The vertical distribution of wind velocity depends on some parameters, involving the surface roughness and the atmospheric stability. The surface roughness is usually characterized by the roughness elements height: buildings, grass, trees ... etc. Usually these elements are very near to each other, that the important is only their height and spacing. Generally, smooth surfaces allow the establishment of a laminar sub-layer in which they are submerged. At the other side, in a rough surface, the roughness elements height blocks the creation of the laminar sub-layer, so that the flow regime is turbulent inside the roughness elements. The laminar sub-layer depth, and thus the classification if the surface is rough or smooth, can be determined according to the Reynolds number of the flow.

3.3.3.1. Mean Velocity in the Adiabatic Surface Layer over a Smooth Surface

If we consider a ground-parallel flow of air on an homogeneous flat surface. If the wind flow is in the x direction ($\bar{u}_y=0$) and $\bar{u}_x=\bar{u}_x(z)$, taking that the vertical temperature profile is adiabatic, the formula of the mean velocity profile $\bar{u}_x(z)$ can be calculated by:

$$\bar{u}_x(z) = u_* \left(\frac{1}{k} \ln \left(\frac{u_* z}{\nu} \right) + 5.5 \right) \quad (3.14)$$

where u_* is the characteristic velocity of the flow, which depends on the turbulence $\overline{u'_x u'_z}$ flux and is called the friction velocity, it is actually equal to $\sqrt{\tau_0/\rho}$ where τ_0 is the shear stress at the surface, The friction velocity can be computed from an actual measurement of the velocity at a given height. ν is the kinematic viscosity and k is the von Karman constant (0.4). Since all the actual surface are roughness, Equation (3.14) has limited utility in the real atmosphere.

3.3.3.2. Mean Velocity in the Adiabatic Surface Layer over a Rough Surface

In the case of a surface with roughness elements of height ϵ . In this case there is no laminar sub-layer so the use of the kinematic viscosity is not needed and the mean velocity profile $\bar{u}_x(z)$ is:

$$\bar{u}_x(z) = \frac{u_*}{k} \ln \frac{z}{z_0}, z > z_0 \quad (3.15)$$

With z_0 is the roughness length which is related to the height of the roughness element ϵ , which found experimentally that $z_0 \approx \epsilon/30$. This equation is valid only for heights significantly greater than the roughness length, because according to the equation 3.15 when $z = z_0$ we have $\bar{u}_x = 0$.

Commonly, the friction velocity u_* is obtained from a measurement of the velocity at some reference height h_r , often equal to 10m. Then, if $\bar{u}_x(h_r)$ is known, u_* value is:

$$u_* = \frac{k \bar{u}_x(h_r)}{\ln(h_r/z_0)} \quad (3.16)$$

3.3.3.3. Mean Velocity Profiles in the Nonadiabatic Surface Layer

Because the atmosphere is rarely adiabatic, the velocity profiles for stable and unstable conditions can not computed from the previous logarithmic law (equation 3.15). For the more frequently encountered nonadiabatic atmosphere (stratified), the Monin-Obukhov similarity theory is usually used

Depending Monin-Obukhov similarity theory, the characteristics of turbulence in the surface layer are conducted generally by the following seven variables: $\partial \bar{u}_x / \partial z$, z , z_0 , u_* , p , (g/T_0) , and $\bar{q}_z = \rho c_p \overline{u_z \theta}$, (g/T_0) is a parameter related to buoyancy, and q_z is the vertical mean turbulent flux. Considering that the roughness length z_0 variations do not affect the velocity profile form but only shift them, we can neglect this parameter and limit the list to six variables. In the problem there are four dimensions (length, mass, time and temperature), so, according to the Buckingham π theorem, the behaviour of the system is governed by two dimensionless groups. The first one is the flux Richardson number (Rf) defined as:

$$Rf = \frac{-k g z \bar{q}_z}{\rho \hat{c}_p T_0 u_*^3} \quad (3.17)$$

where $k = 0.4$ is the von Karman constant. The flux Richardson number is equal to the ratio of the production of turbulent kinetic energy by buoyancy to its production by shear stresses. Rf can be positive or negative depending on the sign of the vertical mean turbulent flux $\bar{q}_z = \rho c_p \overline{u_z \theta}$. There are three cases:

- If $Rf < 0$, this case corresponds to an unstable atmosphere.
- If $Rf > 0$, the atmosphere is stable.
- If $Rf = 0$, this case corresponds to an adiabatic atmosphere (neutral).

The flux Richardson number according to (3.17) is a function of the distance from the ground. Because it is dimensionless, it can actually be viewed as a dimensionless length:

$$Rf = \frac{z}{L} \quad (3.18)$$

where L is the Monin-Obukhov length and according to (3.17) and (3.18) is given by:

$$L = - \frac{\rho c_p T_0 u_*^3}{k g \bar{q}_z} \quad (3.19)$$

The Monin-Obukhov length is the height at which the production of turbulence by both mechanical and buoyancy forces is equal to each other. Like the flux Richardson number, the L parameter, determine the stability of the surface layer (Table 3.2).

L		Stability condition
Very large negative	$L < -10^5$ m	Neutral
Large negative	-10^5 m \leq L \leq -100 m	Unstable
Small negative	-100 m $<$ L $<$ 0	Very Unstable
Small positive	$0 <$ L $<$ 100 m	Very stable
Large positive	100 m $<$ L $<$ 10^5 m	Stable
Very large positive	$L >$ 10^5 m	Neutral

Table 3.2 Monin-Obukhov Length L with Respect to Atmospheric Stability (Seinfeld and Pandis 2006)

In this case the wind velocity vertical profile is related to stability through the following equation:

$$\frac{kz}{u_*} \frac{\partial \bar{u}_x}{\partial z} = \Phi\left(\frac{z}{L}\right) \quad (3.20)$$

Accepted forms of the universal function are $\Phi(\beta)$ with $\beta = \frac{z}{L}$ those of Businger et al. (1971):

$$\text{Stable, } \beta > 0, \Phi(\beta) = 1 + 4.7\beta$$

$$\text{Neutral, } \beta = 0, \Phi(\beta) = 1 \quad (3.21)$$

$$\text{Unstable, } \beta < 0, \Phi(\beta) = (1 - 15\beta)^{-1/4}$$

The velocity $\bar{u}_x(z)$ can be determined by integrating (3.20) from $z = z_0$ and $u_x = 0$ using (3.21).

$$\bar{u}_x(z) = \int_{z_0/L}^{z/L} \frac{\Phi(\beta)}{\beta} d\beta \quad (3.22)$$

$$\text{For neutral conditions: } \bar{u}_x(z) = \frac{u_*}{k} \ln \frac{z}{z_0} \quad (3.23)$$

$$\text{For stable conditions: } \bar{u}_x(z) = \frac{u_*}{k} \ln \frac{z}{z_0} + 4.7 \frac{u_* z}{k} \quad (3.24)$$

$$\text{For unstable conditions: } \bar{u}_x(z) = \frac{u_*}{k} \int_{z_0/L}^{z/L} \frac{d\beta}{\beta(1-15\beta)^{-1/4}} \quad (3.25)$$

3.4. Atmospheric stability

As described above, atmospheric stability values and functions are determined using standard similarity theory profiles (the Monin-Obukhov length) equation 3.19. If the sensible heat flux \bar{q}_z is positive or directed away from the surface it results unstable conditions ($L < 0$), in the case when it is negative or directed toward the ground, it is associated with stable conditions ($L > 0$).

A physical description of L can be presented as follows:

- In unstable conditions, $-L$ is the range from the surface above which convective turbulence is more important than mechanical shear stress because of the surface friction.
- In stable conditions, L is the vertical distance above which the vertical turbulent motion is very inhibited because of the stable stratification.

As described in the previous section, the the velocity profile shape changes with the atmospheric stability, figure 3.3 illustrates the wind velocity profile variation with the change of the eddies' shape. Under unstable conditions, the shape of the profile variates because the shape of the eddies is stretched. On the contrary, under stable condition, the eddies are compacted as shown in figure 3.3.

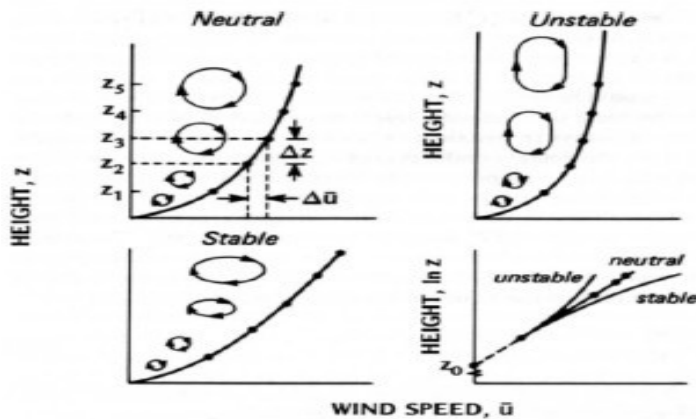


Figure 3.3 Wind profile modification due to stability (Thom, 1975).

3.5. Air pollution modelling

Air pollution models simulate the time evolution of spatial fields for a set of chemical species. There are many applications of the resulting numerical models, such as: understanding of physical processes as the assessment of the impact of a given process, environmental forecast, impact studies of emission sources, sensitivity analysis with respect to different scenarios of emission, inverse modelling (of uncertain emissions), etc. Different scales are concerned in the air pollution modelling: local scale (accidental release), regional scale (photochemistry urban pollution), continental scales (transboundary pollution with the example of acid rains), global scale (atmospheric chemistry in the stratosphere, oxidizing power of the troposphere, etc).

Figure 3.4 illustrates in general the scheme of processes described by a chemistry-transport model. Some primary substances such as: Nitrogen oxide or volatile organic compounds are come from both anthropogenic and biogenic sources. After that the chemical components diffused vertically in the atmospheric boundary layer due to turbulent eddies related to wind shear (mechanical forces) and buoyancy (thermal forces), while the horizontal movement is caused by wind advection. Chemical reactions of gases, related mainly to the oxidizing power of the atmosphere and to the radiative fluxes into photolysis operation, which cause the formation of secondary pollutants as ozone O_3 . Mass transfer between aqueous phase (cloud droplets), gas phase and particulate matter (solid or liquid particles in suspension) may also happen. Furthermore, the assessment of aerosols is governed by microphysical processes like the collision between particles (coagulation), formation of small clusters of gaseous molecules (nucleation), mass transfer between the semi-volatile species and particles (condensation/evaporation) or the formation of aerosols to cloud droplets through condensation of water vapor (activation). The dry deposition is the loss processes from the atmosphere which happened when gases or particles impinges upon and stick to the surface.

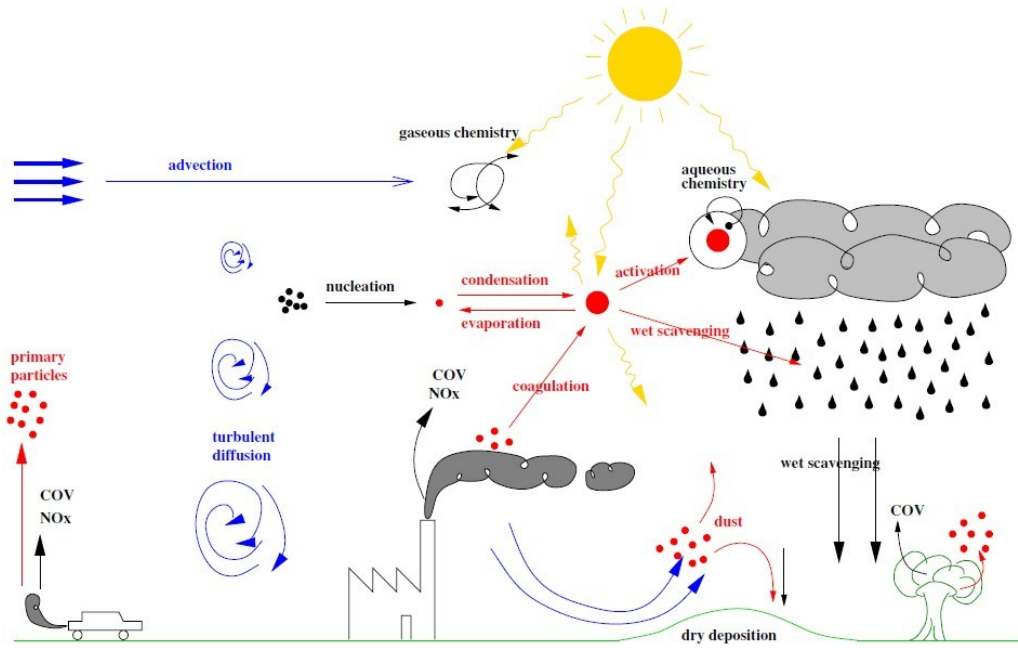


Figure 3.4 Scheme of processes described in a chemistry transport model (Sportisse, 2007).

3.6.3D atmospheric chemical transport models

The starting point of atmospheric chemical transport models is the mass balance equation for a chemical species i (equation 3.26):

$$\frac{\partial c_i}{\partial t} + \nabla \cdot (u c_i) = \nabla \cdot (K \nabla c_i) + E_i - S_i \quad (3.26)$$

$$\frac{\partial c_i}{\partial t} + u_x \frac{\partial c_i}{\partial x} + u_y \frac{\partial c_i}{\partial y} + u_z \frac{\partial c_i}{\partial z} = \frac{\partial}{\partial x} \left(K_{xx} \frac{\partial c_i}{\partial x} \right) + \frac{\partial}{\partial y} \left(K_{yy} \frac{\partial c_i}{\partial y} \right) + \frac{\partial}{\partial z} \left(K_{zz} \frac{\partial c_i}{\partial z} \right) + E_i(x, y, z, t) - S_i(x, y, z, t) \quad (3.27)$$

where $c_i(x, t)$ is the concentration of i as a function of location x and time t , $u(x, t)$ is the velocity vector (u_x, u_y, u_z) , $E_i(x, t)$ and $S_i(x, t)$ are the emission and removal fluxes, respectively. In the second equation (3.27), $u_x(x, y, z, t)$, $u_y(x, y, z, t)$, and $u_z(x, y, z, t)$ are the x , y , and z components of the wind velocity and $K_{xx}(x, y, z, t)$, $K_{yy}(x, y, z, t)$, and $K_{zz}(x, y, z, t)$ are the corresponding eddy diffusivities. The turbulent fluctuations u' and c'_i of the velocity and concentration fields relative to their mean values u and c_i have been approximated using the K theory (or mixing length or gradient transport theory) in (3.27) by:

$$\overline{u'c'_i} = -K \cdot \nabla c_i \quad (3.28)$$

According to J. H. Seinfeld and S. N. Pandis 2006, equation (3.28) is the simplest solution to the closure problem and is currently used in the majority of chemical transport models. Higher-order closure approximations have been developed but are computationally not cheap. Part of the latest formulations have shown promise of becoming computationally competitive with the commonly employed K theory.

3.6.1. Coordinate System—Uneven Terrain

Some studies assumed that the terrain is flat. Obviously, this is not always the case. For example, severe air pollution problems often occur in regions that some times bounded by mountains which block the movement of air. The surface of the Earth can be characterized by its topography;

$$Z = h(x, y) \quad (3.29)$$

in the modelling domain the upper boundary can be characterized by the mixing height $H_m(x, y, t)$ or an appropriately selected constant height H_t . The numerical solution of the atmospheric diffusion equation is relatively complicated because of the topography. Researchers usually transform the modelling domain to a simple geometry (Fig. 3.5), Instead of using the actual height of a site which is computed by taking the sea level as a reference. This can be finished by a mapping that converts points (x, y, z) to points (x, y, ζ) or from the physical domain to the computational domain. The terrain-following coordinate transformation is used, where:

$$\zeta = \frac{z - h(x, y)}{H_t - h(x, y)} = \frac{z - h(x, y)}{\Delta H(x, y, t)} \quad (3.30)$$

this formula rescales the vertical coordinate of the modelling domain into a new coordinate domain ζ which varies from 0 to 1. One may also simply subtract the surface height and define the new vertical coordinate by:

$$z' = z - h(x, y) \quad (3.31)$$

and now z' has units of length and is not bounded between 0 and 1.

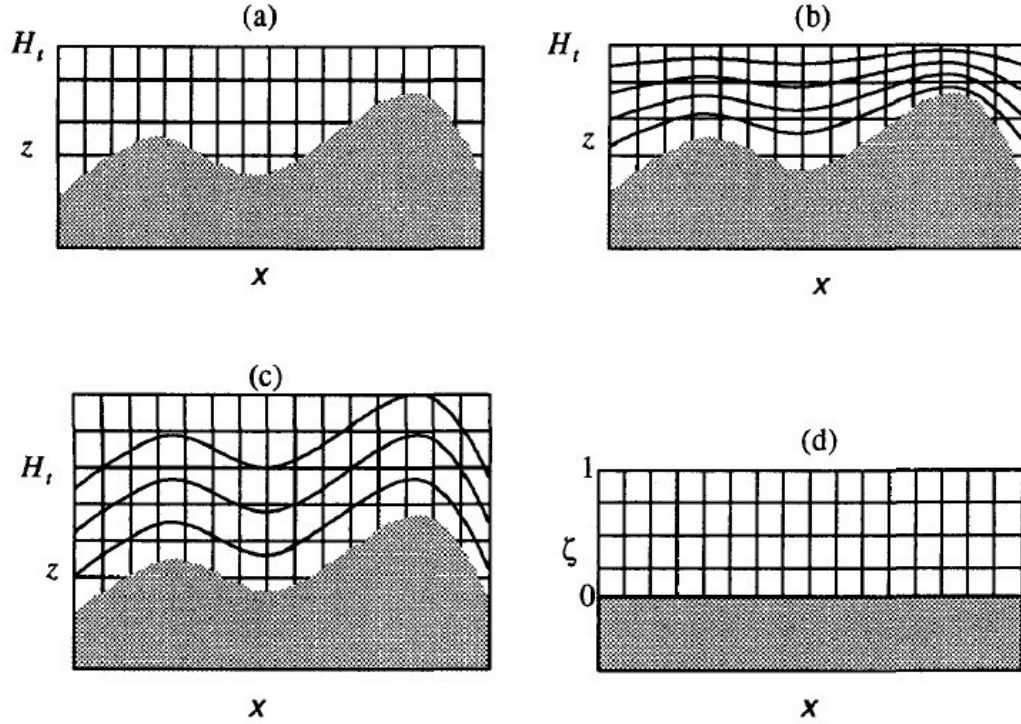


Figure 3.5 Coordinate transformation for uneven terrain: (a) two-dimensional terrain in $x - z$ space; (b) same as (a) but with contours of constant ζ superimposed; (c) same as (a) but with contours of constant z' superimposed; (d) two-dimensional terrain in $x - \zeta$ computational space (the terrain is indicated by the shaded region).

The above transformations result in changes of the components of the wind field from (u_x, u_y, u_z) to (u_x, u_y, ω) , where for the terrain-following coordinate system.

$$\omega = \frac{1}{\Delta H} \left[u_z - u_x \left(\frac{\partial h}{\partial x} + z \frac{\partial \Delta H}{\partial x} \right) - u_y \left(\frac{\partial h}{\partial y} + z \frac{\partial \Delta H}{\partial y} \right) - z \frac{\partial \Delta H}{\partial t} \right] \quad (3.32)$$

Note that, if the terrain is rough (large derivatives $\partial h/\partial x$ and $\partial h/\partial y$) imply that even if the original vertical wind speed u_z is small, the new wind speed ω can be important. For the simple coordinate system transformation of (3.31), the vertical velocity is:

$$\acute{\omega} = u_z - u_x \frac{\partial \Delta H}{\partial x} - u_y \frac{\partial \Delta H}{\partial y} \quad (3.33)$$

The coordinate transformations analysed previously result in changes of the eddy diffusivities. Initially, the eddy diffusivity tensor K was diagonal, but the transformed form is

no longer diagonal. Whatever, the off-diagonal terms participation to turbulent transport in widely flows in urban area is negligible. If the terrain-following coordinate system is used if these terms are neglected and, then:

$$K_{\zeta\zeta} = \frac{K_{zz}}{\Delta H^2} \quad (3.34)$$

For the simple transformation of (3.31), no modification is necessary. The required changes for the three coordinate systems are written in Table 3.3. It is noted that for the terrain-following systems boundary conditions must be applied at $\zeta = 0$ and $z' = 0$, where for the physical coordinate system boundary conditions application at $z = h(x,y)$ (Figure 3.5). When using the simple terrain-following coordinate transformation (3.31), is effectively "flattens out" the terrain, resulting the flat domain of modelling illustrates in Figure 3.5d.

Coordinate system	Coordinates	Definitions	Vertical wind speed	Vertical eddy diffusivity
Physical	x, y, z		u_z	K_{zz}
Terrain-following	x, y, ζ	$\zeta = \frac{z-h(x,y)}{\Delta H(x,y,t)}$	ω^a	$\frac{K_{zz}}{\Delta H^2}$
Simple terrain-following	x, y, z'	$z' = z - h(x,y)$	ω^b	K_{zz}

^aGiven by: equation 3.32

^bGiven by: equation 3.33

Table 3.3 Coordinate Systems for Solution of the Atmospheric Diffusion Equation

3.6.2. Initial conditions

The specification of the initial and input concentration field of all substances is required for the solution of the full atmospheric diffusion equation:

$$c_i(x,y,z,0) = c_i^*(x,y,z) \quad (3.35)$$

In a domain of simulation over the urban or global scales which formed by thousands of computational cells, it is necessary to define the concentrations of all the simulated substances and at all the points. In reality it is impossible to find a sufficient measurements exist, mainly in the upper part of the simulation domain, which leads to use the extrapolation from the few available data to the rest of the modelling domain. This can introduce an important error during the start of the simulation. After the run of the simulation, the effect of

the initial conditions will be lost and the solution is dominated by the emissions and the boundary conditions, even if the specified initial conditions contain gross errors. It is therefore useful to start the simulation of atmospheric phenomenon with a given period of time before. By the end of the initial period we have an established concentration fields that ofcourse do not reflect initial conditions and after we start a comparison with observation. The startup time for a chosen air quality model is determined by the residence time of an air parcel in the domain of modelling.

3.6.3. Boundary conditions

Except the global-scale models simulating the whole Earth's atmosphere. The boundary conditions in horizontal direction are required for the atmospheric diffusion equation in three dimensions, for the x , y , and z directions. Determining the concentrations at the horizontal boundaries of the modelling domain as a function of time is given by the following equations:

$$\begin{aligned}c(x, 0, z, t) &= c_{x0}(x, z, t) \\c(x, \Delta y, z, t) &= c_{xl}(x, z, t) \\c(0, y, z, t) &= c_{y0}(y, z, t) \\c(\Delta x, y, z, t) &= c_{yl}(y, z, t)\end{aligned}\tag{3.36}$$

During the simulation period and in opposite to initial conditions, boundary conditions, continue affecting the simulation predictions. Moreover, because the concentration of simulated species in the field are practically not known at the full points of the boundary of the modelling domain, that is affect the quality of the simulation results. A proposition to solve this problem is to use boundary conditions in relatively clean areas, where boundary conditions are mostly known and have a small effect on model simulation. If it is not possible to add all the sources of spaces inside the modelling domain, the sources effect has to be added to the boundary conditions implicitly. An other solution is to use a regional model to provide boundary conditions to and urban scale model. The curent technique is named nesting technique (a local scale model is nested inside a regional scale model).

About the boundary conditions at the upper and lower part. Usually, a total reflection condition at the upper boundary of the computational domain which is the top of the planetary boundary layer is chosen:

$$K_{zz} \left(\frac{\partial c}{\partial z} \right)_{z=H_i} = 0 \quad (3.37)$$

The boundary condition used at the Earth's surface accounts for surface sources and sinks of material:

$$\left(v_{d,i} c_i - K_{zz} \frac{\partial c_i}{\partial z} \right)_{z=0} = E_i \quad (3.38)$$

where $v_{d,i}$ is the deposition velocity and E_i is the ground-level emission rate of the species. The ground-level emissions can be involved even as part of the $z = 0$ boundary condition or directly in the differential equation as a source term in the ground-level cells.

CHAPTER 4

MODELLING METHODOLOGY

4.1. Introduction

As mentioned in the introduction chapter, the current doctorate thesis is divided into two main parts: the first one concerned, the local scale modelling and simulation of pollutants (O₃, NO₂) dispersion and concentration. A prognostic meteorological and air pollution model was used in combination with data, which were collected by in situ and remote monitoring stations, in order to assess the photochemical smog formation over a complex topography area and the effect of meteorology conditions on its formation.

In the second part of the doctorate project, the NO₂ tropospheric vertical column densities (VCDs) are simulated at different resolutions, with focus to high polluted regions. Satellite data were averaged and regridded on daily basis, onto common analysis grids with the same model resolutions. The same conditions applied into the satellite data production, are used as a mask of valid measurements that is applied also to model results to make the satellite and model datasets fully consistent. During this part the effect of high resolution on the model simulations was also investigated.

4.2 Local-scale simulation

In this work, an attempt is made in order to investigate the photochemical smog formation and the prevailing flow pattern over a heavily industrialized mountainous basin in NW Greece. Six lignite-fired power stations, are operated in the greater area resulted in large amount of PM, NO_x, SO₂, emissions in the atmosphere (Kaldelis et al., 2012). The study focuses on the dispersion of ozone produced by primary pollutants' emissions from PSs and on the contribution of these external sources to the O₃ concentrations measured in the most populated city of the area, Kozani. The city is located in a distance of about 12 km southerly to the most neighbouring PS. It is a complicated case in terms of source variety (i.e. coal-

fired power plants' operation, mining activities, urban sources), ground complexity, and meteorological conditions prevailing. The basin north of the city is governed by nocturnal stagnant conditions favouring ozone production and accumulation within the surface boundary layer during sunny days. Stack emissions may affect the city under specific meteorological conditions, which in combination with urban sources may cause air pollution episodes (Triantafyllou et al., 2002).

A coupled mesoscale prognostic meteorological and air pollution model is used, in combination with data, which were collected by a conventional ground Monitoring Station (MS) and a Differential Optical Absorption Spectroscopy (DOAS) system. A seven-day period in the summer of 2006 was selected for simulation and in particular, the 23–29 of June 2006. This period of the year was recorded as a period with high temperatures and elevated air pollutant concentrations in the city of Kozani. For the same period, experimental data from the MS and DOAS system have also been collected. The analysis of pollutants' concentrations and meteorological parameters reveals the most important factors of ozone production, such as: solar radiation, temperature, wind speed and topography. The methodological advance in the present work is the combined use of in situ and remote sensing measurements and the outputs of the model simulations.

4.2.1. Study area and dataset description

The region of interest is located in in high complex topography in north western Greece. In the region, four lignite combustion power stations (PS1, PS2, PS3, PS4) with stacks of 115 - 200 m in height are operated with different and variable PM, NO₂ and SO₂ emissions (Kaldelis et al.,2012). The power stations use raw lignite as fuel that is mined nearby, through open-pit mines. The power plants lie at about 650 m above sea level. In addition that, there are also different other types of pollution sources in this area related with urban and agricultural/burning biomass activities. Figure 4.1 shows the topography of the region with the power stations (PS).

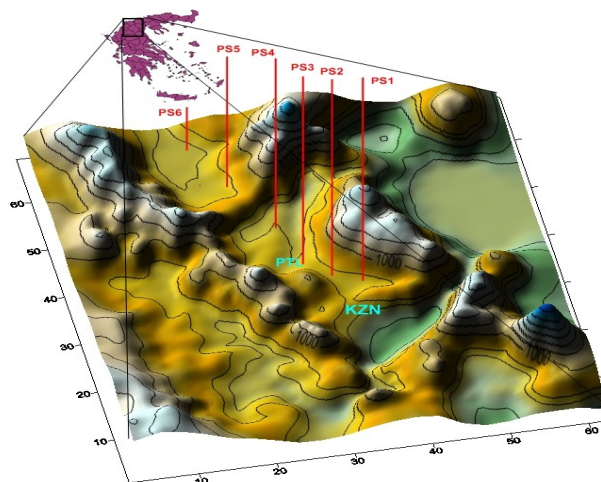


Figure 4.1 Topography of the area covered by the inner grid with the Power Stations (PS) (Triantafyllou et al, 2013)

The measured data were provided from both in situ measurement station and DOAS system in the city center of Kozani, the most populated city in the region. DOAS spectra were recorded using a high-pressure 150 W xenon lamp. The DOAS (SANO, Environment S.A.) system was installed on the roofs of two opposite buildings above the busiest street in the city of Kozani. Figure 4.2 describes the top of the street canyon covered by the DOAS light path. The emitter and the receptor were located at a height of 10 m and 15 m, respectively, above ground level covering a distance of 291 m in length. The span calibration of the DOAS system was performed by introduction of one or more-gas cell with a known high concentration of the gas in interest. More details for the matter can be found in Triantafyllou et al., 2008. Concentrations of O_3 , NO_2 , SO_2 , have been collected from DOAS measurements. For the same period, experimental data of SO_2 , O_3 and NO_2 from a ground measurement station located near the street canyon covered by DOAS light path, have also been collected. The sampling head was operating at a height of 3m AGL. Meteorological parameters of temperature, solar radiation, humidity, surface pressure and wind speed and direction were obtained from the meteorological station on the roof of the Technological Education Institution (TEI) of Western Macedonia, 1km outside the city of Kozani.

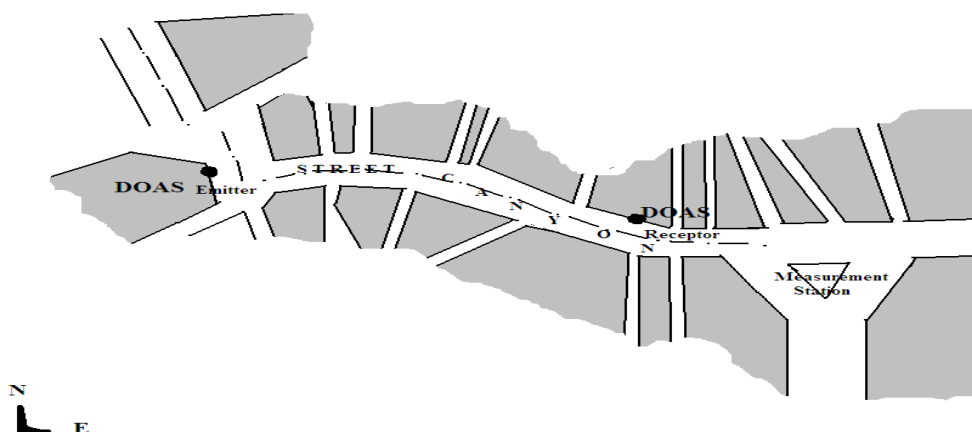


Figure 4.2 Street canyon covered by DOAS light path, and the measurement station location

4.2.2. Air pollution model

4.2.2.1. Model description

The Air Pollution Model (TAPM) is a PC-based, nestable, prognostic meteorological and air pollution model driven by a Graphical User Interface. TAPM solves fundamental fluid dynamics and scalar transport equations to predict meteorology and pollutant concentration for a range of pollutants important for air pollution applications. TAPM consists of coupled prognostic meteorological and air pollution concentration components, eliminating the need to have site-specific meteorological observations. Instead, the model predicts the flows important to local-scale air pollution, such as sea breezes and terrain-induced flows, against a background of larger-scale meteorology provided by synoptic analyses. For computational efficiency, it includes a nested approach for meteorology and air pollution, with the pollution grids optionally being able to be configured for a sub-region and/or at finer grid spacing than the meteorological grid, which allows a user to zoom-in to a local region of interest quite rapidly. The meteorological component of the model is nested within synoptic-scale analyses/forecasts that drive the model at the boundaries of the outer grid. The coupled approach taken in the model, whereby mean meteorological and turbulence fields are passed to the air pollution module every 5 min, allows pollution modelling to be done accurately during rapidly changing conditions such as in sea-breeze or frontal situations. The use of integrated plume rise, Lagrangian particle, building wake, and Eulerian grid modules, allows industrial plumes to be modelled accurately at fine resolution for long simulations. Similarly, the use of a condensed chemistry scheme also allows nitrogen dioxide, ozone, and particulates to be modelled for long periods. Details on the model approach with a more complete technical description can be found in (Hurley, 2005).

4.2.2.2. Model configuration

TAPM V4.0 was used in a nested mode with 25 x 25 x 25 grid points and 30-km, 10-km and 3-km spaced horizontal grids for meteorology, and with 81 x 81 x 25 grid points and 6-km, 2-km and 0.6-km, spaced horizontal grids for pollution. It is worth noting that the area covered by each pollution grid is less than the area of the corresponding meteorological grid. In this way, the pollution grids avoid the boundary regions of the nested meteorological grids, where unspecified vertical velocities can sometimes occur. The lowest ten model's levels were at heights of 10, 25, 50, 100, 150, 200, 250, 300, 400 and 500 m, with the model top at 8 km. TAPM was configured for the region of Kozani by extracting the surface information databases which are provided by CSIRO Atmospheric Research, Australia, and include gridded terrain height, vegetation and soil type, sea-surface temperature, and synoptic-scale meteorology (default databases was used).

The stacks of the PSs were employed as emission sources. A chemistry mode (PM10, NO_x, NO₂, O₃, SO₂, and PM2.5) was chosen to be simulated by the model. The concept of using Rsmog rather than Volatile Organic Compounds (VOCs) for all VOC emissions follows from the work of Johnson (1984). The concentration of Rsmog is defined as a reactivity coefficient multiplied by VOC concentration: [Rsmog] = 0.0067[VOC] (Hurley, 2005, TAPM Technical description, CSIRO,).

The model was run in Lagrangian mode to capture the near source dispersion more accurately during the first 900 seconds, and then changes to Eulerian mode, by using the TAPM option (Maximum particle travel time before conversion to EGM (LPM)), which allows selection of the travel time after which Lagrangian particles are converted to grid concentration and from then on represented by the Eulerian transport equation (EGM mode).

4.2.3. Data analysis

For the validation of the results obtained by the air pollution model TAPM, the ozone concentrations from model's first vertical level (9.3m) were compared with experimental data from a ground measurement station MS. Model validation was performed also by comparing model predicted values with the recorded data of Differential Optical Absorption Spectrometer (DOAS) that emits / receives along a street canyon in the city center.

The statistical evaluation method proposed by Wilmott (1985) is used to validate the model results, and to analyse pollutants' concentration against each other and meteorology parameters, in order to reveal the most important factors in ozone production. Hourly averages from monitored data were compared with hourly averages extracted from the

corresponding TAPM grid cells. Three performance indices were calculated, the Index of Agreement (*IOA*), the Root-Mean-Square-Error (*RMSE*) and the correlation coefficient *r*. The *IOA* is defined as

$$IOA = 1 - \frac{\sum_{i=1}^n (P_i - O_i)^2}{\sum_{i=1}^n (|P_i - O_{ave}| + |O_i - O_{ave}|)^2} \quad (4.1)$$

where, *n* is the number of observations, O_{ave} is the average of the observations O_i , and P_i are the simulation predictions. The index of agreement ranges from 0.0, noting complete disagreement, to 1.0, indicating perfect agreement between the observed and predicted observations. The *IOA* is a measure of skill of the model in predicting variations about the observed mean; a value above 0.5 is considered to be good.

The error in the model was assessed using the Root Mean Square Error *RMSE* (equation 4.2), as defined a Good model results assume that *RMSE* approaches to zero.

$$RMSE = \left[\frac{1}{n} \sum_{i=1}^n (O_i - P_i)^2 \right]^{1/2} \quad (4.2)$$

The correlation coefficient *r* (equation 3) is a measure of the extent to which two measurement variables “vary together”. The Correlation analysis tool is particularly useful when there are more than two measurement variables for each of *N* subjects.

$$r = \frac{N \left(\sum_{i=1}^N O_i P_i \right) - \left(\sum_{i=1}^N O_i \right) \left(\sum_{i=1}^N P_i \right)}{\sqrt{\left[N \left(\sum_{i=1}^N O_i^2 \right) - \left(\sum_{i=1}^N O_i \right)^2 \right]} \sqrt{\left[N \left(\sum_{i=1}^N P_i^2 \right) - \left(\sum_{i=1}^N P_i \right)^2 \right]}}, \quad (4.3)$$

The correlation coefficient is a number between -1 and 1, which measures the degree to which two variables, (e.g. measured and predicted values), are linearly related. Whether large values of one variable tend to be associated with large values of the other (positive correlation), whether small values of one variable tend to be associated with large values of

the other (negative correlation), or whether values of both variables tend to be unrelated (correlation near zero).

4.3. Meso-scale simulation

In the present study, NO₂ tropospheric vertical column densities (VCDs) are simulated at different resolutions. A two step approach is employed here to compare model results directly with satellite data. In the first step, best quality satellite retrievals are selected through specific conditions (cloud coverage, surface albedo and solar zenith angle) and built satellite data into the same model resolutions and regions. In the second step, the model simulation results are transformed using the averaging kernel interpolated to the model pressure levels.

The BOLCHEM model is employed to simulate NO₂ concentration, using different model resolutions. The OMI tropospheric NO₂ data (Dutch OMI NO₂, DOMINO v2.0) (Boersma et al., 2007) will be used for comparison. Model simulations were performed throughout 2007 (the last year of the 10 year CityZen experiment) over Europe and the two main hot-spots therein: the Po Valley and the BeNeLux area. In addition, the area of Gibraltar, is also considered since, in the absence of other important pollutant sources, shipping emissions have a major role (see figure 4.3). Analyses will be discussed on annual and seasonal bases and the effect of resolution will be also addressed.

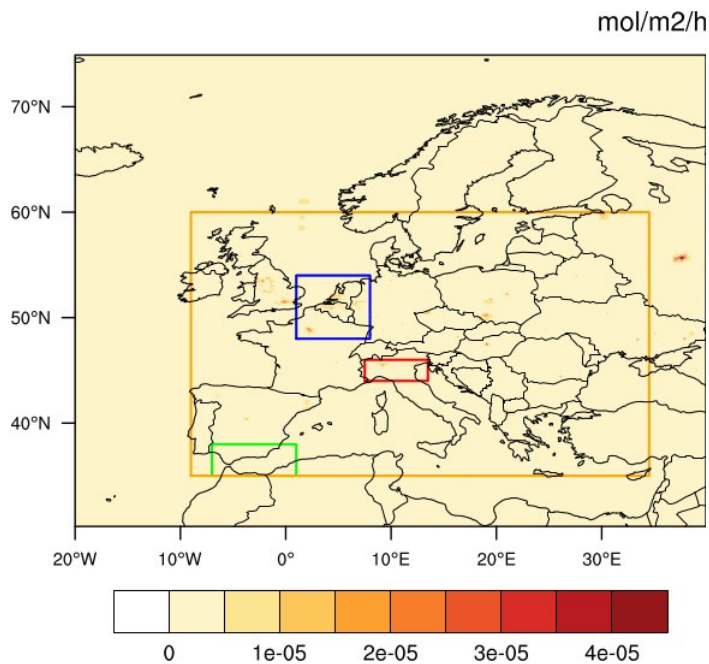


Figure 4.3 Selected regions for analysis: Europe (yellow), Po Valley (red), BeNeLux (blue) and Gibraltar (green), overlapped to average NO₂ emission rates sample (unit: mol/m²/h)

4.3.1. Model description

The BOLCHEM model (Mircea et al. 2008; Maurizi et al. 2010) is an on-line coupled meteorology-composition model. Its meteorological component is the mesoscale meteorological Bologna Limited Area Model (BOLAM), whose dynamics is based on hydrostatic primitive equations. The vertical grid uses a hybrid-terrain-following coordinate system, with variables distributed on a non-uniformly spaced staggered Lorenz (1960) grid. The horizontal discretisation uses geographical coordinates on an Arakawa C-grid. The time scheme is split-explicit, forward-backward for gravity modes. The weighted average flux (Billet and Toro 1997) advection scheme is implemented. Lateral boundary conditions are imposed using a relaxation scheme in order to minimise the wave energy reflection. As initial and lateral boundary conditions, use can be made of the data from the European Centre for Medium-range Weather Forecasts (ECMWF) or the global forecast system (NOAA-GFS). Hybrid model level data are directly interpolated on the BOLAM grid. Transport (advection and diffusion) of tracers (both passive and reactive) is performed on-line at each meteorological time-step using the mass-conservative WAF scheme (Maurizi et al. 2013) for advection and a “physical” (second-order) horizontal-diffusion, with diffusion coefficient carefully estimated from experiments (Tampieri and Maurizi 2007) to account for unresolved motion. Vertical diffusion is performed using a one-dimensional diffusion equation with a diffusion coefficient estimated by means of an E-I turbulence closure scheme (Zampieri et al. 2005). Dry deposition is computed through a resistance-analogy scheme and is provided as boundary condition to the vertical diffusion equation. Furthermore, vertical redistribution of tracers due to moist convection is parameterised consistently with the Kain-Frisch scheme used in the meteorological component for moist convection. Transport of chemical species is performed in mass units, while gas chemistry is computed as mixing ratio. Physical/chemical processes are treated separately for gas phase, aerosol classes and generic tracers (e.g. radioactive species, Saharan dust, etc.). The gas phase is treated using the SAPRC90 mechanism modified to account for secondary organic aerosol precursors. The Aerosol component is modelled using AERO3. The model is included in the COST 728/732 model inventory(<http://www.mi.uni-hamburg.de/List-classification-detail-view.6156.0.html?&nocache=1&mvid=2621441>), where more technical details can be found.

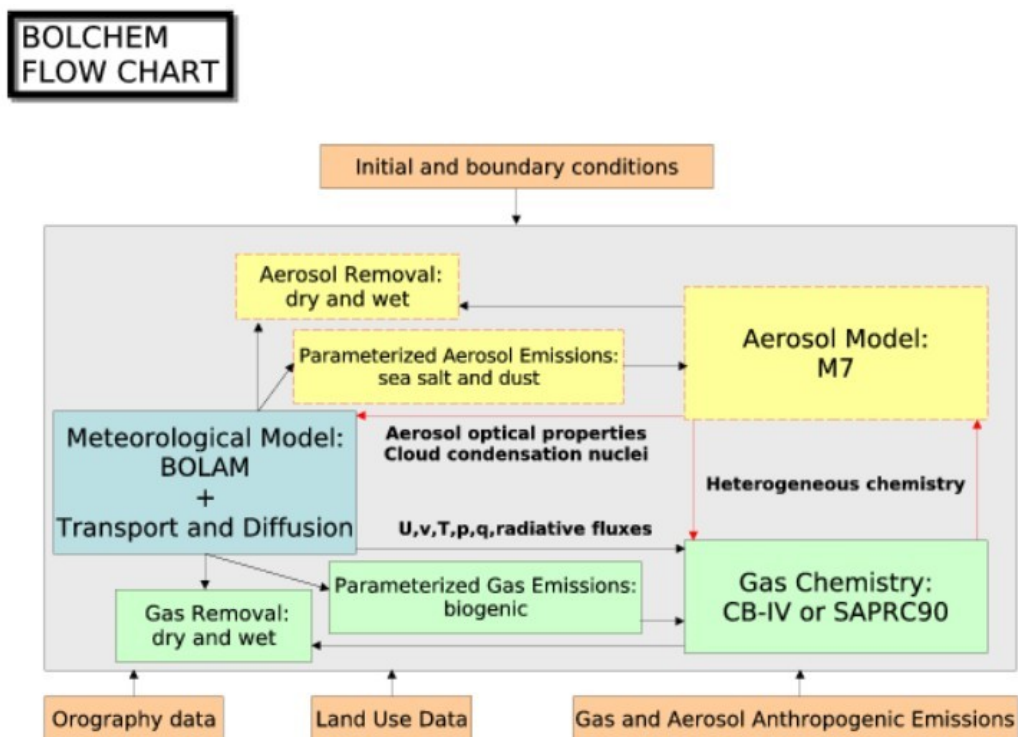


Figure 4.4 BOLCHEM flow chart (<http://bolchem.isac.cnr.it/projects/bolchem.do>)

BOLCHEM started as an online coupled meteorology and composition model (Baklanov et al. 2014) in 2003 (Butenschoen et al. 2003), when this approach was relatively new. It was successfully used in the GEMS Project for operational forecasts of gas-phase pollutants as a member of the GEMS-RAQ ensemble, for over 1.5 years. In the same framework, it was compared indirectly, as part of the GEMS-RAQ ensemble, to satellite-retrieved NO₂ VCD (Huijnen et al. 2010) and, directly, with IASI tropospheric O₃ columns (Zyryanov et al. 2012). Moreover, an upgraded version (2.0) was also verified in a 10-year experiment against surface data measurements as part of “megaCITY-Zoom for the Environment” (CITYZEN) project (Colette et al. 2011), showing good skills particularly for NO₂ surface concentration. To date, a systematic comparison with satellite NO₂ VCD over a long period with the focus on model performances has never been carried out and is part of the subject of the present work.

4.3.2. Experimental set-up

Model runs were performed over Europe with a horizontal resolution of 50×50 km², and in the two hot-spots (Po Valley and BeNeLux, as defined for the CITYZEN project) at 10×10 km², with 40 and 20 vertical sigma-hybrid levels for meteorology and chemistry, respectively. The top of chemistry domain is approximately at 500 hPa. Equations are

integrated on a rotated-pole coordinate system with a time-step of 400 s. Boundary conditions for the meteorology were supplied by ECMWF; for tracers, gas and aerosols, climatological boundary conditions were used for the European domain. For the two hot-spots, the boundary conditions were taken from the simulation of the European domain every hour. Emissions prepared for the CITYZEN project by INERIS (<http://www.ineris.fr>) (Colette et al. 2011) were used. This emission dataset was prepared for the 10-year experiment using on official European Monitoring and Evaluation Programme (EMEP) data (with resolution of $50 \times 50 \text{ km}^2$) and spatial distribution based on the GEMS-RAQ emissions (at $10 \times 10 \text{ km}^2$ resolution). This emission dataset is affected by the typical uncertainty of similar datasets like, e.g. the one prepared with the same spatial resolution in the frame of the “Monitoring Atmospheric Composition and Climate (MACC)”.

4.3.3. Satellite data (OMI sensor)

The ozone monitoring instrument (OMI) flies on the NASA/EOS-AURA satellite, providing the possibility of global measurements of the atmospheric NO₂ VCDs via measuring direct and backscattered sunlight in the Ultraviolet-Visible range from 270 nm to 500 nm (Levelt et al., 2006). The instrument was launched in July 2004 with a Sun-synchronous polar orbit crossing the equator at 13:30 local time. The OMI satellite observes the atmosphere with a spatial resolution of 13 km along track and 24 km across track in the nadir view, with a global coverage in one day.

The OMI tropospheric NO₂ level-2 data (Dutch OMI NO₂, DOMINO v2.0) used in this study for Europe in 2007 are obtained from Tropospheric Emission Monitoring Internet Service (TEMIS) project (<http://www.temis.nl>). According to Boersma et al. (2007) and Boersma et al. (2011), the NO₂ DOMINO retrieval algorithm is based on three main steps: (i) obtain the NO₂ slant column density from OMI reflectance spectra, using differential optical absorption spectroscopy (DOAS); (ii) estimate and separate the stratospheric and tropospheric contributions to the slant column; and (iii) convert the remaining tropospheric slant column using the tropospheric air mass factor (AMF). Moreover, only satellite measurements with cloud fractions less than 50% are included in the satellite dataset (van der A et al. 2008). The DOMINO level-2 data contains geolocated column integrated NO₂ concentrations, or NO₂ columns (in units of molecules/cm²). DOMINO data constitute a pure Level-2 product, i.e. it provides geophysical information for each and every ground pixel observed by the instrument, without the additional binning, averaging or gridding typically applied for Level-3 data. In addition to vertical NO₂ columns, the product contains

intermediate results, such as the result of the spectral fit, fitting diagnostics, assimilated stratospheric NO₂ columns, the averaging kernel, cloud information, etc.

According to Boersma et al. 2011, improvements for DOMINO v2.0 were found in the calculation of the air mass factors (AMFs), through improved radiative transfer modelling, the use of high-resolution data on terrain height and surface albedo, and better a priori NO₂ profiles (improving the sampling of the TM4 model). Over large polluted areas, version 2.0 tropospheric NO₂ columns are generally reduced by 10–20% relative to previous versions. Locally, differences between v2.0 and v1.02 retrievals may be stronger as a result of the higher resolution terrain height and albedo maps, and de-stripping corrections (Boersma et al., 2011). Further information on the DOMINO v2.0 retrieval algorithm is available in Boersma et al. (2011) and the latest updates can be found in the DOMINO product specification document ([http://www.temis.nl/docs/OMI NO2 HE5 2.0 2011.pdf](http://www.temis.nl/docs/OMI_NO2_HE5_2.0_2011.pdf)).

4.3.4. Satellite tropospheric NO₂ VCD level-3 production

In order to compare the modelled tropospheric columns to satellite retrieval products correctly. The OMI daily data level-2 Hierarchical Data Format (HDF) files, without binning, averaging and gridding are used. The satellite level-2 swath files were regridded on daily basis using the WHIPS (<http://www.sage.wisc.edu/download/WHIPS/WHIPS.html>) tool, onto common analysis grids with the same model resolution: 50 × 50 km² in the Europe and Gibraltar cases and 10 × 10 km² for the Po Valley and BeNeLux. In the regridding procedure, data with cloud cover larger than 0.2, surface albedo larger than 0.3 and solar zenith angle larger than 85° are discarded. This filter produces a mask of valid measurements that is applied also to model results to make the satellite and model datasets fully consistent. Figure 4.5 shows the difference between satellite grid and fixed regular grid.

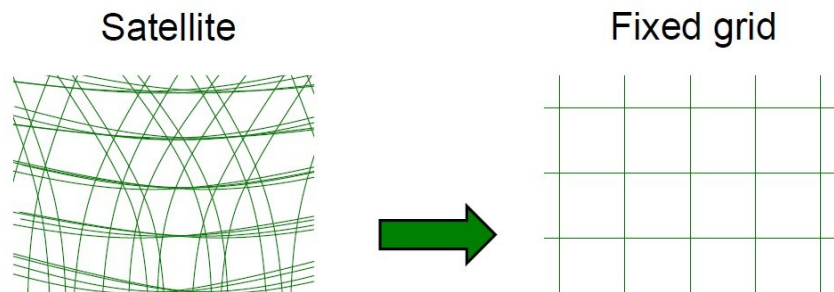


Figure 4.5 Difference between satellite grid and fixed regular grid

4.3.5. Computation of tropospheric NO₂ VCD

As indicated in the user manual of OMI satellite data product for advanced users interested to model-OMI comparison, all the comparisons between model and satellite products should be done by taking into account the OMI averaging kernel, that provides the link between (modelled) reality and retrieval data. More specifically the averaging kernel matrix AK is the sensitivity of the retrieved state to the true atmospheric state for each vertical level in the retrieval grid.

According to above, and after averaging and regridding the satellite level-2 swath data on daily basis using WHIPS software, to a common analyses grid for each model resolution and for all regions. The tropospheric NO₂ averaging kernel (AK) is extracted from each satellite daily file level-3 and interpolated from the TM4 (the chemistry transport model used in the satellite data retrieval procedures) model pressure levels to BOLCHEM model pressure levels.

First the tropospheric NO₂ averaging kernel for the TM4 model is calculated through the following formula:

$$AK_{tm4_{trop}} = AK_{tm4} * \left(\frac{AMF}{AMF_{trop}} \right) \quad (4.4)$$

where AK_{tm4} is the total column averaging kernel and AMF and AMF_{trop} are the air mass factors for the total columns and tropospheric columns, respectively.

Then the interpolation procedure for every two vertical grid points $i1$ and $i2$ is done, in order to compute the tropospheric NO₂ averaging kernel Ak_{trop} interpolated to BOLCHEM model pressure layers for each grid point (i, j, k) , the interpolation is based on the tropospheric NO₂ averaging kernel ($AK_{tm4_{trop}}$) extracted from the satellite data.

Because model simulation reach a height of about 500 hPa, the upper NO₂ content was extrapolated linearly from the upper model value to zero at the tropopause (where O₃ exceeds 150 ppb which, above Europe, corresponds to about 200 hPa) (Huijnen et al. 2010). The linear extrapolation to zero is well-supported by the climatological fields used in CITYZEN (Colette et al. 2011) and the analysis about the application of the AK found in Huijnen et al. (2010). The tropospheric NO₂ concentration (molecules / m³) is extrapolated at every grid point (i, j, k) in the tropospheric upper part using the sigma coordinate system of the meteorology model (BOLAM).

The tropospheric averaging kernels is then applied to the tropospheric vertical profiles of NO₂ simulated by BOLCHEM model using the following equation:

$$Y_{trop} = AK_{trop} * X_{trop} \quad (4.5)$$

Where Y_{trop} is the transformed model profile and X_{trop} is the tropospheric NO₂ profile simulated by BOLCHEM model.

Since we have the NO₂ tropospheric concentrations simulated and sampled at the same satellite overpass time over Europe (13:30 UTC) in addition to the tropospheric NO₂ AK interpolated to BOLCHEM model pressure layers, the tropospheric NO₂ VCD can be computed by multiplying the model simulations with the interpolated AK_{trop} . Then the produced gaseous profiles were integrated from the surface up to the maximum of the troposphere layer (z_{top}) and for the time period from 01/01/2007 to 31/12/2007, as described in equation (4.6):

$$NO2_{TVCD} = \int_0^{z_{top}} AK_{trop_i} c_i dz \approx \sum_{i=1}^{i=z_{top}} AK_{trop_i} c_i \Delta z_i \quad (4.6)$$

Where AK_{trop_i} is the NO₂ tropospheric averaging kernel, c_i is the NO₂ concentration in molecules/cm³ and Δz the model vertical step.

4.3.6. Statistical metrics

Three statistical metrics namely: correlation coefficient (r), root mean square error ($RMSE$) and mean bias (MB) are used to assess the model performance. This metrics have been successfully used in several studies for evaluating the performance of regional air quality models (e.g. Han et al. 2011 and Zyrichidou et al. 2013). The mean bias provides the information on the overestimation/underestimation of any variable by the model and is defined as:

$$MB = \frac{1}{N} \sum_{i=1}^N (P_i - O_i) \quad (4.7)$$

where the summation are performed over the total number of model-observations pair values (N) while O_i and P_i represent the i^{th} observed and simulation predicted values respectively. The two other metrics, correlation coefficient and $RMSE$ are already defined in a previous section (equations: 4.2 and 4.3). The $RMSE$ considers error compensation due to opposite sign differences. Although $RMSE$ encapsulates the average error produced by the model but it does not illuminate the sources or the types of errors.

4.3.7. Data processing

Starting from the daily values of both: modelled and satellite retrieved NO_2 tropospheric VCD, spatial and temporal averaged quantities are computed according to the selected regions and the temporal intervals chose for the evaluation (monthly, seasonal and annual). The NO_2 VCD netCDF (Network Common Data Form) files resulted from the model simulations and computed from the satellite measurements, are processed using the Climate Data Operators (CDO) software, which is a collection of many operators for standard processing of climate and model output. The operators include simple statistical and arithmetic functions, data selection and sub-sampling tools, and spatial interpolation.

The statistical value of the temporal ensemble mean of NO_2 VCD over a selected time interval n is given by the following formula:

$$\langle NO_{2_{TVCD}}(i, j) \rangle = \frac{1}{n} \sum_{t=1}^{t=n} NO_{2_{TVCD}}(i, j, t) \quad (4.8)$$

with $NO_{2_{TVCD}}(i, j, t)$ presents the tropospheric NO_2 VCD (molecules/m²) at a given grid point (i, j) and at the time t , n is the number of the selected time steps (month, season or year).

The statistical value of the spatial ensemble mean of NO_2 VCD over a selected region (x_1, x_2, y_1, y_2) and for an averaged time is computed as follow:

$$\overline{\langle NO_{2_{TVCD}} \rangle} = \frac{1}{N} \iint_{x_1, y_1}^{x_2, y_2} \langle NO_{2_{TVCD}}(i, j) \rangle dx dy = \frac{1}{N} \sum_{i=1, j=1}^{i=N, j=N} \langle NO_{2_{TVCD}}(i, j) \rangle \quad (4.9)$$

Where, $\langle NO_{2_{TVCD}}(i, j) \rangle$ is the tropospheric NO_2 VCD (molecules/m²) in every grid point (i, j) in the selected domain and for an averaged time, N is the number of grid points in the selected field.

CHAPTER 5

RESULTS AND ANALYSES

5.1. Introduction

Photochemical air pollution modelling and simulation in different atmospheric scales were realised during this study. In the first phase, the photochemical smog formation over a heavily industrialized area with complex terrain was investigated. Three-dimensional photochemical simulations have been performed by The Air Pollution Model (TAPM) for a seven-day period in the summer of 2006. A model configuration including the industrial sources has been built to simulate the pollutants dispersion and transformation around a complex topography region. Results from the numerical simulation were compared with observations of both in situ monitoring station and DOAS, which have been installed in the same area.

In the second part, NO₂ tropospheric vertical column densities (VCDs) are modelled and simulated at different resolutions using the online-coupled BOLCHEM model. In order to compare the same number of pairs of observation-simulation collocated in space and time. The best quality satellite retrievals are selected and level-3 product are built into the same model resolutions and regions. From the other hand, the model simulation results are transformed using the interpolated NO₂ tropospheric averaging kernel. Model output is compared to OMI satellite data from TEMIS for the year 2007. High-polluted areas are simulated at finer resolution and analysed separately.

5.2. Photochemical air pollution modelling in local-scale

5.2.1. Meteorology

The distribution of pollutants and therefore the ozone production depends on meteorological conditions such as temperature, solar radiation, wind speed and its direction. To validate the simulated meteorological fields, we compare the model results to

experimentally measured parameters like temperature, solar radiation and wind speed and direction (Figure 5.1a,b,c,d). They were obtained from the meteorological station on the roof of the Technological Education Institute (TEI) of Western Macedonia located in the region of interest. Performance statistics between TAPM meteorology results and the corresponding observed values in the meteorological station are presented in Table 5.1.

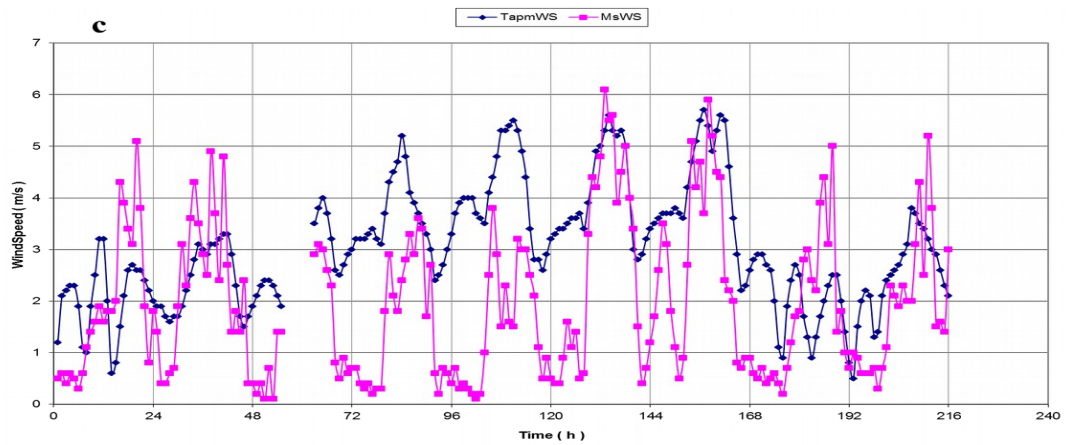
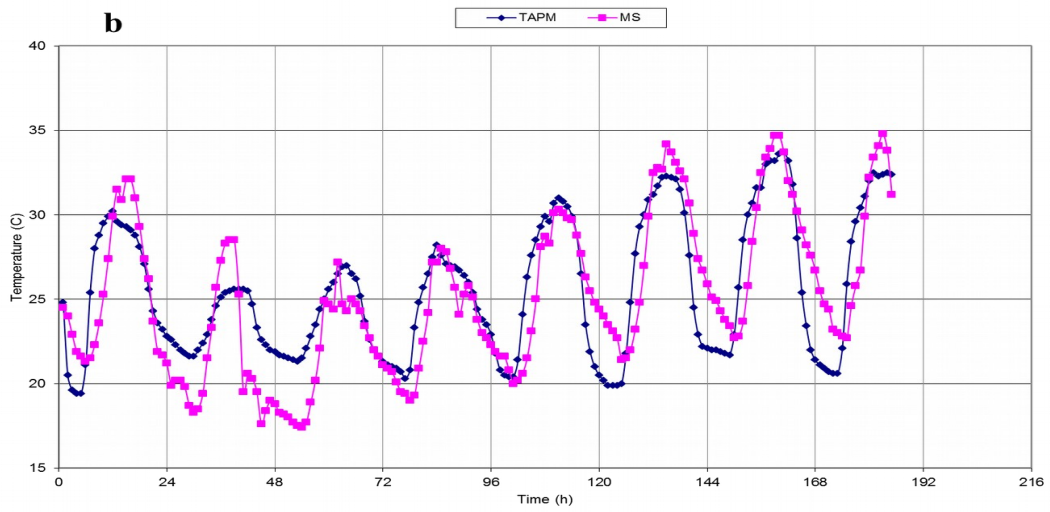
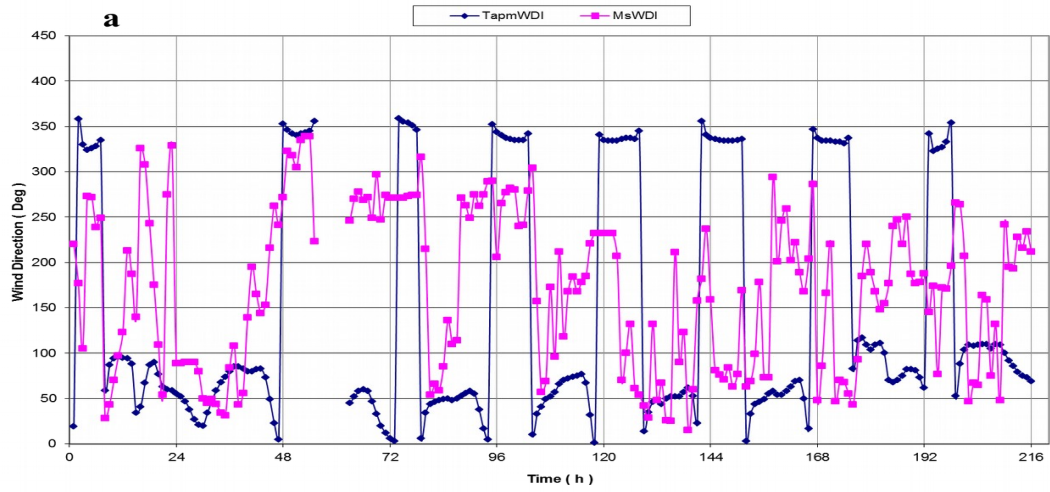
The first graph in Figure 5.1 demonstrates that shifts in wind direction occur at the right times at city, which means; wind reversal starts and stops at the same time. The discrepancy in wind direction at the beginning and the end of each shift is mainly attributed to the proximal approximation of the grid point that nearly represents the station location, and the complex topography of the area.

Temperature shows reasonable agreement for the minimum and maximum respectively at 04:00 and 15:00, during the simulation period (Figure 5.1 second graph). A slight discrepancy at minimal and maximal values may be attributed to the difficulties in accurately modelling of the lower layer and humidity content of soil (deep soil parameters). Regarding the wind speed (Figure 5.1 third graph) the difference in values is due to the location of the meteorological station and the complex topography of the area of interest. However, there is an acceptable correlation ($r = 0.46$) between the observed and modelled values. The fourth graph gives a good comparison for the solar radiation during the period of the simulation, with a very good agreement (IOA = 0.88) and a high correlation coefficient $r = 0.79$.

Finally, we can say that the simulated meteorological fields are realistic. Temperature has shown significant agreement with the experimental data. Wind speed and direction are reproduced with wind reversal observed at the same times in the model and in measurements. Solar radiation is evaluated very well with MS data. Therefore, meteorological fields are viewed as realistic enough to drive transport and mixing of chemical species.

	IOA	RMSE	Correlation Coefficient (r)
Temperature (C)	0.89	2.63	0.81
Solar Radiation (W/m ²)	0.88	200.1	0.79
Wind Speed (m/s)	0.62	1.88	0.46

Table 5.1 Model performance statistics for meteorology



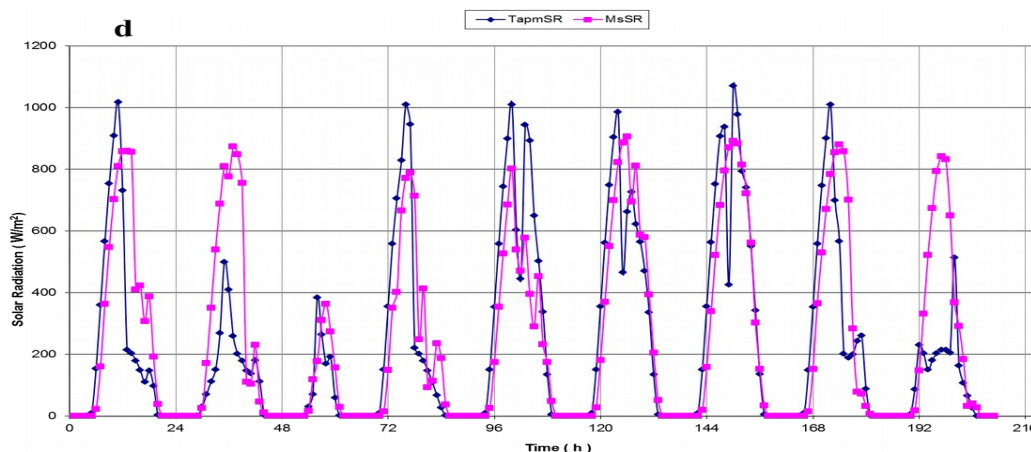


Figure 5.1 Meteorological monitoring station MS compared to TAPM results for: a) Wind direction, b) Temperature, c) Wind speed and d) Solar radiation (SR).

5.2.2. Model's results and validation of chemistry

The ozone concentrations from the model's first vertical level (9.3m) were compared with observations from both in situ MS and DOAS system. Figure 5.2 shows the observed mean hourly O_3 concentrations in Kozani city centre (MS and DOAS system) and the corresponding predicted values by the model during the simulated period (23-29, June 2006). Temporal variability of the simulated ozone concentrations correspond reasonably well to the measured values from DOAS and MS. The higher concentrations are also observed at about the same time (16:00) in both, the simulation and the observations. Table 5.2 reports the statistical evaluation results of the ozone data obtained by the simulation against both; measurement station and DOAS data during the simulated week. The index of agreement and the correlation coefficient for TAPM simulation are 0.70 and 0.60 respectively with the MS data; this shows relatively high skill of TAPM to describe the situation. The corresponding values against DOAS are 0.41 and 0.63 respectively.

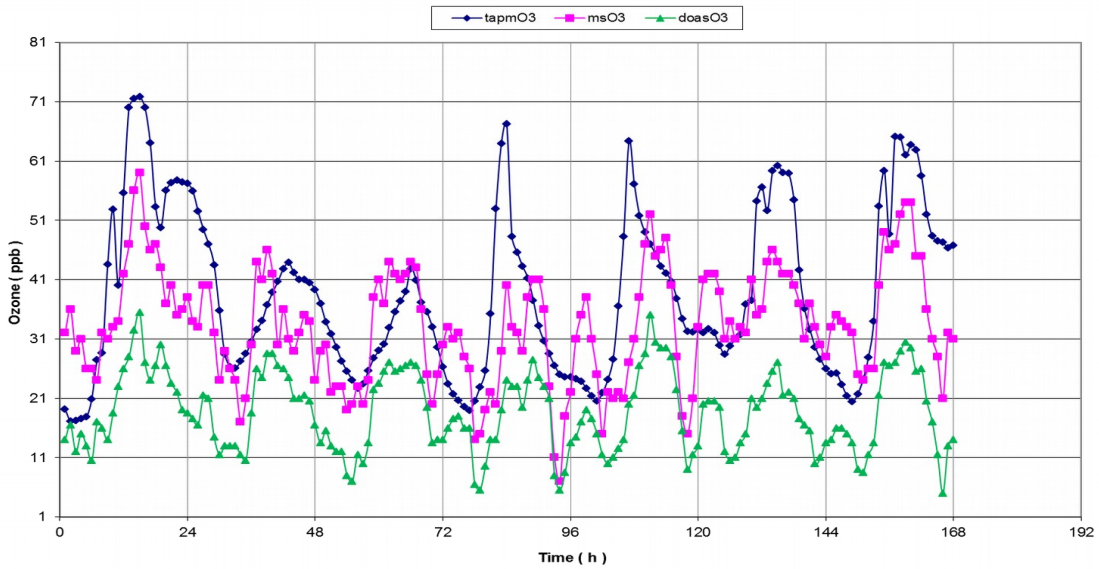


Figure 5.2 Observed and predicted mean hourly Ozone concentrations (ppb), obtained by TAPM, Measurement station and DOAS, during the simulated period; 23-29 June 2006

The difference between the concentrations of in situ measurement station, DOAS and the TAPM predictions may be because of the level and the area in which every tool took the information. So, the DOAS system’s measurements represent averages over paths, while the MS gives the concentration values at a specific point which is not exactly below the DOAS path and TAPM grid point. It is also mentioned that in meteorology at the model top boundary, all variables are set at their synoptic values. This is different from pollution case where no boundary conditions are used, which may affect the simulation results. In addition it is noted that during the extraction of the model results from the grid points above measurements location (neighbouring points), the nearest grid point to the station and DOAS bath was taken. It also must be taken into account that O₃ background concentrations of 20 ppb were used as input in the model, which explains the drift of the model’s results.

	IOA	RMSE (ppb)	Correlation Coefficient (<i>r</i>)
Monitoring Station	0.70	12.40	0.60
DOAS	0.41	22.76	0.63

Table 5.2 Model performance statistics of mean hourly Ozone concentrations during the considered period

Table 5.3 shows all the statistical measures of the hourly averages during the simulated period. The correlation coefficient of the hourly averages for the whole week

between the observed and predicted ozone data is significantly high, 0.75 and 0.86 with MS and DOAS, respectively. Results from Model for ozone are in good agreement with the ground surface station and DOAS data. Figure 5.3 shows the scatter-plots between the measured and predicted ozone concentrations in Kozani city for the whole period. All the DOAS data is under the line 1:1, while monitoring station (MS) data is above the line 1:1 for the small values and under it for the highest values, with slopes equal to 0.44 and 0.77 for DOAS and MS respectively.

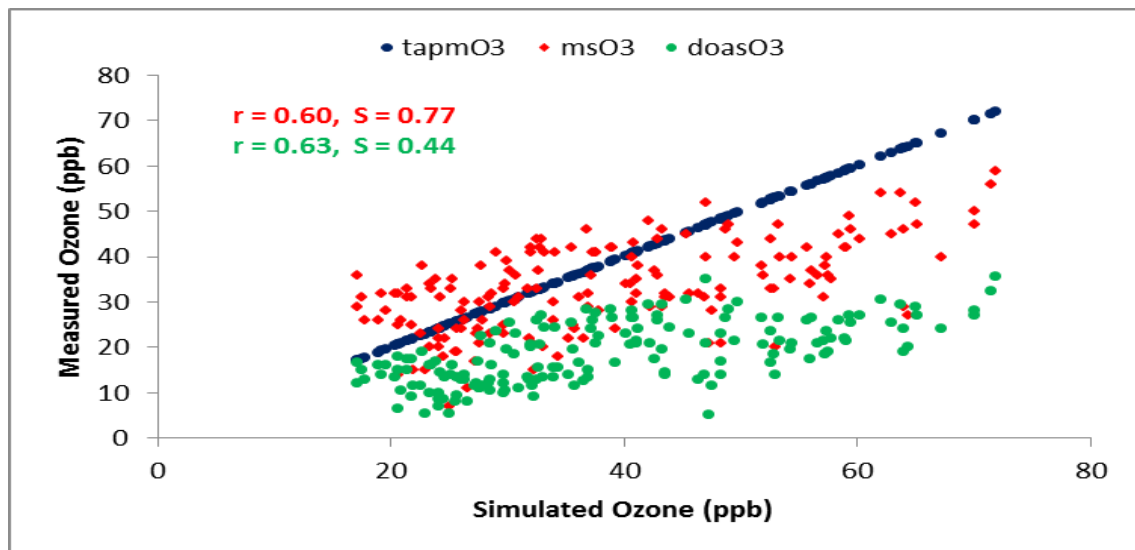


Figure 5.3 Comparison between measured and simulated Ozone, where (r) is the correlation coefficient and (S) is the slope.

	IOA	RMSE (ppb)	Correlation Coefficient (r)
Monitoring Station	0.78	8.13	0.75
DOAS	0.42	20.6	0.86

Table 5.3 Model performance statistics of ozone's daily variation computed from the hourly averages values of the whole period

In NO_2 case (Figure 5.4), the results obtained by TAPM are not compared well with surface data. There is also a difference between the data from the two measuring station (DOAS and MS). This is attributed to the different traffic loads at the areas of sampling. The MS location is very close to vehicular sources emitting considerable amounts of NO_x ($\text{NO} + \text{NO}_2$). That is why its values are very high against DOAS values which are acquired from high level (10 to 15m) and indicate averages over the path above the street canyon. On the other hand, TAPM results represent a grid point at 10 m higher than the ground. Besides, the

location of the ground sampling station is not exactly below the DOAS path and TAPM grid point.

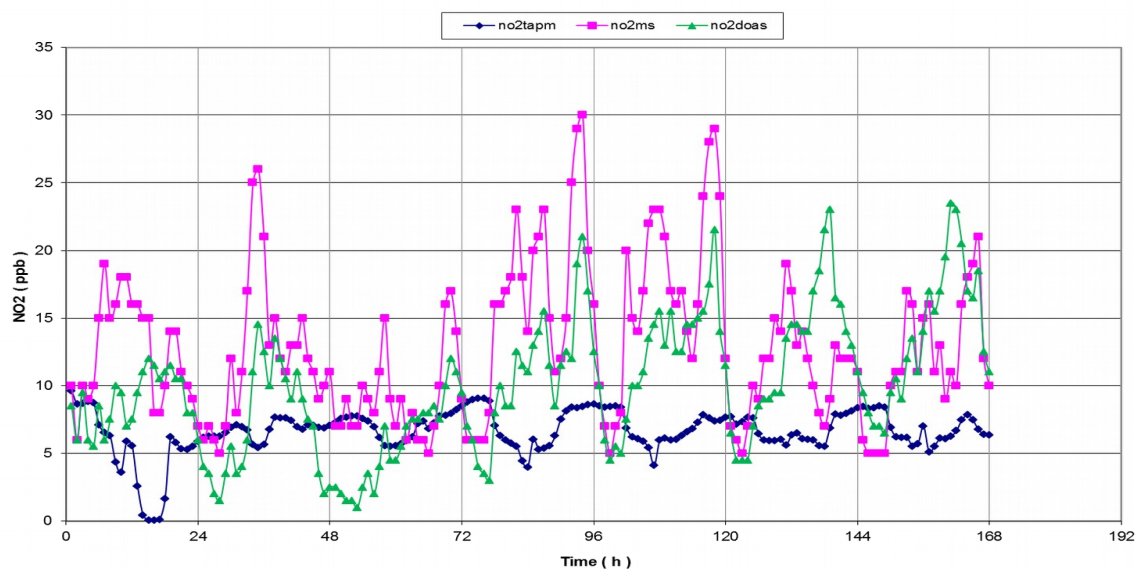


Figure 5.4 Concentrations of NO₂, obtained by TAPM, Measurement station and DOAS, during the simulated period between 23 and 29 June 2006.

5.2.3. Effect of meteorology on O₃, NO₂ formation

Figures 5.5.a,b,c and table 5.4 show the effect of the meteorology conditions (temperature, solar radiation and wind speed) on the formation of ozone and NO₂ during the simulated period. Figure 5.5.a and b display that high ozone concentrations coincide with high temperature and solar radiation, and low NO₂ concentrations, which explains the photochemical operation between primary pollutants and sunlight, resulting in ozone production. This symmetric level has occurred between ozone and NO₂ which follow opposite trends with a correlation coefficient of -0.70. It is worthwhile to be mentioned here that Triantafyllou et al., 2008, have found the correlation coefficient between O₃ and NO₂ equal to -0.59 by using one year's concentration measurements of the MS.

A steady rise in ozone level is observed with decreased NO₂ concentration. The peak concentration of NO₂ occurs before the peak of ozone, because the photochemical reaction sequence forms NO₂ first and then ozone. The above hints show the favourable photochemical ozone production within the urban complexity between the morning hours up to the afternoon. The figure 5.5.c illustrates the relation between O₃, NO₂ and wind speed. As shown in this graph, when the horizontal wind speed increases, ozone concentration increases too, as fresh oxygen is supplied in the photochemical cycle reacting with NO₂ and finally

leading to the production of O₃. In addition, wind contributes to the dilution of the atmospheric mass bringing these more photochemically reactive molecules under the sunlight's influence.

Correlation Coefficient (<i>r</i>)	Ozone	NO ₂
Temperature	0.71	- 0.53
Solar Radiation	0.46	- 0.46
Wind Speed	0.29	0.004
NO ₂	- 0.70	1

Table 5.4 The correlation coefficient (*r*) of chemical and meteorological TAPM results

Table 5.4 presents the correlation coefficient between ozone, NO₂, temperature and solar radiation. A good correlation between ozone and meteorology was found, specifically the correlation coefficient found is equal to 0.71 and 0.46 for temperature and solar radiation respectively. Negative correlation between NO₂ and meteorology parameters, with -0.53 against temperature and -0.46 against solar radiation were found. These findings confirm the factors that drive the photochemical phenomena.

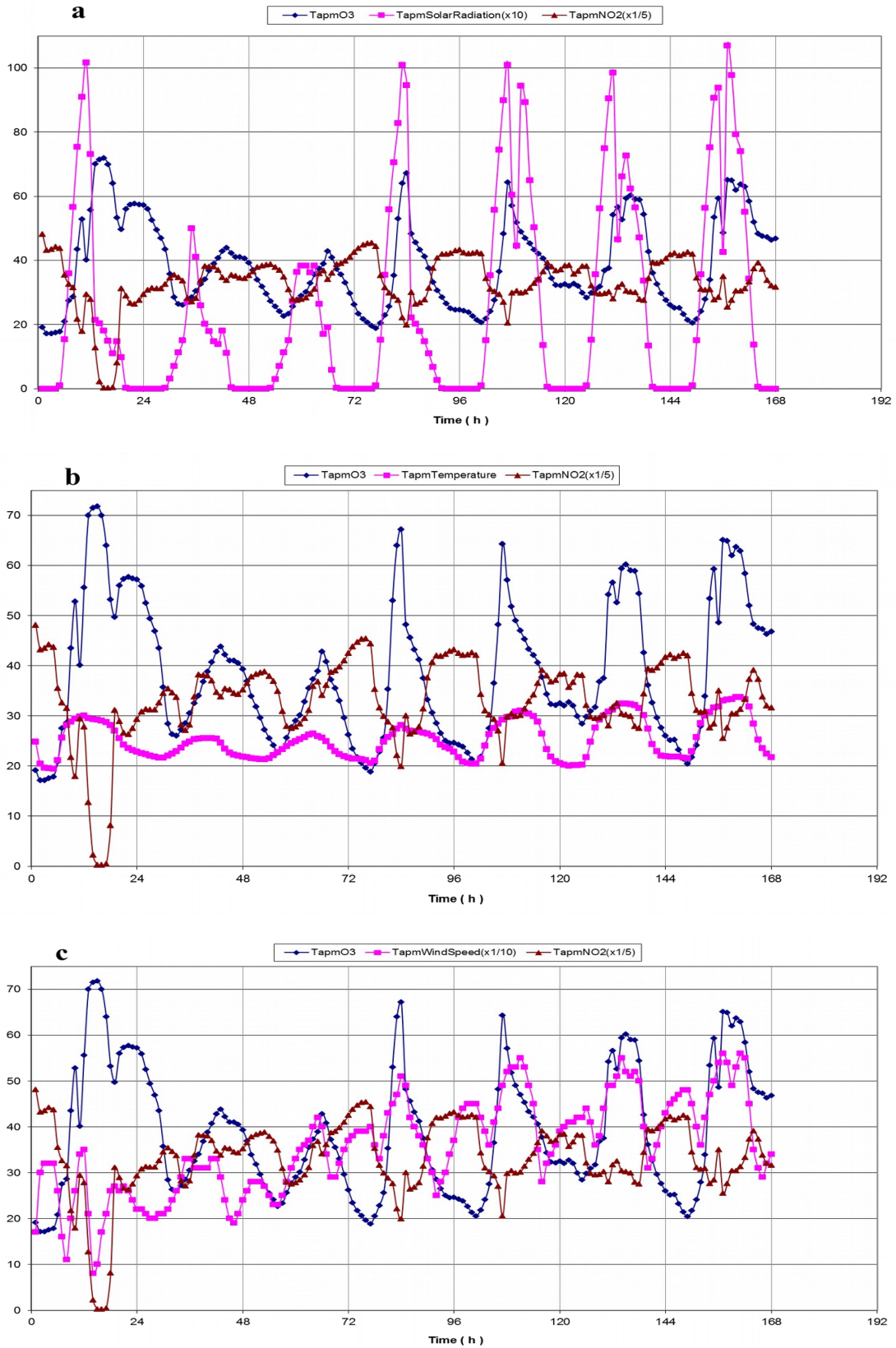


Figure 5.5 The variation of Ozone, NO_2 concentrations with solar radiation (a), temperature (b) and wind speed (c), during the simulated period

5.3. Tropospheric NO₂ vertical column densities simulation

Comparison of model and satellite data were performed for the whole domain with focus on selected regions (Figure. 4.3) at two different resolutions: 50×50 and 10×10 km². The analysis was performed on annual, seasonal and monthly basis. For the seasonal analysis, conventional seasons were used: winter (January, February, December), spring (March, April, May), summer (June, July, August) and autumn (September, October, November). Notice that winter is based on three months of the same year.

Satellite level-2 swath files were regridded on daily basis using the Wisconsin Horizontal Interpolation Program for Satellites, WHIPS (<http://www.sage.wisc.edu/download/WHIPS/WHIPS.html>) tool, onto common analysis grids with the same model resolution: 50×50 km² in the Europe and Gibraltar cases and 10×10 km² for the Po Valley and BeNeLux. In the regridding procedure, data with cloud cover larger than 0.2, surface albedo larger than 0.3 and solar zenith angle larger than 85° are discarded. This filter produces a mask of valid measurements that is applied also to model results to make the satellite and model datasets fully consistent.

The model output was sampled at the same satellite overpass time over Europe (13:30 UTC). The modelled VCD was computed using the averaging kernel (AK) corrected by the ratio between the total and the tropospheric AMF (Eskes and Boersma 2003). Because model simulation reach a height of about 500 hPa, the upper NO₂ content was extrapolated linearly from the upper model value to zero at the tropopause (where O₃ exceeds 150 ppb which, above Europe, corresponds to about 200 hPa) (Huijnen et al. 2010). The linear extrapolation to zero is well-supported by the climatological fields used in CITYZEN (Colette et al. 2011) and the analysis about the application of the AK found in Huijnen et al. (2010).

5.3.1 Low-resolution results

Results of the analysis of annual and seasonal tropospheric NO₂ VCD as simulated by the BOLCHEM model and observed by OMI over Europe (low resolution) are reported in Figures. 5.6, 5.7 and 5.8 and Table 5.5.

In this section, the main features are analysed for the whole Europe and selected regions: Po-Valley, BeNeLux and Gibraltar (Figure. 4.3), at coarse resolution. Yearly and seasonal analyses are also discussed. Figure 5.6 shows the annual spatial distribution of NO₂ VCD over Europe of the DOMINO product (right) and the model output (left), along with the difference between them (middle).

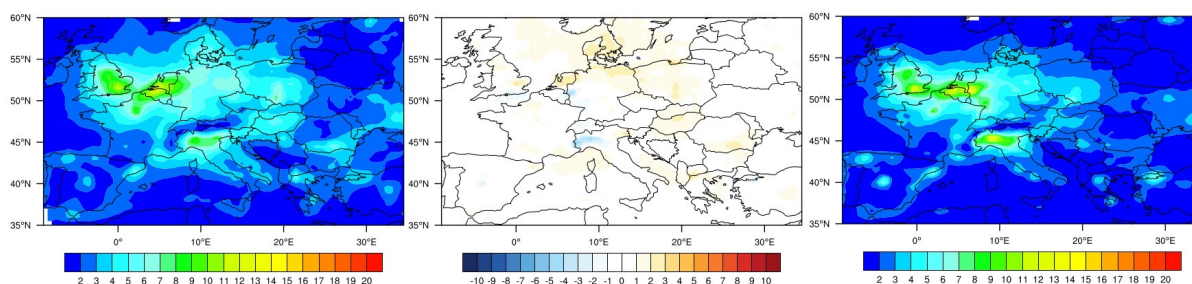


Figure. 5.6 Annual average of NO₂ VCD (unit: $\times 10^{15}$ molecules cm^{-2}) over Europe: model (left), model-satellite (middle) and satellite (right)

At a first glance, a good agreement between model and satellite can be noticed (Figure. 5.6). Similar features are displayed by predicted and simulated VCD over highly polluted regions (the Po Valley and BeNeLux hot-spots and the largest European cities; Paris, London, Madrid, Barcelona, Rome, etc.). Generally speaking, the model presents a background higher and smoother than the satellite, mainly in winter and autumn. The model underestimates VCD over some large cities (Cologne, Istanbul, Madrid, Milan, Turin), while displaying a weak overestimation over others (Athens, Barcelona, London, Marseilles, Paris, Rome) and a general overestimation over the Netherlands. Looking at the two hot-spots, it can be seen that VCD in the Po Valley is underestimated by the model, while the behaviour for BeNeLux is less uniform, displaying both over- and under-estimations.

Model underestimation observed in the Po Valley (Figure. 5.9 upper panel) can be related to the complex Alpine topography and its impact on the data retrieval (Schaub et al. 2007; Zhou et al. 2009), in addition to inaccuracies in the emissions inventory. In contrast to this seasonal change observed over Europe, the underestimation in the Po Valley is relatively uniform over time.

In the BeNeLux area (Figure. 5.10 upper panel), a mixture of slight over- and under-estimation of VCD is observed. The satellite map presents two maxima while the model only has one, missing the maximum observed over the Cologne area. This is likely to be caused by inaccuracies in the emission database. The effect of finer resolution will be discussed in “High resolution over Po Valley” and “High resolution over BeNeLux” sections.

Looking at the south-west part of the domain, the ship tracks are more visible in the model map, especially for the Gibraltar area, while the satellite map shows some signs of the North African big cities and industrial areas (e.g. Algiers, Oran, S’kikda, Tunis) that are not

visible in the model map, clearly reflecting the lack of emissions in the southern part of the simulated domain (North Africa).

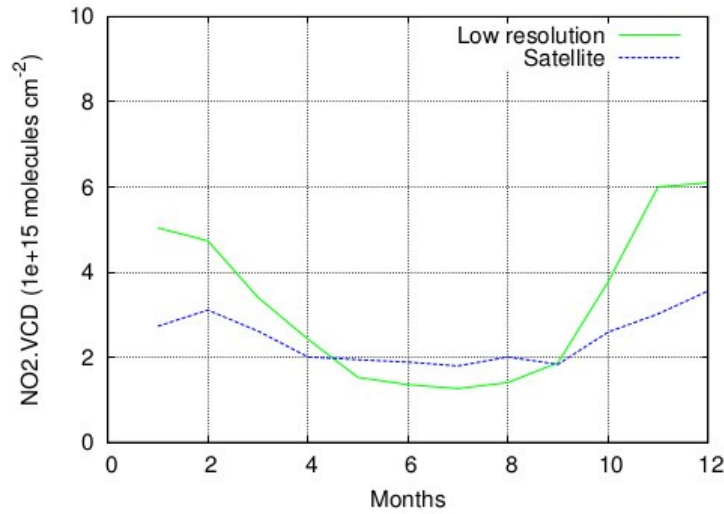


Figure 5.7 Area average of NO₂ VCD over Europe (see Figure. 4.3) of the monthly mean tropospheric columns for 2007

Annual and seasonal root mean square error (RMSE), mean bias (MB) and correlation (r) were computed for Europe and specific regions (see Table 5.5).

Region	Season	Low-resolution			High-resolution		
		RMSE	MB	r	RMSE	MB	r
Europe	Annual	0.82	0.52	0.90	-	-	-
	Winter	2.97	2.23	0.76	-	-	-
	Spring	0.75	0.24	0.91	-	-	-
	Summer	0.82	-0.55	0.88	-	-	-
	Autumn	1.61	1.20	0.86	-	-	-
Po valley	Annual	1.88	-0.46	0.74	1.39	0.11	0.91
	Winter	4.72	-0.11	0.46	5.13	2.58	0.69
	Spring	2.01	-1.23	0.83	1.66	-0.74	0.89
	Summer	1.51	-1.28	0.76	1.51	-1.30	0.81
	Autumn	2.03	1.03	0.81	2.10	1.13	0.86
BeNeLux	Annual	1.21	0.35	0.85	1.31	0.62	0.90
	Winter	2.81	1.80	0.61	2.69	1.44	0.66
	Spring	1.40	0.40	0.88	1.71	0.95	0.91
	Summer	2.13	-1.81	0.75	1.75	-1.37	0.83
	Autumn	2.07	1.67	0.84	2.11	1.67	0.87
Gibraltar	Annual	0.50	0.31	0.79	-	-	-
	Winter	1.52	1.31	0.77	-	-	-
	Spring	0.27	-0.06	0.79	-	-	-
	Summer	0.44	-0.32	0.60	-	-	-
	Autumn	0.67	0.45	0.76	-	-	-

Table 5.5 Annual and seasonal statistical indices computed over Europe and selected regions

The spatial correlation of the annual maps between OMI DOMINO v2.0 and BOLCHEM is 0.90. The value of the above correlation coefficient is high compared to typical values found in the literature.

Seasonal average maps of VCD are presented and compared in Figure 5.8, and a statistical analysis is reported in Table 5.5. Figure 5.8 is organised in the same way as Figure 5.6: model results in the left panel, satellite observations in the right panel and differences in the middle.

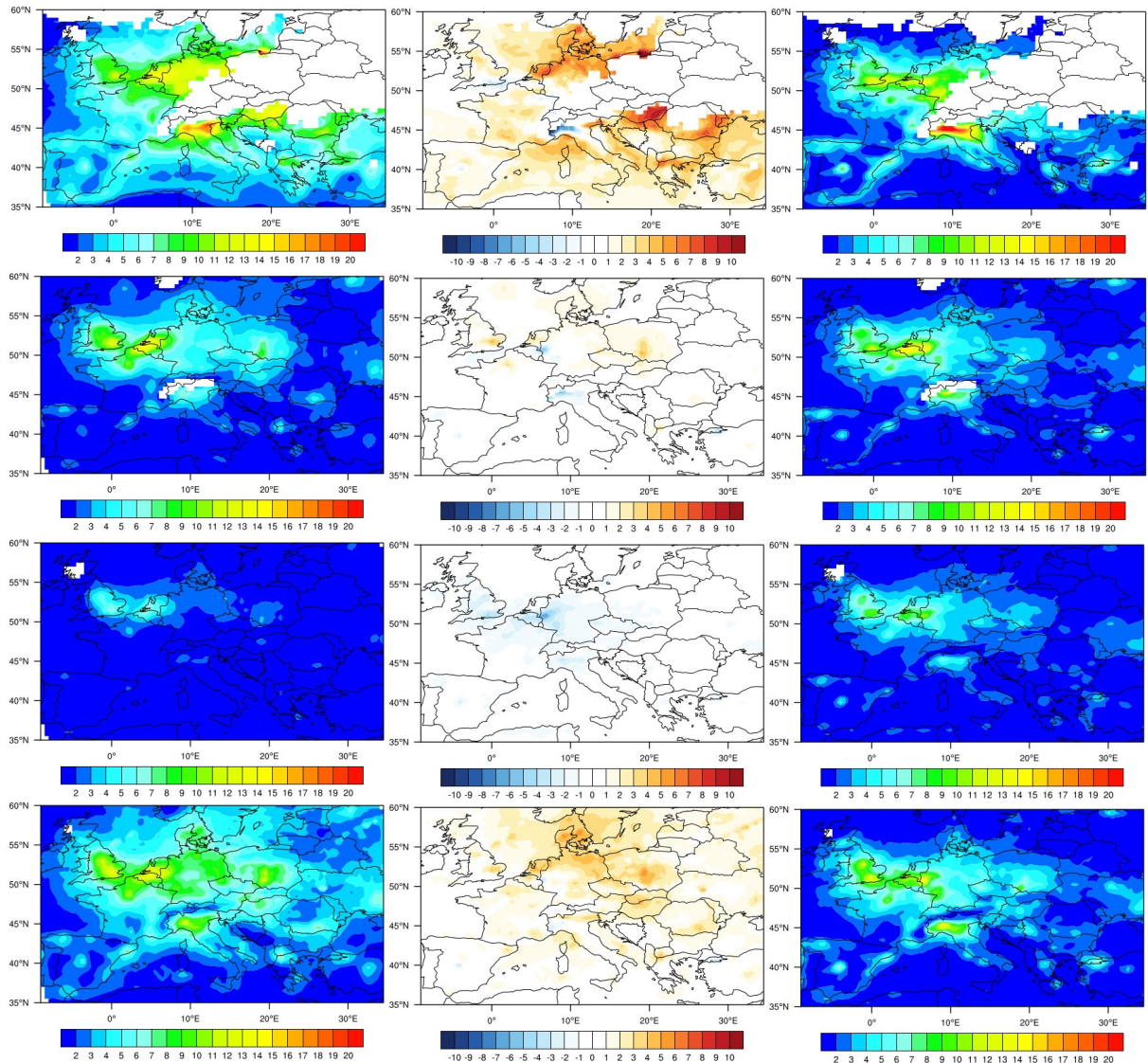


Figure 5.8 Seasonal average of NO₂ VCD (Unit: $\times 10^{15}$ molecules cm^{-2}) over Europe: model (left), model-satellite (middle) and satellite (right). Seasons are winter, spring, summer and autumn from top to bottom, respectively. White areas for model and satellite maps represent missing values

Figure 5.8 shows a good agreement between model and satellite data with hot-spots and urban polluted patterns similarly distributed in spring and summer, with spatial correlation coefficients (Table 5.5) of 0.91 and 0.88, respectively, and small RMSE and MB. In autumn and winter, there is a general overestimation more pronounced near areas where missing values are present, possibly highlighting some efficiency problem in the filtering procedure. In particular, the large areas of missing values observed in north-east Europe result from the combination of cloudiness and high surface albedo due to snow cover. Selecting thresholds higher than the “standard ones” would enlarge the missing data areas, thus removing the large overestimation in winter over, e.g. Hungary. Underestimation is observed in some spots like Madrid, Frankfurt and the English Channel, with a strong maximum in the Po Valley in which, however, high overestimation in winter is observed in pixels adjacent to missing data areas and can be partly removed with more strict thresholds. Despite this, the spatial correlation over Europe is still high (0.86) in autumn and acceptable in winter (0.76).

Looking at specific regions, it is observed that (Table 5.5) the correlation is moderately higher for BeNeLux than for the Po Valley and Gibraltar. The correlation is good in the Po Valley, except in winter when the area is frequently covered by clouds. Gibraltar presents also good correlation, except in summer, in contrast to the lowest value observed in winter in the other two regions. Concerning the MB, the annual values, which differ for each area, are unevenly distributed over time, with typically small negative values in spring/summer and high positive values in winter and autumn, except for the Po Valley where even winter values are very small, due to a compensation between the underestimation in the west and the overestimation in the east.

Figure 5.11 shows the scatter-plots between the BOLCHEM simulated and the OMI retrieved tropospheric NO₂ VCD over Europe, Gibraltar for low-resolution ($50 \times 50 \text{ km}^2$) and the Po Valley, BeNeLux for high-resolution ($10 \times 10 \text{ km}^2$). For Europe, most of the data is above the 1:1 line, which reflects the already noted annual overestimation, with the subset of data for north-eastern Europe clearly identifiable, and well above the regression line. Clear overestimation is also apparent in the BeNeLux and Gibraltar scatter-plots. In the Po Valley, the scatter-plot displays an overestimation for small values and an underestimation for the highest end of the VCD range, which corresponds to the model underestimation over the highly polluted Milan area observed in Figure. 5.9.

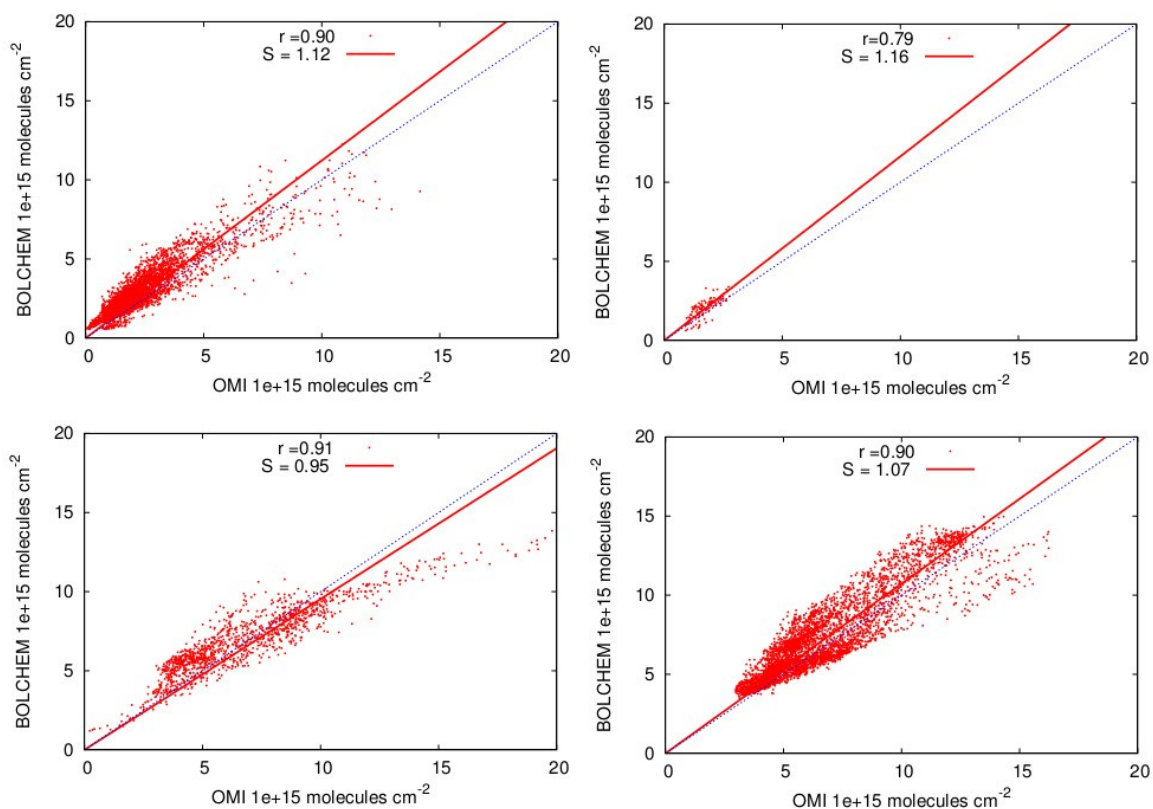


Figure. 5.11 Scatter plots between BOLCHEM and OMI NO₂ columns: a Europe, b Gibraltar at low-resolution, c Po Valley and d BeNeLux at high-resolution. (r) is the correlation coefficient and (S) is the slope

Despite Gibraltar was not the focus of the CITYZEN project, model simulation cover also that region which is highly affected by shipping emission. Although the domain is located near the boundary and is probably influenced by the boundary conditions, which in the present simulations are climatological, the area is mostly affected by shipping emissions which are present in the emission dataset used for the model simulations and, therefore, the analysis of results can provide useful information.

Figure 5.12 displays NO₂ VCDs for the Gibraltar region, which are lower than in the other selected regions, this area not being affected by very large emissions. VCD values range from 100 to 400×10^{15} molecules cm^{-2} during the whole of 2007 for both model and satellite. The lack of emissions in North Africa, already observed when analysing results for Europe, do not seem to play a major role. In general, the most influential sources in the area seem to be the southern Spain cities and shipping emissions.

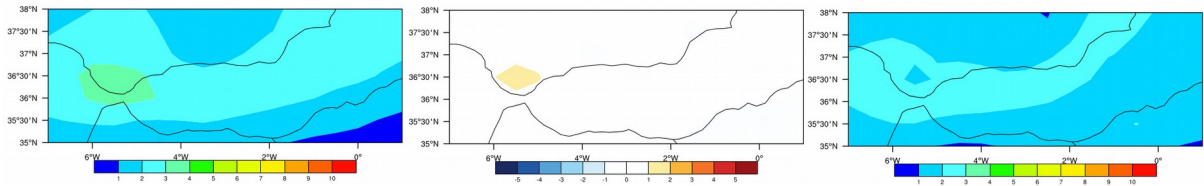


Figure. 5.12 Annual average of NO₂ VCD (unit: $\times 10^{15}$ molecules cm^{-2}) over Gibraltar: left (model), centre (difference: model-satellite) and right (satellite)

The model predicts higher values of VCD than the satellite, in agreement with previous findings where a strong model overestimation is observed over the sea in correspondence to shipping routes (Im et al. 2014).

Looking at the annual cycle (Figure. 5.13), during spring and summer, there is a small difference between the spatial average of OMI measured and model simulated NO₂ VCDs, ranging from 5 to 8 % in spring and is 18 % in summer. In winter and autumn, a model overestimation is observed.

A more detailed analysis is found in Table 5.5. The statistical analysis displays a small magnitude of the Mean Bias in spring and summer with -0.06 and -0.32×10^{15} molecules cm^{-2} , respectively. It is worth noting that an unusual seasonal spatial correlation (high in winter and small in summer) appears in the seasonal statistical analysis (Table 5.5) in contrast to what happens for the other selected regions. It must be borne in mind, however, that this region is not only less affected by large emissions but also presents low cloudiness.

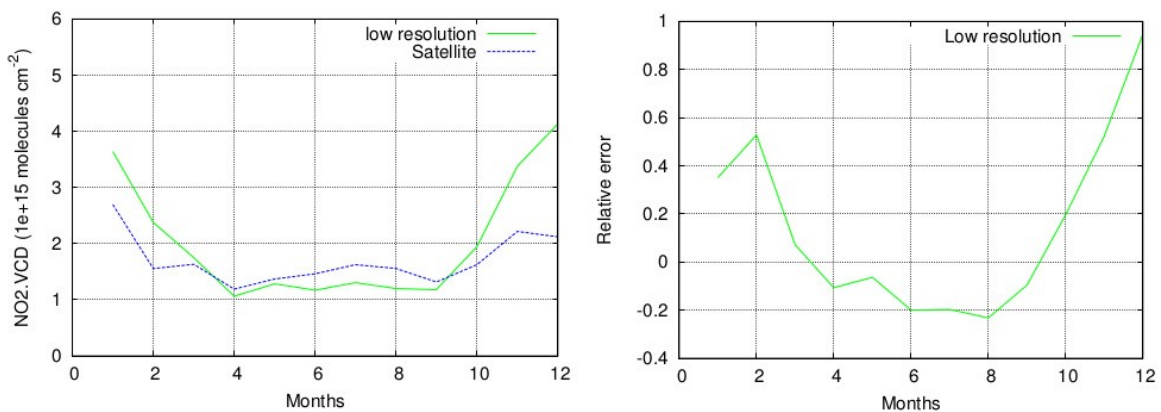


Figure. 5.13 Area average of NO₂ VCD over Gibraltar (see Figure. 4.3) of the monthly mean tropospheric columns for 2007 (left panel). In the right panel, relative differences are shown

5.3.2 High-resolution results

In this section, we present a comparison of DOMINO v2.0 with coarse- and high-resolution simulated tropospheric NO₂ VCDs from the BOLCHEM model over the Po Valley hot-spot. The discussion is based on the results reported in Figures. 5.9 and 5.14 and Table 5.5.

Figure 5.9 displays a generally good agreement between model and satellite for the annual average, especially for the high-resolution simulation. The same spatial features, which changes significantly with resolution, are discerned in both the model and satellite such as the high NO₂ amounts for Milan and low amounts over the Alps and Appenines. Model overestimation in Liguria (west of Genoa) and over the Ligurian Sea is observed. Concerning Liguria, the over-estimation is possibly caused by the poor representation of the Maritime Alps barrier between the Po Valley and Ligurian Sea in the meteorological model, allowing for some spurious transport from the more polluted Po Valley area towards the sea. Underestimation is generally reduced except over Milan. The annual spatial correlation is $r = 0.91$ (Table 5.5), a clear improvement with respect to the low-resolution correlation ($r = 0.74$, Table 5.5).

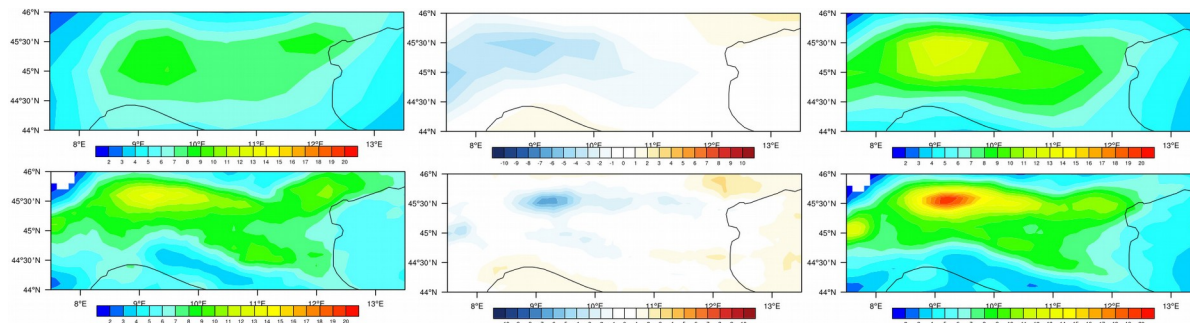


Figure 5.9 Annual average of NO₂ VCD (unit: $\times 10^{15}$ molecules cm^{-2}) over Po Valley: model (left), model-satellite (middle) and satellite (right), for low-resolution (top) and high-resolution (bottom)

Figure 5.14a presents the time series of the monthly mean VCD from OMI satellite measurements and model-predicted values averaged over the Po Valley region. The model is quite successful in capturing the VCD annual cycle, with small absolute differences, except in winter. Looking at the relative errors, the high-resolution simulated VCD values are larger than the OMI ones by 0 to 35 % during winter time. In summer, there is an underestimation of more than 40 %, enhanced by the low absolute values of VCD. A different picture emerges at coarse-resolution, which displays a better agreement in winter and autumn, with relative

errors ranging from 0 to -0.15 in winter and -0.43 to -0.48 in summer. The bulk effect of increasing resolution is to increase the simulated NO₂ VCD by 5 to 30 % for the whole year. This seems to be effective in reducing the error mainly in summer, when the photochemical reactions are dominant.

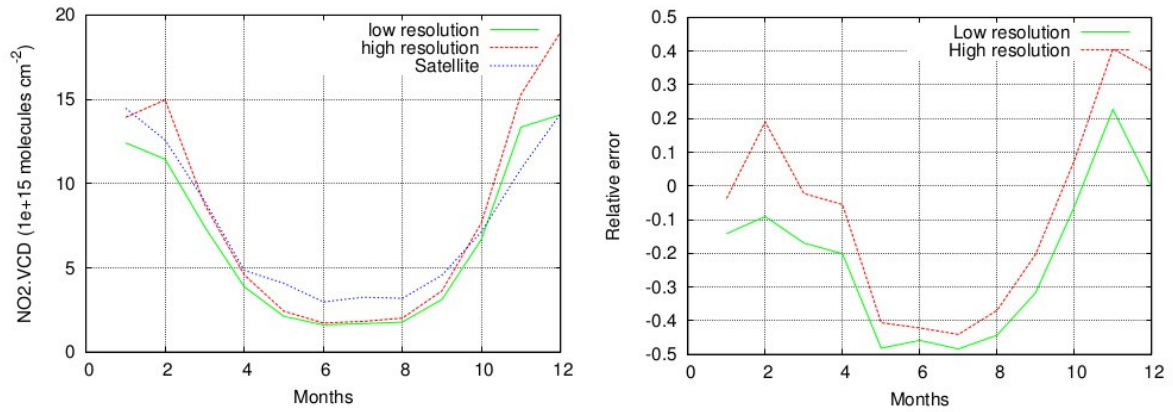


Figure 5.14 Area average of NO₂ VCD over Po Valley (see Figure. 4.3) of the monthly mean tropospheric columns for 2007 with different model resolutions (left panel). In the right panel, relative differences are shown

A good correlation is found for the Po Valley for all seasons in the high-resolution experiment (Table 5.5), higher than those found for the low-resolution experiment (Table 5.5) with a larger improvement in winter in which the lowest value is found for both resolutions. The mean bias shows variations with season for high-resolution, with the greatest value in winter (2.58×10^{15} molecules cm^{-2}). This highlights the better agreement between model and satellite observations in cloud-free conditions.

The seasonal statistical analysis in Table 5.5 demonstrates the positive effect of the high-resolution model in spring and summer and the negative effect during winter and autumn. Table 1 displays high RMSE in winter at both resolutions. The magnitude of the mean bias decreases with high-resolution from 1.23 to 0.74×10^{15} molecules cm^{-2} in spring, whereas the same parameter increases from 0.11 , 1.03 to 2.58 and 1.13×10^{15} molecules cm^{-2} for winter and autumn, respectively.

As for the Po Valley, the BeNeLux model results at two different spatial resolutions are compared with satellite data. In Figure. 5.10, which shows a close-up of the BeNeLux region, the spatial distribution (maxima and minima locations) of NO₂ VCDs is not very well captured by the model at low resolutions because model only presents a maximum of VCD while satellites displays two. This picture is slightly improved by the high-resolution that displays a secondary maximum in correspondence to the Rhine-Ruhr area, the main center of

European steel production and the big inland port of Duisburg. However, VCD in this area is slightly underestimated at both resolution with a more pronounced effect at low-resolution (Figure. 5.10b, e). On the other end, high-resolution simulation displays larger overestimation in areas not affected by large emissions. Moreover, as a general comment, the model always displays a smoothly distributed VCD, unlike the satellite VCD, which is more concentrated in areas of high emissions.

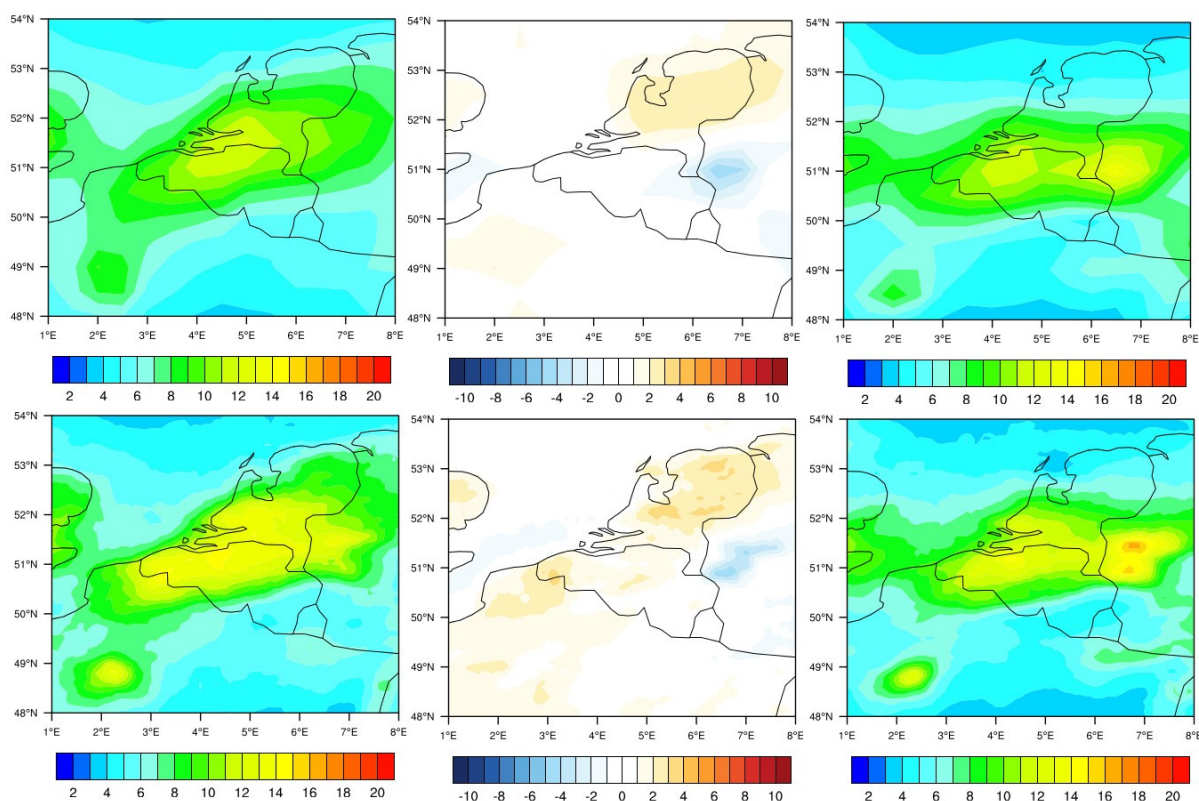


Figure. 5.10 Annual average of NO₂ VCD (unit: $\times 10^{15}$ molecules cm^{-2}) over BeNeLux: model (left), model-satellite (middle) and satellite (right), for low-resolution (top) and high-resolution (bottom)

In contrast to the results for the sea in other areas, a large NO₂ VCD is observed by both model and satellite between the UK and Belgium, and more generally (see Figures. 5.6 and 5.8) in the whole English Channel and south of the North Sea. This is possibly because, in addition to shipping emissions, a large contribution to the high level of pollution comes from the highly polluted adjacent land areas.

The spatial correlation is improved in high-resolution simulation (Table 5.5) uniformly over the seasons. The statistical analysis shows that the high-resolution model has positive effects

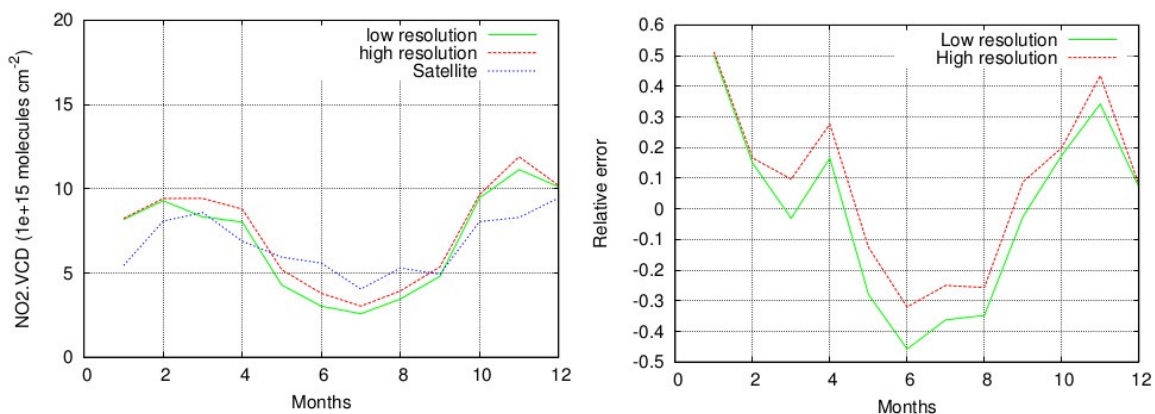


Figure 5.15 Area average of NO₂ VCD over BeNeLux (see Figure. 4.3) of the monthly mean tropospheric columns for year 2007 with different model resolutions (left panel).

In the right panel, relative differences are shown

during summer time in agreement with Yamaji et al. (2014). This is more evident in this region than in the Po Valley. According to the relative error plot (Figure. 5.15b), the high-resolution simulation reduces the error between simulated and measured VCDs by 29 % in summer.

As shown in Table 5.5, MB displays strong seasonal variations. The RMSE varies slightly, displaying higher values in winter and autumn and lower in spring and summer with only slight variations between high and low resolution.

CONCLUSIONS

Photochemical air pollution modelling and simulation in different atmospheric scales was realised during this study. The objective of the first part was to investigate the photochemical smog formation, the dispersion and concentration of O₃ and NO₂, as well the meteorology effects, over a heavy industrialized area. The region is a mountainous basin with complex terrain, which results in the local meteorological circulations observed. A coupled mesoscale prognostic meteorological and air pollution model in combination with data, which were collected by in situ and remote monitoring measurements, was used. More specific, three-dimensional photochemical simulations have been performed by The Air Pollution Model (TAPM) for a seven-day period in the summer of 2006. A model configuration including the industrial sources has been built to simulate the pollutants dispersion and transformation in and around the selected area. Results from the numerical simulation were compared with observations of both in situ monitoring station and DOAS, which have been installed in the biggest city in the region.

Comparison of model's results to observations, showed the considerable skill of the model (TAPM) in predicting the major local-scale features affecting the pollutants dispersion and concentrations in the area of interest. Simulated meteorological fields were viewed as realistic enough to drive transport and the mixing of chemical species. More specifically temperature has shown significant agreement against experimental data. Wind speed and direction were reproduced with wind reversal observed at the same times in the model as in the measurements. Solar radiations were evaluated very well against monitoring station data.

Regarding the O₃ concentrations, the statistical performance measures (IOA, RMSE and Correlation coefficient) indicated a good agreement between the predicted and observed O₃ values. However, there were some differences between predicted and measured values maybe due to the level where each tool (TAPM, DOAS and MS) captured the information, while the drift of the simulation's results is due to relative high background concentrations which was used as input in the model.

Concerning the NO_2 , the simulated values were not compared well with surface data. Differences were also observed between the data sets collected by DOAS system and MS. The MS location is very close to vehicular sources emitting considerable amounts of NO_x . That is why its values are higher than DOAS values which are acquired from high level (10 to 15m) and indicate averages over the path above the street canyon. On the other hand, TAPM results represent a grid point at 10 m higher than the ground. Besides, the location of the ground sampling station is not exactly below the DOAS path and TAPM grid point.

A comparison between pollutants (O_3 , NO_2) and meteorology parameters (temperature, solar radiation and wind speed) has shown clearly the photochemical process where the primary pollutants and sunlight react to produce Ozone. The statistical analyses showed a negative agreement between NO_2 against temperature and solar radiation. On the other hand, a good agreement has been achieved between temperature, solar radiation and ozone. TAPM simulation and experimental data has shown that as wind speed increases, the concentration of ozone increases because fresh oxygen is supplied in the photochemical cycle that reacts with NO_2 producing O_3 . This highlights clearly the effects of meteorology conditions and topography on the air pollution smog formation. In addition a very interesting symmetric level has occurred between ozone and NO_2 which follow opposite trends. A steady rise in ozone level is observed with decreased NO_2 concentration. The peak concentration of NO_2 occurs before the peak of ozone because the photochemical reaction sequence forms NO_2 first and then ozone. This shows the favourable photochemical ozone production within the urban complexity between morning hours and 18.00 hours in the afternoon.

Regarding the second part of the thesis, simulations of atmospheric pollutants for the year 2007, with a focus on hot-spots at higher resolution were analysed in order to verify the ability of the BOLCHEM model to reproduce the NO_2 vertical column density retrieved from OMI (DOMINO v2.0 product from TEMIS). A two step approach is employed during this study to compare model results directly with satellite data. In the first step, best quality satellite retrievals are selected through specific conditions (cloud coverage, surface albedo and solar zenith angle) and built satellite data into the same model resolutions and regions. In the second step, the model simulation results are transformed using the averaging kernel interpolated to the model pressure levels. The analysis was performed on an annual, seasonal and monthly basis.

The model turned out to perform well, with statistical parameters in line with those found in the literature for other comparison experiments (e.g. Han et al. 2011; Zyrichidou et al. 2013, Im et al. 2014) with particularly high values of the correlation coefficient. Analysis on a seasonal basis confirms the good BOLCHEM performances, while revealing a difference between the “warm” and “cold” seasons: in spring and summer, performances are usually better than in winter. However, the statistical significance of winter satellite data is reduced by the low number of observations caused by the presence of clouds and also by increased surface albedo due to snow cover.

Performances in the low polluted region of Gibraltar, where one of the main sources is shipping emissions, is relatively good despite the missing emissions from North Africa and also possibly by the boundary conditions can have a negative influence. At variance with the other analysed regions, the spatial correlation is higher in winter and lower in summer when photochemistry is active.

The analysis of high-resolution simulations over the two selected hot-spots reveals that high-resolution is more effective in the Po Valley, where it increases the spatial correlation more than in the BeNeLux. However, the effect on the other scores is less clear. The increase of correlation is an important signature of the impact of non-linearities in photochemistry. The observed differences between the two hot-spots in response to increasing resolution can be explained by the large differences in meteorology. In BeNeLux, where wind is typically stronger than in the Po Valley and causes more mixing which, in turn, is expected to make the concentrations less dependent on local emissions, high resolution does not seem to increase the model prediction. This is confirmed by the differences observed in the seasonal analysis, which shows a positive impact in “warm” seasons, where photochemistry is more effective, and negative in “cold” ones.

An extended analysis, also involving surface data and ground-based remote sensing with profiling capabilities, would be an interesting step towards understanding both satellite data reliability and model performances with regard to the effect of vertical distribution, which is known to be an important issue for both models and satellites.

References

- [1] Antonacci G (2005) Air pollution modelling over complex topography. PhD thesis, Università degli Studi di Trento
- [2] Ashmore MR (2005) Assessing the future global impacts of ozone on vegetation. *Plant Cell and Environment* 28(8):949–964. doi:10.1111/j.1365-3040.2005.01341.x
- [3] Atkinson BW (1981) *Meso-Scale Atmospheric Circulations*, Academic Press, 1–445
- [4] Baklanov A, Schlunzen K, Suppan P, Baldasano J, Brunner D, Aksoyoglu S, Carmichael G, Douros J, Flemming J, Forkel R, Galmarini S, Gauss M, Grell G, Hirtl M, Joffre S, Jorba O, Kaas E, Kaasik M, Kallos G, Kong X, Korsholm U, Kurganskiy A, Kushta J, Lohmann U, Mahura A, Manders-Groot A, Maurizi A, Moussiopoulos N, Rao ST, Savage N, Seigneur C, Sokhi RS, Solazzo E, Solomos S, Sørensen B, Tsegas G, Vignati E, Vogel B, Zhang Y (2014) Online coupled regional meteorology chemistry models in Europe: current status and prospects. *Atmos Chem Phys* 14(1):317–398. doi:10.5194/acp-14-317-2014
- [5] Bernard SM, Samet JM, Grambsch A, Ebi KL, Romieu I (2001) The potential impacts of climate variability and change on air pollution related health effects in the United States. *Environ Health Perspect* 109:199–209
- [6] Billet SJ, Toro EF (1997) On WAF-Type schemes for multidimensional hyperbolic conservation laws. *J Comput Phys* 130:1–24
- [7] Boersma KF, Eskes HJ, Veefkind JP, Brinksma EJ, van der ARJ, Sneep M, van den Oord GHJ, Levelt PF, Stammes P, Gleason JF, Bucsela EJ (2007) Near-real time retrieval of tropospheric NO₂ from OMI. *Atmos Chem Phys* 7:2103–2118
- [8] Boersma KF, Eskes HJ, Dirksen RJ, van der ARJ, Veefkind JP, Stammes P, Huijnen V, Kleipool QL, Sneep M, Claas J, Leitao J, Richter A, Zhou Y, Brunner D (2011) An improved tropospheric NO₂ column retrieval algorithm for the Ozone Monitoring Instrument. *Atmos Meas Tech* 4:1905–1928
- [9] Brulfert G, Chemel C, Chaxel E, Chollet JP (2005) Modelling photochemistry in alpine valleys. *Atmos Chem Phys* 5:2341–2355
- [10] Businger JA, Wyngaard JC, Izumi Y and Bradley EF (1971) Flux profile relationships in the atmospheric surface layer, *J. Atmos. Sci.* 28, 181-189.
- [11] Butenschoen M, Maurizi A, Tampieri F (2003) Bolchem 0.9: A 3d prediction model of the meteorology and the chemical composition of the atmosphere. Tech. rep. CNR-ISAC, Italy
- [12] Chen KS, Ho YT, Lai CH, Chou YM (2003) Photochemical modeling and analysis of meteorological parameters during ozone episodes in Kaohsiung, Taiwan. *Atmos Environ* 37:1811–1823

- [13] Chen R, Samoli E, Wong CM, Huang W, Wang Z, Chen B, Kan H (2012) Associations between short-term exposure to nitrogen dioxide and mortality in 17 Chinese cities: The China Air Pollution and Health Effects Study (CAPES). *Environ Int* 45:32–38
- [14] Colette A, Granier C, Hodnebrog Ø, Jakobs H, Maurizi A, Nyiri A, Bessagnet B, D'Angiola A, D'Isidoro M, Gauss M, Meleux F, Memmesheimer M, Mieville A, Rouil L, Russo F, Solberg S, Stordal F, Tampieri F (2011) Air quality trends in Europe over the past decade: a first multi-model assessment. *Atmos Chem Phys* 11:11,657–11,678. doi:10.5194/acpd-11-19029-2011
- [15] Colette A, Granier C, Hodnebrog Ø, Jakobs H, Maurizi A, Nyiri A, Rao S, Amann M, Bessagnet B, D'Angiola A, Gauss M, Heyes C, Klimont Z, Meleux F, Memmesheimer M, Mieville A, Rouil L, Russo F, Schucht S, Simpson D, Stordal F, Tampieri F, Vrac M (2012) Future air quality in Europe: a multi-model assessment of projected exposure to ozone. *Atmos Chem Phys* 12(21):10,613–10,630. doi:10.5194/acp-12-10613-2012
- [16] Currier RL, Kranenburg R, Segers AJ, Timmermans RMA, Schaap M (2014) Synergistic use of OMI NO₂ tropospheric columns and LOTOSEUROS to evaluate the NO_x emission trends across Europe. *Remote Sens Environ* 149:58–69
- [17] David HF (2000) Air pollution. CRC Press LLC
- [18] Dias de Freitas E, Droprinchinski Martins L, da Silva Dias PL, Fatima de Andrade M (2005) A simple photochemical module implemented in RAMS for tropospheric ozone concentration forecast in the metropolitan area of Sao Paulo, Brazil: coupling and validation. *Atmos Environ* 39:6352–6361
- [19] Eskes HJ, Boersma KF (2003) Averaging kernels for doas totalcolumn satellite retrievals. *Atmos Chem Phys* 3:1285–1291. doi:10.5194/acp-3-1285-2003, 2003
- [20] Fenger J, Hertel O, Palmgren F (1999) Urban air pollution – European aspects. Kluwer Academic Publishers
- [21] Han KM, Lee CK, Lee J, Kim J, Song CH (2011) A comparison study between model-predicted and OMI-retrieved tropospheric NO₂ columns over the Korean peninsula. *Atmos Environ* 45:2962–2971
- [22] Hilboll A, Richter A, Burrows JP (2013) Long-term changes of tropospheric NO₂ over megacities derived from multiple satellite instruments. *Atmos Chem Phys* 13:4145–4169
- [23] Huijnen V, Eskes HJ, Poupkou A, Elbern H, Boersma KF, Foret G, Sofiev M, Valdebenito A, Flemming J, Stein O, Gross A, Robertson L, D'Isidoro M, Kioutsioukis I, Friese E, Amstrup B, Bergstrom R, Strunk A, Vira J, Zyryanov D, Maurizi A, Melas D, Peuch VH, Zerefos C (2010) Comparison of OMI NO₂ tropospheric columns with an ensemble of global and European regional air quality models. *Atmos Chem Phys* 10:3273–3296
- [24] Hurley P (2005) The air pollution model (TAPM) version 3. Part 1: technical description, CSIRO atmospheric research technical paper no. 71. Available at <http://www.dar.csiro.au/TAPM>

- [25] Im U, Daskalakis N, Markakis K, Vrekoussis M, Hjorth J, Myriokefalitakis S, Gerasopoulos E, Kouvarakis G, Richter A, Burrows J, Pozzoli L, Unal A, Kindap T, Kanakidou M (2014) Simulated air quality and pollutant budgets over Europe in 2008. *Sci Total Environ* 470–471:270–281
- [26] Johnson GM (1984) A simple model for predicting the ozone concentration of ambient air. *Proceedings of the 8th International Clean Air and Environment Conference, New Zealand, Clean Air Society of Australia & New Zealand*
- [27] Kubler J (2001) Integrated assessment of photochemical air pollution control strategies. PhD thesis. Ecole Polytechnique Federale de Lausanne.
- [28] Kukkonen J, Olsson T, Schultz DM, Baklanov A, Klein T, Miranda AI, Monteiro A, Hirtl M, Tarvainen V, Boy M, Peuch VH, Poupkou A, Kioutsioukis I, Finardi S, Sofiev M, Sokhi R, Lehtinen KEJ, Karatzas K, San Jos e R, Astitha M, Kallos G, Schaap M, Reimer E, Jakobs H, Eben K (2012) A review of operational, regional-scale, chemical weather forecasting models in Europe. *Atmos Chem Phys* 12(1):1–87. doi:10.5194/acp-12-1-2012
- [29] Lalitaporn P, Kurata G, Matsuoka Y, Thongboonchoo N, Surapipith V (2013) Long-term analysis of no₂, co, and aod seasonal variability using satellite observations over asia and intercomparison with emission inventories and model. *Air Qual Atmos Health* 6:655–672
- [30] Latza U, Gerdes S, Baur X (2009) Effects of nitrogen dioxide on human health: systematic review of experimental and epidemiological studies conducted between 2002 and 2006. *Int J Hyg Environ Health* 212:271–287
- [31] Levelt PF, van denOord GHJ, Dobber MR, Malkki A, Visser H, de Vries J, Stammes P, Lundell JOV, Saari H (2006) The ozone monitoring instrument. *IEEE Trans Geosci Remote Sens* 44:1093–1100
- [32] Linkov I, Loney D, Cormier S, Satterstrom FK, Bridges T (2009) Weight-of-evidence evaluation in environmental assessment: review of qualitative and quantitative approaches. *Sci Total Environ* 407: 5199–5205
- [33] Lorenz EN (1960) Energy and numerical weather prediction. *Tellus* 12:364–373
- [34] Maurizi A, D’Isidoro M, Mircea M (2010) BOLCHEM, an integrated system for atmospheric dynamics and composition. In: Baklanov A, Mahura A, Sokhi R (eds) *Integrated systems of mesometeorological and chemical transport models*, vol 8. Springer, p 186
- [35] Maurizi A, Russo F, Tampieri F (2013) Local vs. external contribution to the budget of pollutants in the Po Valley (Italy) hot spot. *Sci Total Environ* 458–460:459–465
- [36] Mircea M, D’Isidoro M, Maurizi A, Vitali L, Monforti F, Zanini G, Tampieri F (2008) A comprehensive performance evaluation of the air quality model BOLCHEM to reproduce the ozone concentrations over Italy. *Atmos Environ* 42(6):1169–1185
- [37] Monks PS, Granier C, Fuzzi S, Stohl A, Williams ML, Akimoto H, Amann M, Baklanov A, Baltensperger U, Bey I, Blake N, Blake RS, Carslaw K, Cooper OR, Dentener F, Fowler D, Fragkou E, Frost GJ, Generoso S, Ginoux P, Grewe V, Guenther A, Hansson, HC, Henne S, Hjorth

- J, Hofzumahaus A, Huntrieser H, Isaksen ISA, Jenkin ME, Kaiser J, Kanakidou M, Klimont Z, Kulmala M, Laj P, Lawrence MG, Lee JD, Liousse C, Maione M, McFiggans G, Metzger A, Mieville A, Moussiopoulos N, Orlando JJ, CD ODowd, Palmer PI, Parrish DD, Petzold A, Platt U, Poschl U, Prevo ASH, Reeves CE, Reimann S, Rudich Y, Sellegri K, Steinbrecher R, Simpson D, ten Brink H, Theloke J, van der Werf GR, Vautard R, Vestreng V, Vlachokostas C, von Glasow R (2009) Atmospheric composition change global and regional air quality. *Atmos Environ* 43:5268–5350
- [38] Moussiopoulos N, Papalexiou S, Sahn P (2006) Wind flow and photochemical air pollution in Thessaloniki, Greece. Part I: simulations with the European zooming model. *Environ Model Softw* 21:1741–1751
- [39] Richter A, Burrows JP (2002) Tropospheric NO₂ for GOME measurements. *Adv Space Res* 29(11):1673–1683
- [40] Richter A, Burrows JP, Nuß H, Granier C, Niemeier U (2005) Increase in tropospheric nitrogen dioxide over China observed from space. *Nature* 437:129–132
- [41] Roulet YA (2004) Validation and application of an urban turbulence parameterisation scheme for mesoscale atmospheric models. PhD thesis, École polytechnique fédérale de lausanne.
- [42] Peng Y-P, Chen K-S, Wang H-K, Lai C-H, Lin M-H, Lee C-H (2011) Applying model simulation and photochemical indicators to evaluate ozone sensitivity in southern Taiwan. *J Environ Sci* 23:790–797
- [43] Seinfeld JH and Pandis SN (2005) Atmospheric chemistry and physics From Air Pollution to Climate Change, second edition
- [44] Schaub D, Brunner D, Boersma KF, Keller J, Folini D, Buchmann B, Berresheim H, Staehelin J (2007) SCIAMACHY tropospheric NO₂ over Switzerland: estimates of NO_x lifetimes and impact of the complex Alpine topography on the retrieval. *Atmos Chem Phys* 7:5971–5987
- [45] Sini JF (2005) Atmosphère météorologique et air humide, Ecole Centrale de Nantes
- [46] Solomon S, Portmann RW, Sanders RW, Daniel JS (1999) On the role of nitrogen dioxide in the absorption of solar radiation. *J Geophys Res* 104:12,047–12,058
- [47] Stull, R. B., 1988: An introduction to boundary layer meteorology, Kluwer Academic Publishers.
- [48] Tampieri F, Maurizi A (2007) Evaluation of the dispersion coefficient for numerical simulations of tropospheric transport. *Nuovo Cimento C* 30:395–406
- [49] Thom AS (1975) Momentum, mass and heat exchange of plant communities. Academic Press, volume 1, pages 57–109
- [50] Triantafyllou AG, Kiros E, Evagelopoulos V (2002) Respirable particulate matter at an urban and nearby industrial location: concentrations and variability and synoptic weather conditions during high pollution episodes. *J Air Waste Manage Assoc* 52:174–185

- [51] Triantafyllou AG, Zoras S, Evagelopoulos V, Garas S, Diamantopoylos C (2008) DOAS measurements above an urban street canyon in a medium sized city. *Glob NEST* 10:160–167
- [52] Triantafyllou AG, Krestou A, Matthaios V (2013) Source-receptor relationships by using dispersion model in a lignite burning area in western Macedonia, Greece. *Glob NEST J* 15(2):195–203
- [53] van der A RJ, Eskes HJ, Boersma KF, van Noije TPC, van Roozendael M, De Smedt I, Peters DHMU, Meijer EW (2008) Trends, seasonal variability and dominant NO_x source derived from a ten year record of NO₂ measured from space. *J Geophys Res* 113:D04,302.
doi:10.1029/2007JD009021
- [54] Vlachokostas C, Achillas C, Moussiopoulos N, Kalogeropoulos K, Sigalas G, Kalognomou E, Baniyas G (2010a) Health effects and social costs of particulate and photochemical urban air pollution: a case study for Thessaloniki, Greece. *Air Qual Atmos Health*. Doi:10. 1007/s11869-010-0096-1
- [55] Vlachokostas C, Nastis S, Achillas C, Kalogeropoulos K, Karmiris I, Moussiopoulos N, Chourdakis E, Baniyas G, Limperi N (2010b) Economic damages of ozone air pollution to crops using combined air quality and GIS modelling. *Atmos Environ* 44:3352–3361
- [56] Wang X, Carmichael G, Chen D, Tang Y, Wang T (2005) Impacts of different emission sources on air quality during March 2001 in the Pearl River Delta (PRD) region. *Atmos Environ* 39:5227–5241
- [57] Wang B, Chen Z (2013) An intercomparison of satellite-derived ground-level NO₂ concentrations with GMSMB modeling results and in-situ measurements - A North American study. *Environ Pollut* 181:172–181
- [58] Wilmott CJ, Ackleson SG, Davis RE, Feddema JJ, Klink KM, Legates DR, O'Donnell J, Rowe CM (1985) Statistics for the evaluation and comparison of models. *J Geophys Res* 90:8995–9005
- [59] Yamaji K, Ikeda K, Irie H, Kurokawa J, Ohara T (2014) Influence of model grid resolution on NO₂ vertical column densities over east asia. *J Air Waste Manag Assoc* 64:436–444
- [60] Zampieri M, Malguzzi P, Buzzi A (2005) Sensitivity of quantitative precipitation forecasts to boundary layer parameterization: a flash flood case study in the western mediterranean. *Nat Hazards Earth Syst Sci* 5:603–612
- [61] Zhou Y, Brunner D, Boersma KF, Dirksen R, Wang P (2009) An improved tropospheric NO₂ retrieval for OMI observations in the vicinity of mountainous terrain. *Atmos Meas Tech* 2:401–416
- [62] Zyrichidou I, Koukouli ME, Balis D, Katragkou E, Melas D, Poupkou A, Kioutsioukis I, van der A RJ, Boersma KF, van Roozendael M, Richter A (2009) Satellite observations and model simulations of tropospheric NO₂ columns over south-eastern Europe. *Atmos Chem Phys* 9:6119–6134

- [63] Zyrichidou I, Koukouli ME, Balis DS, Kioutsioukis I, Poupkou A, Katragkou E, Melas D, Boersma KF, van Roozendaal M (2013) Evaluation of high resolution simulated and OMI retrieved tropospheric NO₂ column densities over Southeastern Europe. *Atmos Res* 122:55–66
- [64] Zyryanov D, Foret G, Eremko M, Beekmann M, Cammas JP, D’Isidoro M, Elbern H, Flemming J, Friese E, Kioutsioukis I, Maurizi A, Melas D, Meleux F, Menut L, Moinat P, Peuch VH, Poupkou A, Razinger M, Schultz M, Stein O, Suttie M, Valdebenito A, Zerefos C, Dufour G, Bergametti G, Flaud JM (2012) 3D evaluation of tropospheric ozone simulations by an ensemble of regional Chemistry Transport Model. *Atmos Chem Phys* 12:3219–3240. doi:10.5194/acp-12-3219-2012